8-30-2022

Multimodal Imaging of Structural Concrete Using Image Fusion and Deep Learning

Sina Mehdinia
Portland State University

Multimodal Imaging of Structural Concrete Using Image Fusion and Deep Learning

by

Sina Mehdinia

A dissertation submitted in partial fulfillment of the
requirements for the degree of

Doctor of Philosophy
in
Civil and Environmental Engineering

Dissertation Committee:
Thomas Schumacher, Chair
Xubo Song
Eric Wan
David Yang
John Lipor
Avinash Unnikrishnan

Portland State University
2022

Abstract

Concrete structures may be exposed to a variety of loads and environments during their service life. Non-destructive testing (NDT) techniques can be helpful in evaluating the condition of a structure. Imaging provides a visual representation of the interior of concrete and its condition non-destructively. Ground penetrating radar (GPR) and ultrasonic echo array (UEA) using electromagnetic and stress waves, respectively, provide the data that can be used to reconstruct an image. In this PhD dissertation, image reconstruction and fusion algorithms, simulation, and a deep learning model were investigated with the goal to lay the foundation for enhanced imaging applications for concrete.

First, a multimodal 2D imaging pipeline is introduced that can process and fuse GPR and UEA data to enhance imaging of concrete. An algorithm, named extended total focusing method (XTFM) was developed that can reconstruct images from the raw signals collected with GPR and UEA instruments. This algorithm combines synthetic aperture focusing technique (SAFT) and total focusing method (TFM) concepts and can reconstruct images from multi-channel arrays with overlapping measurements. In addition, an image fusion algorithm is introduced that fuses GPR and UEA images using a multi-level wavelet decomposition and a NDT knowledge-based fusion rule. A novel local evaluation metric was developed to evaluate the output images of the algorithm. The results from three concrete specimens built in laboratory are reported and it is shown qualitatively, quantitatively, locally and globally that the reconstructed images represent an enhanced precise image of the interior of the concrete.

Second, the imaging pipeline was used to track damage progression in two full-scale reinforced concrete bridge column-footing specimens with different lap-splice detailing undergoing reverse-cyclic loading in the laboratory. A quantitative analysis revealed that changes in the images can be tracked as early as the columns undergo some initial damage. In addition, it is shown that changes along the height of column vary, i.e., the lower sections of the column exhibit more damage. This observation is in agreement with the internal force demand distribution of the column. A so-called backwall analysis suggests that the difference in the performance of the two tested columns can be captured using imaging.

Finally, GPR simulations and deep learning pipeline was developed that can be used to generate large datasets with different setups to employ deep learning to assist with imaging. A simulated dataset with 3000 data examples of B-scans was generated. A deep neural network model is introduced that can accurately predict two key required parameters for image reconstruction: the dielectric constant of the concrete and the time offset parameter of the GPR measurement. Tuning these two parameters is a cumbersome process usually done manually. Precise prediction of these parameters results in focused images where reflectors such as rebars in concrete, have correct shape and location. It is shown that the developed model can accurately predict these two parameters with an $R^2 > 0.999$. The model was tested on data from the three experimental specimens and resulted in accurate images. The generalizability of the method is also discussed. Gradient visualization is used to highlight which part of an image is utilized most in predictions. It was found that the neural network pays the most attention to the angle of reflections to predict the dielectric constant, and the surface wave portion of GPR for the time offset parameter.

Acknowledgments

I would like to dedicate this dissertation to my father, Hossein Mehdinia, who is not among us today. He taught me to prioritize education in my life and to be a constant learner. He had a great talent in mathematics but was banned from entering university due to political instability of my home country.

I would like to express my deepest gratitude to my PhD advisor Dr. Thomas Schumacher who is not only a great teacher, but an amazing human being. He supported me in every step of my PhD journey, and I would not have been able to complete this dissertation without his support and encouragement. I would also like to thank the other members of my advisory committee, Dr. Xubo Song, Dr. Eric Wan, Dr. John Lipor, Dr. David Yang, and Dr. Avinash Unnikrishnan for their valuable insights and suggestions.

I am indebted to my wife Mina Mehdinia, who supported me at every moment of my PhD journey with her love, patience, sacrifice, and believing in me all the time.

I am indebted to my mother Tooba Seifi, and my sister Niloofar Mehdinia who encouraged me to follow my dreams and helped me becoming who I am today.

Table of Contents

List of Tables

List of Figures

1. Chapter One: Introduction

1) Introduction and Background

Imaging of concrete structures in a non-destructive way means obtaining a visual rep-representation of the interior of structural concrete without damaging it. Concrete is a composite material that is mostly made of cement, water, fine and coarse aggregates, and additives. Grain sizes and properties of the constituent materials vary in each structure. Concrete is thus a complex and non-homogeneous material, which makes it

challenging for imaging [1]. Additionally, it is typically reinforced with some other materials

such as steel reinforcing bars (rebars) to overcome the concrete's weakness in tension. It has been decades since imaging technologies first found their way into non-destructive testing (NDT) of concrete structures. Many NDT methods have been introduced to image the interior of concrete such as radar imaging [2, 3, 4], ultrasonic echo imaging [5, 6, 7], ultrasonic tomography [8, 9], X-ray computed tomography (CT) [10, 11], and magnetic resonance imaging (MRI) [12]. The two most commonly used modalities for NDT of concrete structures are electromagnetic (or radar) waves and ultrasonic stress waves [13]. Multi-modal imaging, meaning that different modalities are used for imaging, has also been proposed [14, 15].

Subsequently, some general concepts and terms used in, and an overview of, this PhD dissertation is presented.

1.1. Ground Penetrating Radar

A ground penetrating radar (GPR) instrument emits an electromagnetic pulse into the material, typically along a path on the structure's surface. As the wave reaches an interface between two materials, a portion of the energy is reflected based on the dielectric constant (or relative permittivity) of the two materials. Per definition, air has a relative permittivity of 1. The relative permittivity of 20 ^{0}C water is approximately 80, while concrete is in the range of 6 to 11 [13]. The higher the water content of the concrete, the higher its relative permittivity. Structural concrete is usually reinforced with metallic rebars. Since metal has a dielectric constant of infinity, they reflect all of the wave energy. Hence, GPR is an excellent tool to detect rebars in concrete. In addition, GPR has been used to estimate the level of corrosion [16] and moisture variations [17]. For concrete applications, an electromagnetic pulse higher than 1 GHz frequency is usually used. The higher the frequency of the wave, the shorter the wavelength, which results in a higher resolution. However, lower frequencies can penetrate deeper. GPR units usually have one transmitter and one receiver as, shown in Figure 1-1.
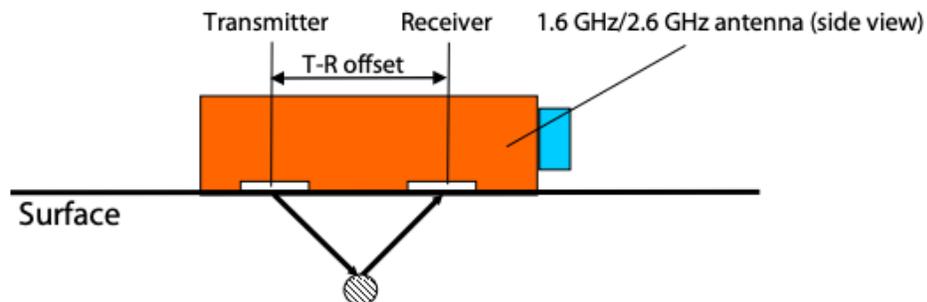
Figure 1-1 Illustration of GPR unit with one transmitter and one receiver, credit of GSSI, Inc [18].

1.2. Ultrasonic Testing

An ultrasonic echo array (UEA) can be used for ultrasonic testing and consists of multiple transducers that both emit and receive stress waves. UEAs usually use a shear stress wave pulse into the material, which is subsequently received by all other transducers. As the wave reaches the interface between two materials, a portion of the energy is reflected based on the difference in the acoustic impendence of the two materials. The transducer frequency of UEAs typically ranges from 50 to 250 kHz for concrete applications [6]. Higher frequencies result in lower wavelengths, i.e., higher resolution, but higher attenuation of the wave. Figure 1-2 shows an illustration of a UEA, where one transducer is sending a wave into the material, and the other transducers are receiving it. The red lines represent the direct wave paths.
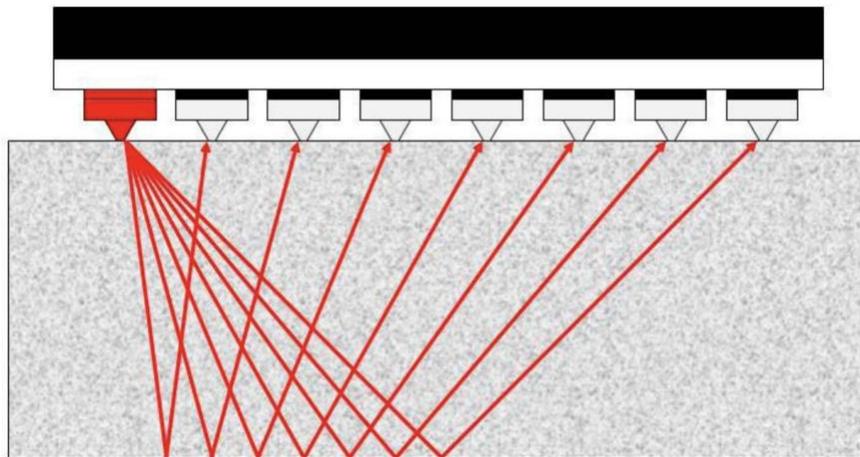
Figure 1-2 Illustration of UEA with eight channels, credit of Proceq, Inc [19].

1.3. Image Reconstruction

1.3.1. Pulse Echo Setup

A pulse echo setup is where both the emitting and receiving transducers are located on the same surface of a specimen. The measurement principle is based on reflection, i.e., a wave is emitted into the material and its reflections are recorded and analyzed. In all experiments of this PhD dissertation, the setup is pulse echo, for both GPR and UEA.

1.3.2. A-scan and B-scan

An A-scan is a 1-D time history – amplitude signal, that is collected back by the receiving transducer. This A-scan consists of possible reflections from interior objects and noise. A collection of A-scans presented in a 2D image is called a B-scan. The vertical axis in a B-scan is the time axis of the A-scans and the amplitudes of the A-scans are shown with shades of gray or a colormap in the B-scan image. The horizontal axis of a B-scan is the number of A-scans. Figure 2-2 in Chapter Two shows a typical A-scan and B-scan collected from a GPR.

1.3.3. Synthetic Aperture Focusing Technique

The synthetic aperture focusing technique (SAFT) is a numerical algorithm used to reconstruct an image given signals received at many aperture points using coherent superposition [5]. For a two-channel instrument without overlapping measurements (See Figure 1-3), the basic SAFT image is obtained via the following equation:

$$I(x_n, y_n) = \sum_m X(t_T + t_R + \epsilon) \tag{1}$$

where m is the number of scans, ϵ is a time offset parameter, t_T and t_R are the travel time between the emitting and receiving transducers to the pixel (or a possible object) of interest, respectively. In the process, each pixel is assumed as a potential reflector, and the signal amplitudes corresponding to that pixel are superimposed for all measurement positions. The travel times, t_T and t_R can be directly computed by dividing the distances d_T and d_R (shown in Figure 1-3) by the velocity of the medium. This equation holds true if there is a constant velocity across the medium.
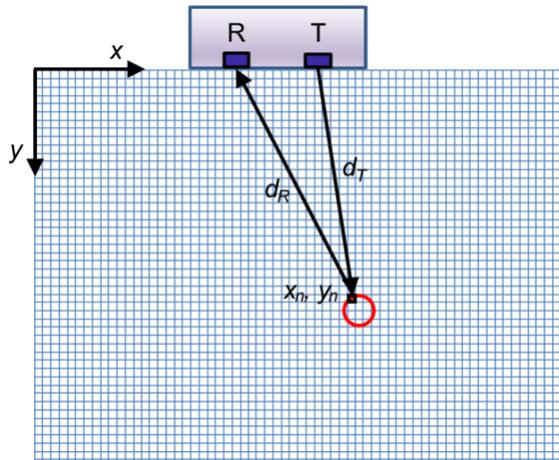
Figure 1-3. Illustration of the SAFT process for a simple two-channel instrument with non-overlapping measurements: The grid delineates the individual pixels. T and R denote transmitter and receiver, respectively.

1.4. Machine Learning and Generalization

A machine learning algorithm is an algorithm that can learn from data. Considering a training dataset (X, Y) where X is the input, Y is the label (output); a supervised algorithm learns a function to map the inputs to the outputs (target labels) [20]. The ideal model would result in a decision boundary (hypothesis) to understand the differences between

different classes (classification) or to predict a continuous variable (regression). If the learned decision boundary is close to the ground truth, then the model has generalization capability. The error is the difference between the predictions and the ground truth which can be decomposed into three parts:

$$E\left(\mathbf{Y} - \hat{\mathbf{Y}}\right)^2 = E\left[f(\mathbf{X}) - \hat{f}(\mathbf{X}) + (\varepsilon)\right]^2 = \mathbf{Var}\left(\hat{f}(\mathbf{X})\right) + \mathbf{Var}(\varepsilon) + \left[\mathbf{Bias}\left(\hat{f}(\mathbf{X})\right)\right]^2 \quad (2)$$

Where $\hat{\mathbf{Y}}$ is prediction for $\mathbf{Y}$, f is the ground truth, $\hat{f}$ is the learned hypothesis, $\mathbf{Var}\left(\hat{f}(\mathbf{X})\right)$ is the variance of the model, $\left[\mathbf{Bias}\left(\hat{f}(\mathbf{X})\right)\right]^2$ is the bias of the model and ε is the Bayes error.

The model is then used to predict unseen data (generalization). A good model is a model that had learned the underlying distribution of the data (low bias) and can also predict well the unseen data, i.e., has good generalization ability (low variance). For example, if one trains a model on the GPR data collected on only one concrete bridge from one instrument, or simulates a dataset with a fixed antenna frequency, the learned model may not generalize well on the data collected on other bridges or other instruments. Variance is dependent both on the data and the model, but bias only depends on the model. If we use complex models, we will achieve low bias, but we may overfit to it, and the model can then not generalize on new cases. If we reduce the complexity of the model (for example, using a linear model instead of a highly non-linear neural network), the model may generalize better but there is a risk of underfitting to the data (high bias). This trade-off needs to be contemplated until we achieve a good model with low bias and variance.

In statistical classification [21], Bayes error rate is the lowest possible error rate for any classifier and is called irreducible error. For example, in flipping a coin, we know exactly what process generates the outcome (a binomial distribution). However, if our model wants to predict the outcome of a series of coin flips, there will be errors because the process is inherently random. In real-world measurements, there might be uncertainties in our measurements that are random, and we may not be aware of them. This is the reason why many studies in the lab or on numerical models will fail when deployed on real world applications.

1.5. Deep Learning and Convolutional Neural Networks

Deep learning is a specific kind of machine learning [22] that uses of multilayer stack of modules, that all or most of it can learn and adjust their parameters to compute a nonlinear input-output mapping. They are also called deep neural networks. Deep learning methods are representation learning that takes a raw input and can output the desired output. Hence, they differ from traditional machine learning algorithms where the features are handcrafted and then fed to the model. The term deep refers to the depth of the neural network, where a model is consisted of multiple layers of hidden units between an input and output layer. Each layer in a deep learning model learns a representation from raw data where it becomes a more abstract representation in the next layer [23]. Many of deep neural network architectures are in the category of feedforward neural network since the information flow is from the input to the hidden layers and then output. If the outputs of the model are fed back to itself as feedback, they are called recurrent neural networks which are mostly used in sequential data processing such as language [22].

Convolutional neural network (CNN) is a type of deep learning that uses convolution operators in at least one of its layers [22]. Convolutional networks have been tremendously successful in practical applications, especially in image recognition tasks where a large, labeled dataset is available [24]. Convolution is a linear operator between a kernel (filter) (K) and an input (e.g., image, I) and can be formulated as follows:

$$S(i,j) = (K * I)(i,j) = \sum_m \sum_n I(i - m, \ j - n)K(m,n) \tag{3}$$

The filters in convolutional layers have a fixed width and height (m, n) that determine the local receptive field of a single unit within the layer. The output $S(i, j)$ is the filtered image and is called a feature map in machine learning.

In the traditional model of pattern recognition, kernels were hand-crafted that can extract relevant information from the input and eliminate noise [25]. For example, $K = \begin{bmatrix} 1 & 0 & -1 \\ 0 & 0 & 0 \\ -1 & 0 & 1 \end{bmatrix}$ is a 3×3 edge detector kernel. In a CNN, convolutional layers are not hand-crafted, but the parameters are learned via model training with backpropagation. Usually, the early layers in a CNN learn more traditional features such as edges and lines, but the later layers learn more abstract features.

A CNN usually consists of convolutional and pooling layers. An example of a CNN architecture is provided in Chapter 4 (See Figure 4-4). The pooling layers subsample the previous layers to contain the most important features of the previous feature map. The pooling layers indeed reduce the spatial resolution of a feature map and reduce the sensitivity of the output to distortions together with the weight-sharing capability of CNNs

[26]. Weight sharing refers to the use of the same weights in a given filter applied on a feature map. This also reduces the complexity and training time of a CNN model in comparison with a fully connected layer.

1.6.   Outline of Dissertation

This PhD dissertation follows the multi-paper format per PSU OGS guidelines. Each chapter is a recent publication or a draft for a publication and is organized as follows:

Chapter One: Introduction

Chapter Two (Paper One): A Pipeline for Enhanced Multimodal 2D Imaging of Concrete Structures. An imaging pipeline to achieve enhanced images of the interior of concrete from ground penetrating radar (GPR) and ultrasonic echo array (UEA) measurements is introduced. This work lays the foundation for an advanced yet practical imaging tool to assess concrete structures. Specifically, an enhanced two-dimensional (2D) total focusing method (XTFM) to reconstruct images from raw GPR and UEA data is proposed. The proposed XTFM algorithm integrates the total focusing method (TFM) and synthetic aperture focusing technique (SAFT) concepts to post-process large independent and interelement measurements from both modalities in a computationally efficient way. Furthermore, a novel 2D image fusion algorithm using wavelet multilevel decomposition and an NDT knowledge-based rule to fuse GPR and UEA images is introduced. The algorithm is compared with conventional fusion algorithms such as averaging, maximum, and product. The results from three laboratory concrete reference specimens are evaluated in detail. The fused images are compared with each other as well as benchmarked with the

original GPR and UEA images. A set of image quality metrics is proposed. The output image obtained from our proposed pipeline is an enhanced 2D image of the interior of concrete structures that eases interpretation by a human inspector as well as it has the potential to improve interpretation by computer vision and image analysis algorithms.

Chapter Two is published as a journal article in the journal Materials and Structures:

All data and algorithms introduced in the article are open-source and available at: https://github.com/Sinamhd9/A-Pipeline-for-Enhanced-Multimodal-Imaging-of-Structural-Concrete.

Chapter Three (Paper Two): Damage Tracking of Full-scale Pre-1990s Reinforced Concrete Bridge Members During Reverse-Cyclic Loading Using Fusion-based Imaging. Fusion-based imaging using ground penetrating radar (GPR) and ultrasonic echo array (UEA) measurements is used to track damage progression of two full-scale reinforced concrete (RC) bridge column-footing subassembly specimens with different lap-splice detailing. The laboratory specimens were subjected to reverse-cyclic lateral loading following the Cascadia Subduction Zone (CSZ) loading protocol. Two vertical GPR and UEA scans were performed on each of the columns' east and west faces at select ductility levels. Images from the interior of the columns were reconstructed using the pipeline developed in Chapter Two, the extended total focusing method (XTFM), and a wavelet-

based fusion technique. Finally, the images from the two sides were fused together to create two composite images of the interior of each column. A qualitative analysis based on the structural similarity (SSIM) index of the reconstructed images was found to capture damage progression well. A so-called backwall analysis is also presented, in which the amplitude of the backwall reflector was used to track damage progression. This quantitative analysis shows that changes in the images can be detected as early as the first measurement, which in this study was at a ductility level, $\mu = 0.5$. Moreover, the changes along the height of the column vary, and are consistent with the higher damage at the bottom of the column. Finally, a comparison between the two columns is presented. In conclusion, fusion-based imaging can be used to track and characterize damage progression in full-scale RC members adequately.

This article will be submitted to Journal of Nondestructive Evaluation.

Chapter Four (Paper Three): A Deep Learning and Simulation Pipeline for Image Reconstruction of GPR Data. Image reconstruction on ground penetrating radar (GPR) B-scan data is usually performed with synthetic aperture focusing and migration techniques, which require prior knowledge of several parameters. For example, in the extended total focusing method (XTFM) algorithm, an accurate dielectric constant of the media, as well as an offset parameter, are required to reconstruct a focused image from the interior of a media, herein, reinforced concrete. Traditionally, this is done by a manual calibration process that requires knowledge about the depth of multiple reflectors in a structure. Deep neural networks can learn meaningful representations from raw data. In this study, we introduce a simulation and deep learning pipeline to generate high quality

datasets, as well as learn from them. We propose a neural network model that can predict the dielectric constant of the media and the offset parameter, and thus, can reconstruct the focused image with high accuracy. In addition, we use model explainability techniques such as gradient visualization to show which areas of the images the algorithm is utilizing in the prediction process. We test the algorithm on real-world data from Chapter 2 and Chapter 3 and discuss the generalizability of it. In conclusion, the model performs has an excellent performance on the simulated data with an R2 coefficient of higher than 0.999 on both parameters. It has also been found that the neural network pays the most attention to the angle of reflections and the shape of a hyperbole resulting from a point reflector to predict the dielectric constant, and surface wave portion of GPR to predict the offset parameter.

This article will be submitted to Journal Automation in Construction.

Chapter Five: Conclusion and Outlook.

1.7. References

[1]   Büyüköztürk, O. (1998). Imaging of concrete structures. Ndt & E International, 31(4), 233-243.

[2]   Clem, D. J., Schumacher, T., & Deshon, J. P. (2015). A consistent approach for processing and interpretation of data from concrete bridge members collected with a hand-held GPR device. *Construction and Building Materials*, 86, 140-148.

[3]   Sun, H., Pashoutani, S., & Zhu, J. (2018). Nondestructive evaluation of concrete bridge decks with automated acoustic scanning system and ground penetrating radar. *Sensors*, 18(6), 1955.

[4]   Lai, W. W. L., Derobert, X., & Annan, P. (2018). A review of Ground Penetrating Radar application in civil engineering: A 30-year journey from Locating and Testing to Imaging and Diagnosis. *NDT & E International*, 96, 58-78.

[5]   Schickert, M., Krause, M., & Müller, W. (2003). Ultrasonic imaging of concrete elements using reconstruction by synthetic aperture focusing technique. *Journal of Materials in Civil Engineering*, 15(3), 235-246.

[6]   Krause, M., Mielentz, F., Milman, B., Müller, W., Schmitz, V., & Wiggenhauser, H. (2001). Ultrasonic imaging of concrete members using an array system. *NDT & E International*, 34(6), 403-408.

[7]   Bittner, J. A., Spalvier, A., & Popovics, J. S. (2018). Internal Imaging of Concrete Elements. *Concrete International*, 40(4), 57-63.

[8]   Choi, H., & Popovics, J. S. (2015). NDE application of ultrasonic tomography to a full-scale concrete structure. IEEE transactions on ultrasonics, ferroelectrics, and frequency control, 62(6), 1076-1085.

[9]   Choi, H., Bittner, J., & Popovics, J. S. (2016). Comparison of ultrasonic imaging techniques for full-scale reinforced concrete. *Transportation Research Record,* 2592(1), 126-135.

[10]   Balázs, G. L., Lublóy, É., & Földes, T. (2018). Evaluation of concrete elements with X-ray computed tomography. *Journal of Materials in Civil Engineering*, 30(9), 06018010.

[11]   Moosavi, R., Grunwald, M., & Redmer, B. (2020). Crack detection in reinforced concrete. *NDT & E International*, 109, 102190.

[12]   Marfisi, E., Burgoyne, C. J., Amin, M. H. G., & Hall, L. D. (2005). The use of MRI to observe the structure of concrete. *Magazine of concrete research*, 57(2), 101-109.

[13]   ACI-American Concrete Institute. (2013). 228: 2R-13 Report on nondestructive test methods for evaluation of concrete in structures.

[14]   Kohl, C., Krause, M., Maierhofer, C. and Wöstmann, J., (2005). "2D-and 3D-visualisation of NDT-data using data fusion technique." *Materials and Structures*, Vol. 38(9), pp: 817-826.

[15]   Maierhofer, C., Zacher, G., Kohl, C., & Wöstmann, J. (2008). Evaluation of radar and complementary echo methods for NDT of concrete elements. *Journal of Nondestructive Evaluation*, 27(1-3), 47.

[16]   Tešić, K., Baričević, A., & Serdar, M. (2021). Non-Destructive Corrosion Inspection of Reinforced Concrete Using Ground-Penetrating Radar: A Review. *Materials*, *14*(4), 975.

[17]   Hugenschmidt, J., & Loser, R. (2008). Detection of chlorides and moisture in concrete structures with ground penetrating radar. *Materials and Structures*, *41*(4), 785-792.

[18]   Geophysical Survery Systems, Inc (2017), *Concrete Handbook*, New Hampshire 03060-3075 USA, www.geophysical.com

[19]   Proceq SA, (2017) *Pundit operating instructions*, Schwerzenbach, www.screeningeagle.com

[20]   Shalev-Shwartz, S., & Ben-David, S. (2014). *Understanding machine learning: From theory to algorithms*. Cambridge university press.

[21]   James, G., Witten, D., Hastie, T., & Tibshirani, R. (2013). *An introduction to statistical learning* (Vol. 112, p. 18). New York: springer.

[22]   Goodfellow, I., Bengio, Y., & Courville, A. (2016). *Deep learning*. MIT press.

[23]   LeCun, Y., Bengio, Y., & Hinton, G. (2015). Deep learning. *nature*, *521*(7553), 436-444.

[24]   Deng, J., Dong, W., Socher, R., Li, L. J., Li, K., & Fei-Fei, L. (2009, June). Imagenet: A large-scale hierarchical image database. In *2009 IEEE conference on computer vision and pattern recognition* (pp. 248-255). Ieee.

[25]   LeCun, Y., & Bengio, Y. (1995). Convolutional networks for images, speech, and time series. *The handbook of brain theory and neural networks*, *3361*(10), 1995.

[26]   LeCun, Y., Bottou, L., Bengio, Y., & Haffner, P. (1998). Gradient-based learning applied to document recognition. *Proceedings of the IEEE*, *86*(11), 2278-2324.

2. Chapter Two: A Pipeline for Enhanced Multimodal 2D Imaging of Concrete Structures

Sina Mehdinia[1], Thomas Schumacher[2], Xubo Song[3], and Eric Wan[4]

Mehdinia, S., developed specimens and algorithms, collected measurements, analyzed data, and drafted the paper; Schumacher, T., developed specimens, collected measurements, contributed to data analysis, review and editing; Song, X., investigation, review and editing; Wan, E., investigation, review and editing.

---

[1]PhD Candidate, Department of Civil and Environmental Engineering, Portland State University, Portland, OR, USA, E-mail: mehdinia@pdx.edu
[2]PhD, PE, Associate Professor, Department of Civil and Environmental Engineering, Portland State University, Portland, OR, USA, E-mail: thomas.schumacher@pdx.edu
[3]PhD, Professor, School of Medicine, Oregon Health and Science University, Portland, OR, USA, E-mail: songx@ohsu.edu
[4]PhD, Research Associate Professor, Department of Electrical Engineering, Portland State University, Portland, OR, USA, E-mail: eric.wan@pdx.edu

Abstract

We present an imaging pipeline to achieve enhanced images of the interior of concrete from ground penetrating radar (GPR) and ultrasonic echo array (UEA) measurements. This work lays the foundation for an advanced yet practical imaging tool to assess concrete structures. Specifically, we propose an enhanced two-dimensional (2D) total focusing method (XTFM) to reconstruct images from raw GPR and UEA data. The proposed XTFM algorithm integrates total focusing method (TFM) and synthetic aperture focusing technique (SAFT) concepts to post-process large independent and interelement measurements from both modalities in a computationally efficient way. Furthermore, we introduce a novel 2D image fusion algorithm using wavelet multilevel decomposition and an NDT knowledge-based rule to fuse GPR and UEA images. We then compare our algorithm with conventional fusion algorithms such as averaging, maximum, and product. The results from three laboratory concrete reference specimens are evaluated in detail. The fused images are compared with each other as well as benchmarked with the original GPR and UEA images. The output image obtained from our proposed pipeline is an enhanced 2D image of the interior of concrete structures that eases interpretation by a human inspector as well as has it the potential to improve interpretation by computer vision and image analysis algorithms.

18

2.1. Introduction and Background

It has been decades since imaging technologies first found their way into non-destructive testing (NDT) of concrete structures. Many NDT methods have been introduced to image the interior of concrete such as radar imaging [1, 2, 3], ultrasonic echo imaging [4, 5, 6], ultrasonic tomography [7, 8], X-ray computed tomography (CT) [9, 10], and magnetic resonance imaging (MRI) [11]. All these modalities have their own limitations [12, 13]. The two most used modalities for NDT of concrete structures are electromagnetic (or radar) waves and ultrasonic stress waves. Both have their strengths and weaknesses, stemming from their underlying physics principles [14]. For example, virtually all the energy of an electromagnetic wave produced by a ground penetrating radar (GPR) instrument is reflected when arriving at a metallic object such as a steel reinforcing bar (or rebar) in reinforced concrete. On the other hand, a significant portion is transmitted through concrete-air interfaces such as an internal crack or void. Conversely, ultrasonic stress waves can penetrate through a metallic object, but most of the energy is reflected at a concrete-air interface. Furthermore, scattering and attenuation patterns are different for these two modalities, so is the speed of data collection [15]. Langenberg et al. discuss the underlying theory of electromagnetic and ultrasonic stress wave imaging in the context of NDT on concrete [16].

Image fusion is the process of combining and merging complementary information into a single image from two or more source images, which generates an improved visualization, and benefits from different NDT methods, especially when they are complementary in nature [15]. There are two main reasons to perform multimodal image fusion [17]. The first

19

one is to achieve an improved visual representation of an image with higher overall quality, thus improving a human inspector's ability to determine features of interest. The second one is to produce a single image that has the information content from both modalities for subsequent computer vision and image processing algorithms such as image segmentation. For multimodal image fusion, it is desirable to preserve relevant and complementary information while reducing noise and providing an enhanced visual representation [18]. In this study, image fusion is performed at the pixel level, where the fused image is obtained from the corresponding pixel values of the source images.

Kohl et al. [15] published the first research on data fusion of ultrasonic and GPR images on concrete where they evaluated different arithmetic rules such as mean, substitution, and maximum to fuse the images. In addition, they employed the maximum amplitude of both modalities on datasets of different sizes. The authors reported that maximum information content was achieved using their approach for concrete structures with high reinforcement density and/or air voids. They did not propose any metrics that would allow for evaluating image quality. In a similar study, Maierhofer et al. [19] performed data fusion of GPR and UEA data from concrete structures. The authors used the maximum amplitude method and reported that maximum information was obtained in structures with a high reinforcement density, tendon ducts, and/or air voids and gaps. Like [15], they did not use any metrics to quantify information or image quality. Van der Wielen et al. [20] used ultrasonic and GPR measurements on concrete pavement and compared the results. They found that GPR is more efficient for dowel positioning and found both useful in thickness estimation. Krause et al. [21] compared ultrasonic echo, GPR and impulse-echo methods on concrete. They

compared the modalities in terms of measuring thickness, location of a metal duct and voided regions inside the duct. They found that all the modalities are useful in measuring thickness and location of the duct. They also found that GPR is not suitable to detect the voids inside the ducts while UEA is. Gucunski [22] et al. reported a comparison of some NDT methods including GPR and ultrasonic pulse echo in condition assessment of concrete bridge decks. They categorized different NDT technologies and reported that both GPR and ultrasonic pulse echo have good potential in detecting delaminations and deterioration. Wimsatt et al. [23] reported combining three datasets from ultrasonic echo, impact echo, and GPR obtained from tunnel inspection using weighted averaging. They applied depth-varying weights to each image to account for different resolutions and penetration depths. They reported that the fused images provide useful information from each modality in a concise combined presentation.

Salazar et al. used fusion of GPR and ultrasound images on a historic masonry wall using the mean and product results of the two images [24]. They reported improved defect detection in the fused image, especially with the mean method, but without the support of any image quality metrics. Not applied to images but related, Volker and Shokouhi applied two data fusion algorithms, namely Dempster's rule of combination and the Hadamard product for GPR, impact echo, and ultrasonic pulse echo data to automatically detect honeycombing in concrete [25]. They evaluated their method quantitatively by comparing receiver operating characteristic (ROC) curves for individual tests and fusion methods. Results from both fusion algorithms were slightly better compared to when a single modality was used. They also investigated clustering methods for fusing GPR, impact echo,

and ultrasonic data to detect honeycombing in another study [26] and found that the density-based clustering algorithm performed well on the classification task between defect and non-defect features.

Summarizing the state-of-the-art in imaging of concrete structures, we make the following observations: (1) Reconstruction algorithms are not cohesive among GPR and UEA modalities, and hence there is a lack of well-defined holistic pipeline, (2) image fusion for concrete applications has still many opportunities for improvement, (3) few studies have proposed quantitative metrics to evaluate fusion performance, and (4) no advanced automated diagnostic algorithms have been developed to quantitatively analyze images.

The main contribution of this study is a comprehensive pipeline for enhanced multimodal 2D imaging of concrete structures that span the first three points above. First, we present an integrated algorithm to reconstruct GPR and UEA images from raw independent and interelement measurements. Second, we introduce a fusion algorithm based on multilevel wavelet decomposition and an NDT-informed fusion rule. Third, we evaluate the quality of each image in terms of two standard types of reflectors and compare the image quality between the original GPR, UEA and fused images. The overall goal is to lay the foundation for an advanced yet practical diagnostic imaging tool for concrete structures. This pipeline has the potential to be used in conjunction with image analysis methods such as deep learning to build a prognostics tool in the future if a proper amount of valid data is available.

2.2. Experimental Setup

2.2.1. Test Specimens

Three specimens with different geometries and known features were built in the laboratory using a standard normal-weight concrete with a specified compressive strength of 31 MPa (4500 psi). The outside dimensions of all specimens are length x width x depth = 1219 x 610 x 305 mm (48 x 24 x 12 in). Figure 2-1 (a) shows Specimen 1, which is unreinforced and varies in depth from 51 to 305 mm (2 to 12 in) in steps of 51 mm (2 in). Figure 2-1 (b) shows Specimen 2, which contains five #4 [bar diameter, d_b = 13 mm (0.5 in)] steel rebars having rebar clear covers, c_c on the top and bottom side ranging from 25 to 127 mm (1 to 5 in) and 165 to 267 mm (6.5 to 10.5 in), respectively. Finally, Specimen 3, which is shown in Figure 2-1 (c), has a row of rebars on each the top and bottom side with a constant rebar clear cover, c_c = 76 mm (3 in). The rebars on the top and bottom side range from #4 to #8 [d_b = 12.7 to 25 mm (0.5 to 1 in)] and #9 to #11 [d_b = 29 to 36 mm (1.13 to 1.41 in)]. The bottom side also has four closely-spaced #4 [d_b = 13 mm (0.5 in)] rebars as well as a hollow 51 mm (2 in) diameter PE pipe.
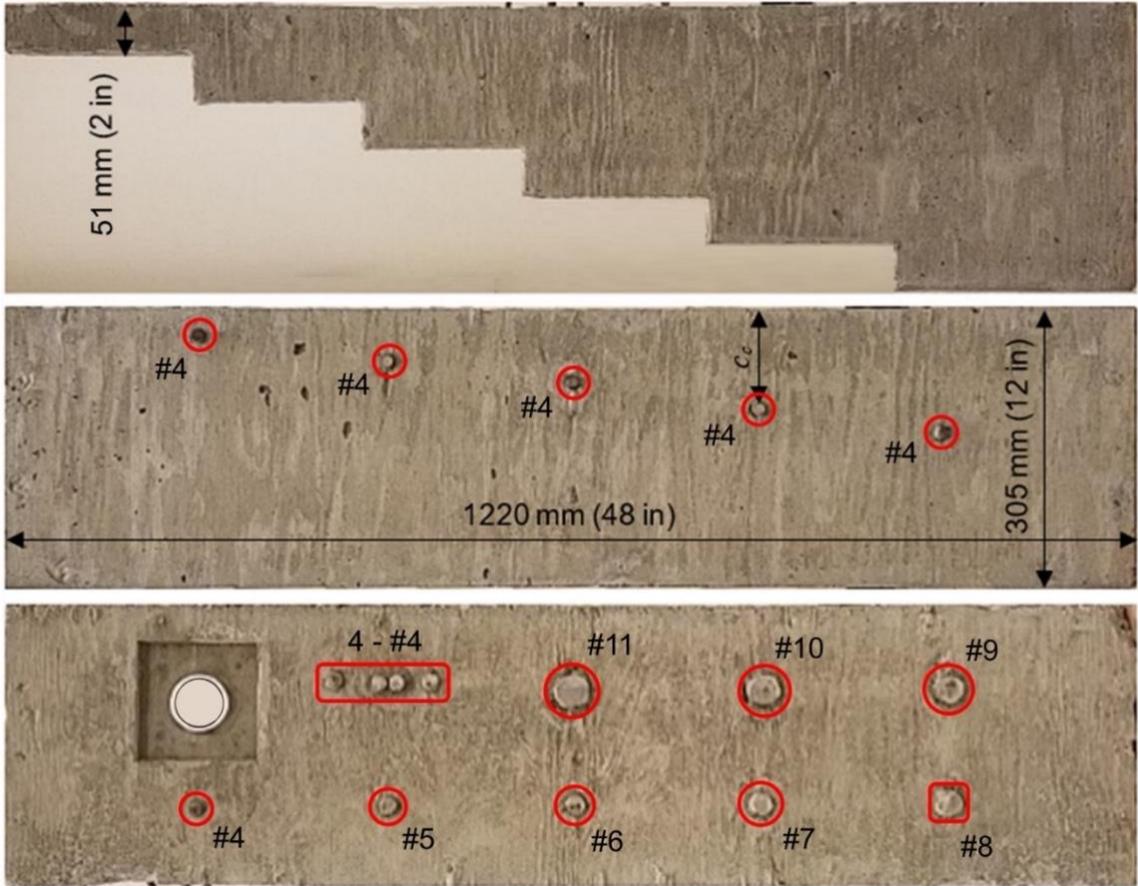
Figure 2-1 Photos (rectified elevations views) of three reference specimens (top to bottom): Specimens 1, 2, and 3. Rebars are highlighted with red circles/rectangles.

2.3. Methodology

2.3.1. Instruments and Data Collection

Two measurement modalities are utilized in this research both using a pitch-catch configuration: electromagnetic waves and ultrasonic stress waves. For the electromagnetic waves, a hand-held ground penetrating radar (GPR) instrument from GSSI, Model StructureScan Mini XT was employed [see photo in Figure 2-2 (a)]. The instrument is equipped with one transmitting and one receiving antenna (subsequently referred to as

24

transducer). It emits an electromagnetic pulse that is transmitted into the material along a path on the structure's surface, as shown on the photo in Figure 2-2 (c). A portion of the incident electromagnetic pulse is reflected at interfaces between materials with different dielectric properties [14]. Figure 2-2 (b) and (d) show a typical individual measurement (or A-scan signal) and a contour plot of subsequent A-scan signals (or B-scan plot), respectively, of unprocessed GPR data. Technical details are provided in Table 2-1.
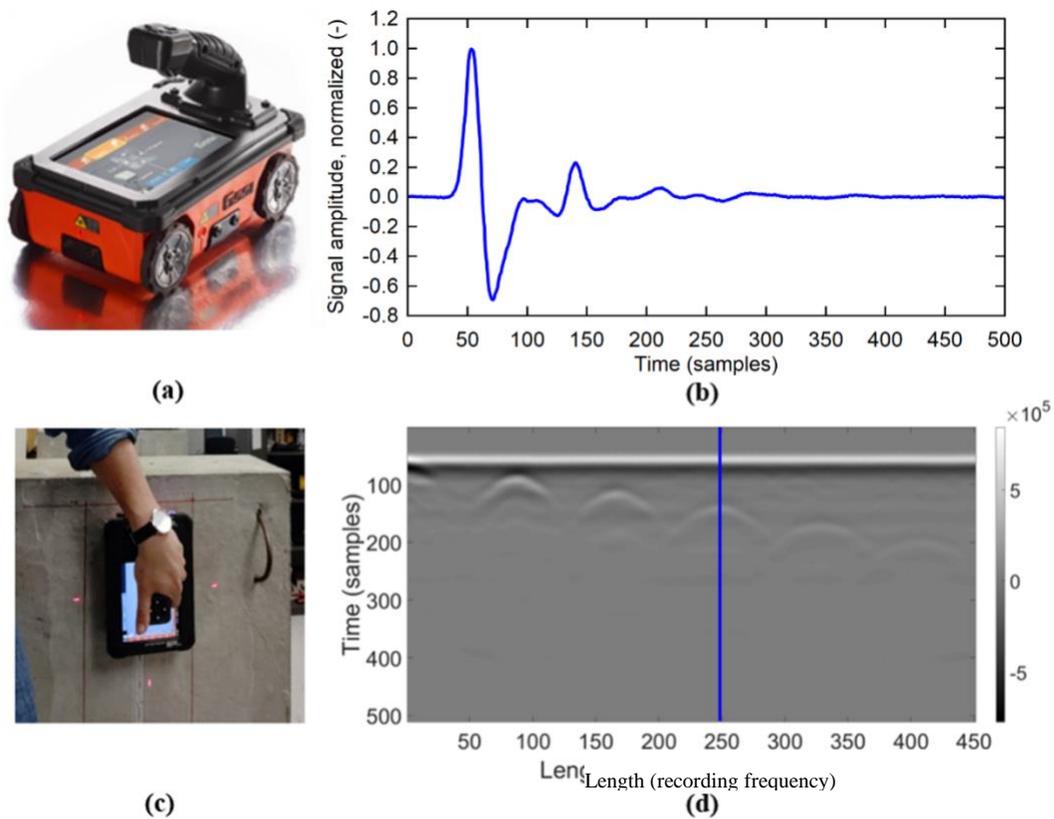
Figure 2-2. Ground penetrating radar (GPR) measurements: (a) Photo of instrument (Manufacturer, model: GSSI, StructureScan Mini XT), (b) typical A-scan signal (unprocessed), (c) Photo taken during data collection, and (d) typical B-scan plot from independent measurements (unprocessed). The blue line in (d) marks the location of the A-scan signal shown in (b).

For the ultrasonic stress waves, an ultrasonic echo array (UEA) instrument from Proceq, Model Pundit 250 Array, was used [see photos in Figure 2-3 (a) and (c)]. The instrument is equipped with 24 ultrasonic transducers, arranged in an 8 x 3 array. It emits a shear stress wave pulse row-by-row into the material, which is subsequently received by all other transducers. A portion of the incident stress wave is reflected at interfaces between materials with different acoustic impedances [14]. Figure 2-3 (b) and (d) show a typical A-scan signal and B-scan plot, respectively of unprocessed ultrasonic echo data. The transducer frequency is 50 kHz with a sampling frequency of 1 μs. Table 2-1 shows a comparison between the properties of the GPR and UEA instruments.
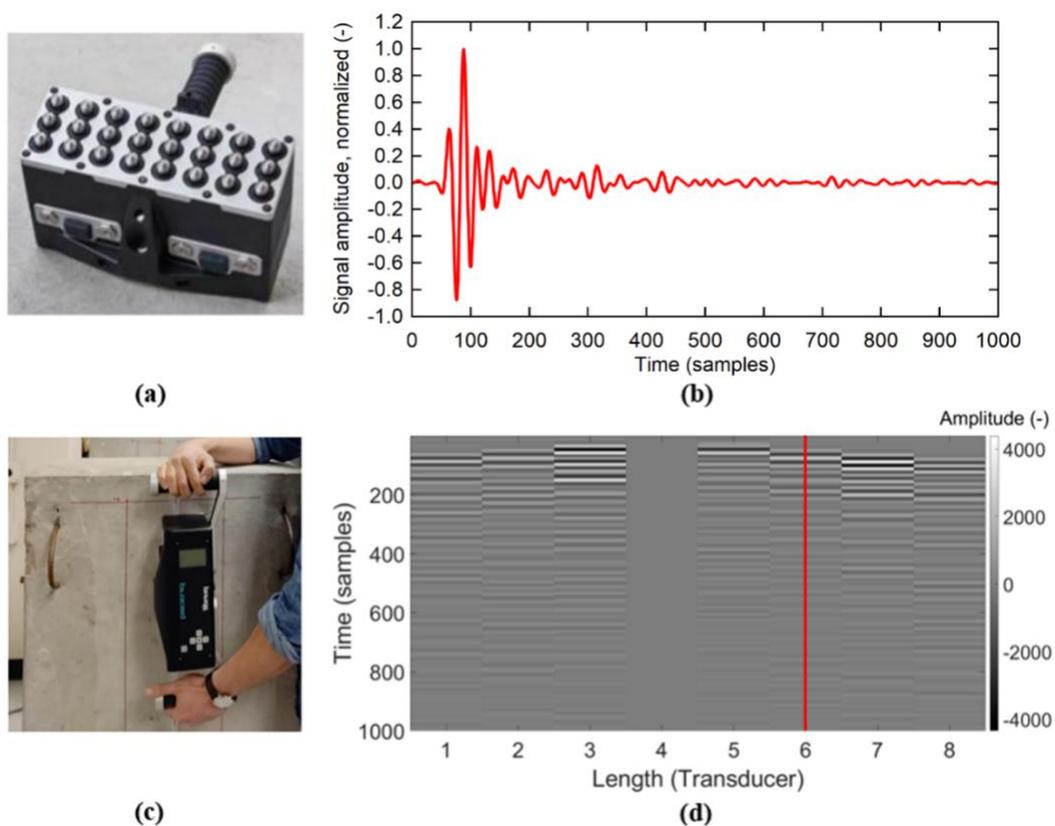
Figure 2-3. Ultrasonic echo array (UEA) measurements: (a) Photo of instrument (Manufacturer, model: Proceq, Pundit 250 Array); (b) typical A-scan signal

(unprocessed), (c) Photo taken during data collection, and (d) typical B-scan plot from interelement measurements (unprocessed). The red line in (d) marks the location of the A-scan signal shown in (b).

Table 2-1. Technical details of the two utilized instruments.

Instrument	GPR	UEA
Wave type	Electromagnetic	Stress (shear) wave
Central pulse frequency	2.7 GHz	50 kHz
Signal Resolution	0.0164 ns	1 µs
Recording frequency	2.54 mm (0.1 in) (fixed)	10 mm (0.394 in) (selected for this study)
Number of transducer rows, transducers/row	2, 1	8, 3[1]
Transducer spacing(s)	40 mm (1.58 in)	30 mm (1.18 in)

[1]The instrument records across all three transducers in one row and then computes and saves the average signal.

2.4. Pipeline Methodology

2.4.1. Image Reconstruction

In this research, an integrated approach based on the total focusing method (TFM) [27, 28] and the synthetic aperture focusing technique (SAFT) [4] was employed that can be used to reconstruct 2D images for both modalities. TFM utilizes the full aperture to reconstruct the image by synthetically focusing on every pixel of interest, while SAFT uses independent recordings [29, 30]. Our reconstruction approach uses measurements that contain both interelement data of the array as well as independent overlapping

measurements and works for both GPR and UEA modalities. We propose the term XTFM (extended total focusing method) because it considers overlapping measurements and works across modalities, i.e., it can process both GPR and UEA data. Overlapping measurements return an independent array response at different positions where there is a dependent interelement response at each position. Therefore, a large matrix of measurements is collected that contains both interelement as well as independent array data. We treat each UEA measurement the same as one GPR recording where the UEA data are stored in the form of an nS x 1000 x 8×8 array, while The GPR data are in a nS x 512 x 2×2 array, with the diagonals consisting of zeros and the matrix being symmetric, meaning that only one signal is recorded between each transducer pair. nS is the total number of scans. For every measurement, the image area that can be covered by the signal length is used for reconstruction. Thus, the beam is not focused in any particular manner. We deliberately omit the enveloping of the signal (using the Hilbert Transform) that is often applied in practice since we find that it creates the illusion of a circular shape for circular objects like rebars. It should be noted that the GPR instrument used in this study is not an array GPR (it has only one emitter and receiver), however, our proposed XTFM algorithm works for any number of channels ≥ 2. The following pseudo-code shows the steps of the proposed algorithm. The actual code in Python and MATLAB can be downloaded at no cost from our GitHub repository [31].

2.4.2. Algorithm 1: Pseudocode for 2D XTFM

XTFM (**X**, *v*, *ε*, *sR*, *d*, s, *r, dim*)

Input:

X: 4D matrix of raw measurements containing all slices of independent and interelement data with the format of *nS* sL * nC * nC* , where *nS* is the number of independent scans, *sL is the signal length of a raw measurement* and *nC* is the number of channels of the instrument.
v: velocity of the medium
ε: time offset
sR: signal resolution
d: recording frequency
s: transducer spacing
r: desired resolution
dim: grid dimensions (2D)

Output: I (reconstructed image)

Initialize vectors, $\mathbf{x_n}$, $\mathbf{y_n}$ spanning from 0 to *dim* *r with a step of *r*

Initialize the output image, **I** with zeros with a size of *dim*

For every *k* independent measurement (total of *nS*)

    For every *i, j* interelement measurement (total of (*nC * (nC-1)/2*):

$$\textbf{Calculate T} \text{ matrix} = \left[\frac{\left(\frac{\sqrt{(x_n - i{*}s - k{*}d)\text{\textasciicircum}2 + y_n\text{\textasciicircum}2))} + \sqrt{(x_n - j{*}s - k{*}d)^2 + y_n^2}}{v} + \varepsilon \right)}{sR} \right]$$

       Mask T matrix to discard out of range values (values bigger than *sL*)

       Add X[*k*,**T**, *i, j*] to **I**

    End For

End For

Return I

The time variable, $\mathbf{T}$, is an array, computed by broadcasting the $\mathbf{x}_n$ and $\mathbf{y}_n$ vectors. The array $\mathbf{T}$ can be implemented using fancy indexing (i.e., passing an array of indices to access elements of an array at the same time) and broadcasted to the final image. Thus, it can make the process computationally more efficient. All indices in the $\mathbf{T}$ matrix contribute to the final image if they are less than the signal length. The other indices are discarded through the masking step. This can lead to adding more information to the image, as well as increasing the risk of adding potential artifacts. Both ε and v need to be determined experimentally, which aligns the images in the y-direction and results in the correct focus. The process involves tuning the two parameters until the known features such as rebars and the backwall are shown in their correct locations. The assumption is that both parameters are deterministic entities and can be applied uniformly throughout a specimen. While this is a reasonable assumption for the specimens used in our study, it might not be for a real structure with larger dimensions where concrete properties might vary spatially.

2.5. Image Fusion

2.5.1. Preprocessing

To keep the pipeline practical and general, an effort was made to minimize any manual preprocessing. The images should be aligned (or registered) correctly in the y-direction when the parameters ε and v were tuned correctly. Based on the geometry of the instruments and measurements, there might be a slight misalignment in the x-direction. Thus, the only image registration necessary in the x-direction before fusing the GPR and UEA images is translation in the x-direction. Finally, a conventional (and optional) surface

wave removal was applied to both GPR and UEA images and the images were min-max normalized to take amplitude values in the 0 to 1 range.

2.5.2. Wavelet image fusion

Wavelet image fusion is a multiresolution approach capable of handling different image resolutions while extracting the image content with the most pertinent information [32, 33, 34]. The fusion rule used here was informed by the nature of the measurements. The direct pulse recorded from a reflector follows one of these two patterns, which consist of a center and two side lobes: dark-bright-dark (i.e., low-high-low intensity), which we name Type 1 reflector and a bright-dark-bright (i.e., high-low-high intensity), which we name Type 2 reflector. Examples of the former and latter are embedded metals such as rebars and air voids or backwalls of the concrete, respectively. The other areas of an image where there is no reflector are usually shades of gray having some level of variation, or noise. Figure 2-4 shows (a) a sample reconstructed image having both reflectors as well as (b) a representative A-scan with the two reflectors highlighted by boxes. Our objective is to achieve high contrast for both types of reflectors, Type 1 as well as Type 2, so that they are clearly discernible from the background. For example, in the results section we discuss that from reconstructed images of Specimen 2, the GPR image shows all the rebars but it does not reveal the backwall. On the other hand, the UEA image clearly shows the backwall but the small rebars are missing. Generally, we observe higher attenuation of the radar waves, stronger reflection of radar wave energy on near-surface rebars, and higher penetration depth of the ultrasonic waves.
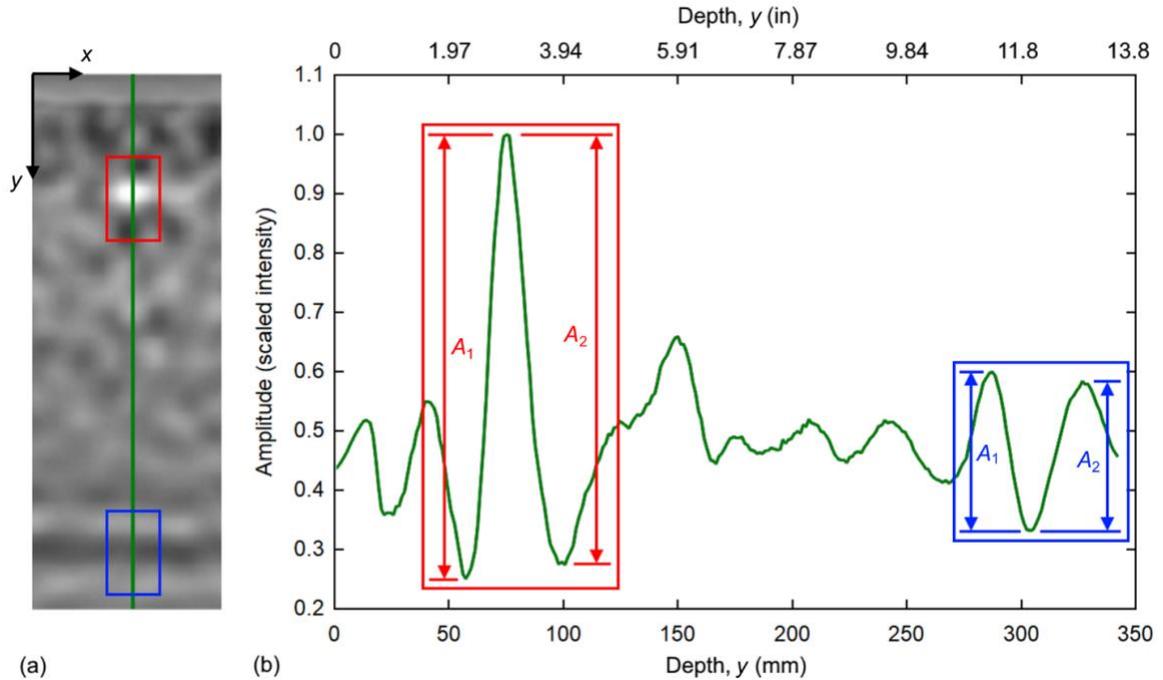
Figure 2-4. (a) Sample reconstructed image of Specimen 2 showing Type 1 (red box) and Type 2 (blue box) reflectors and (b) representative A-scan with the two reflectors highlighted by boxes [location indicated by green line in (a)].

We propose **Algorithm 2** based on the observations made from reconstructed 2D images of the three specimens and the underlying physics of the used modalities.

2.5.3. Algorithm 2: Proposed Image Fusion Algorithm

Step 1: Each image from the two modalities is decomposed via 2D multilevel wavelet decomposition into a low-frequency and three high-frequency detail coefficients for each level. The decomposition is performed recursively for a desired number of levels, for which we propose it being at least four. The Sym5 wavelet from the Symlets family is used in this study, which is suitable for 2D image processing applications [35].

Step 2: Each approximation is divided into three ranges of bright, dark, and gray based on the intensity of each pixel value. The thresholds to divide these three ranges are: pixel values > mean + one standard deviation, pixel values < mean - one standard deviation, and pixel values within mean +/- one standard deviation, respectively. The following rules are applied, based on the expected capabilities and reliabilities of the two modalities:

Case 1: If a feature is bright in the images of both modalities, e.g., the center lobe of a Type 1 reflector (e.g., a rebar in concrete), or the side lobes of a Type 2 reflector, we pick the maximum pixel value.

Case 2: If a feature is dark in the images of both modalities, e.g., the center lobe of a Type 2 reflector (e.g., the hollow pipe embedded in Specimen 3 or the backwall), or the side lobes of a Type 1 reflector, we select the minimum pixel value.

Case 3: If a bright feature is visible in the GPR image, and in the UEA image it is in the gray (i.e., mid-) range, we pick the pixel value from the GPR image.

Case 4: If a bright feature is visible in the UEA image and the GPR image shows it in the gray range, we select the mean value, since GPR is better suited for detecting bright reflectors (like a rebar).

Case 5: If a dark feature is visible in the GPR image and the UEA image shows it in the gray range, we pick the mean value.

Case 6: If a dark reflector is visible in the UEA image and the GPR image shows it in the gray range (like the backwall in Specimens 2 and 3), we select the pixel value from the UEA image.

Case 7: If a feature appears in the gray range in the images of both modalities, we pick the mean pixel value.

Case 8: If a feature is in the bright range of the GPR image and the dark range of UEA image, we select the pixel value of the bright feature.

Case 9: If a feature is in the bright range of the UEA image and dark range of the GPR image, we select the mean pixel value.

Step 3:

Adopt the maximum pixel value of the detail coefficients.

Step 4:

Perform multilevel wavelet reconstruction using the inverse wavelet transform to obtain the final fused image.

2.6.   Results and Discussion

2.6.1. Local Evaluation Metric

The aim of fusion is to enhance the quality (discernibility) of the features of interest and provide a single overall high-quality image capturing information from both modalities. Therefore, we suggest two types of metrics to evaluate the fused images. First, and the more important one, is a local metric to evaluate each reflector individually. As previously described, there are two types of reflectors with consecutive bright and dark regions. To measure the quality of a feature, we define a local contrast metric for each reflector as the contrast (relative intensity) of the local extrema on top of the feature. We measure this by adding relative intensities of the extrema amplitudes. Figure 2-4 (b) shows the amplitudes that are added together (e.g., $|A_1|+|A_2|$) to compute the value of the local contrast metric. This metric measures the saliency of the center lobe of the recorded pulse. Red and blue lines refer to Type 1 and Type 2 reflectors, respectively.
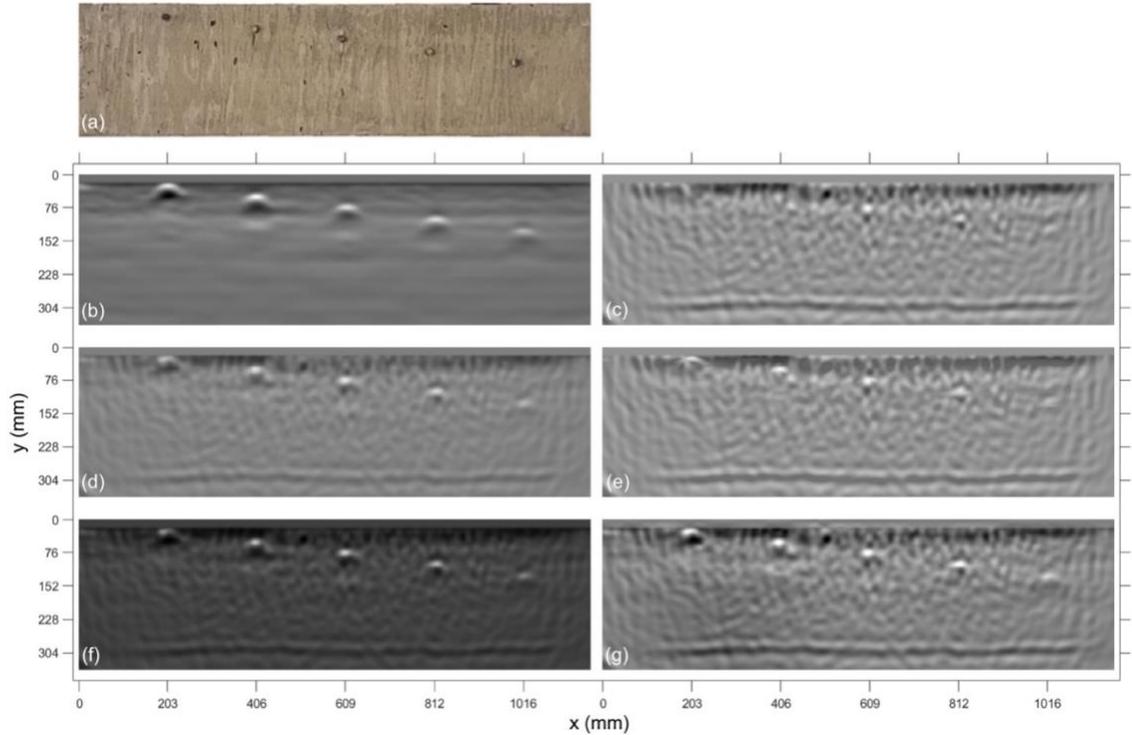
Figure 2-5. Results for Specimen 2: (a) Photo, reconstructed images from (b) GPR and (c) UEA, and fused images using (d) averaging, (e) maximum, (f) product, and (g) our proposed method.

Table 2-2. Normalized local evaluation metrics for select image features from Specimen 2.

Case	Position: x, y in (mm)	GPR	UEA	Average	Maximum	Product	Proposed method
#4 rebar	8, 1 (203, 25)	**1.00**	0.00	0.45	0.56	0.46	**1.01**
#4 rebar	16, 2 (406, 51)	**1.00**	0.52	0.75	0.79	0.87	**1.08**
#4 rebar	24, 3 (610, 76)	0.86	**1.00**	0.90	0.98	**1.12**	**1.23**
#4 rebar	32, 4 (813, 102)	**1.00**	0.83	0.85	0.82	**1.05**	**1.29**
#4 rebar	40, 5 (1016, 127)	**1.00**	0.83	0.83	0.82	**0.98**	1.23
Backwall	28.8, 12 (730, 305)	0.00	**1.00**	0.49	0.89	0.42	**1.05**

From Table 2-2 and Figure 2-5 we can observe that the GPR image [Figure 2-5 (b)] clearly

shows small rebars at different depths, while the UEA image [Figure 2-5 (c)] does not

reveal small and close-to-the-surface rebars. The results in the Table 2-2 are normalized with respect to the best individual modality to show if any of the fusion methods can retain or improve the evaluation metric. Average and maximum [Figure 2-5 (d) and (e)] do not perform better than any of the single modalities while product [Figure 2-5 (f)] sometimes gives better results, especially when both modalities detect the rebar. However, product fails when one modality does not detect it and when information is complementary. In the case of a backwall, the information is complementary and averaging and product perform worse than maximum. Our proposed method [Figure 2-5 (g)] can preserve and accentuate information in all the above cases.
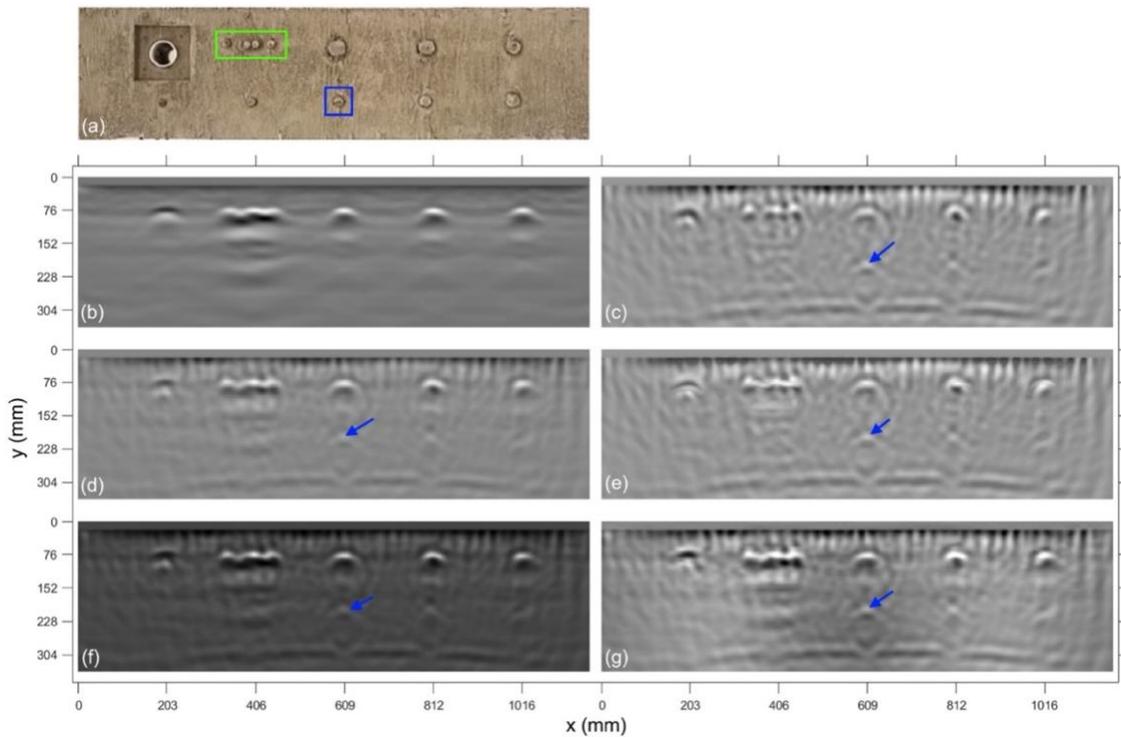
Figure 2-6. Results for Specimen 3: (a) Photo, reconstructed images from (b) GPR and (c) UEA, and fused images using (d) averaging, (e) maximum, (f) product, and (g) our proposed method.

36

Table 2-3. Normalized local evaluation metric for reconstructed images for Specimen 3.

Case	Position: x, y in (mm)	GPR	UEA	Average	Maximum	Product	Proposed method
#11 rebar	24, 3 (610, 76)	**1.00**	0.63	0.81	0.79	**1.08**	**1.03**
#10 rebar	32, 3 (813, 76)	**1.00**	0.76	0.80	0.89	**1.01**	**1.12**
# 9 rebar	40, 3 (1016, 76)	**1.00**	0.84	0.84	0.84	**1.09**	**1.36**
# 6 rebar	24, 8.5 (610, 216)	0.00	**1.00**	0.57	0.93	0.60	**1.09**
Backwall	28.8, 12 (730, 305)	0.12	**1.00**	0.54	0.87	0.52	**0.99**
Pipe	8, 3 (203, 76)	0.89	**1.00**	0.75	0.91	0.76	**1.46**
Close rebars	13.75-17.75, 3 (349-451, 76)	0.62	**1.00**	0.67	0.63	**1.14**	**1.19**

From Figure 2-6 And Table 2-3 we can see that both GPR and UEA images [Figure 2-6 (b) and (c)] clearly show the large diameter rebars that are located close to the surface. In this case, averaging, maximum, and product [Figure 2-6 (d) to (f)] are all able to detect the features as well, while product giving a better result, since the feature is detected in both modalities and multiplying them accentuates redundant information. The proposed method [Figure 2-6 (g)] can retain the information from both modalities and gives the best results. In case of the #6 rebar at a depth of 216 mm (8.5 in) that is hidden under the #11 top rebar [see blue box in Figure 2-6 (a)], as expected, the GPR image [Figure 2-6 (b)] does not show the rebar since all the energy is reflected back from the top rebar. However, the UEA image [Figure 2-6 (c)] reveals this feature (see blue arrow) because stress waves can propagate through metallic objects. In this case, averaging, maximum, and product [Figure 2-6 (d) to (f)] give worse results compared to when only a single modality, e.g., UEA, is used, hence no value is added with fusion. However, the proposed method [Figure 2-6 (g)] not only retains the information but also has a slightly improved contrast value. In the case of Type 2 reflectors, i.e., the pipe and the backwall, we can see that the GPR image [Figure 2-6 (b)]

barely shows the backwall. Again, none of the fusion methods give better results than the best individual modalities, which is UEA in this case, but the proposed method [Figure 2-6 (g)] retains the information of the backwall and intensifies the pipe. The fusion rule is to keep the minimum value when both modalities detect a dark feature or trust UEA when the UEA image shows a dark feature while the GPR image shows it in gray. For closely spaced rebars [see green box in Figure 2-6 (a)], we also study a horizontal line at $y = 76$ mm (3 in) and consider the relative contrast of the rebars as well as the relative contrast of the space between the rebars. We can see that the UEA image [Figure 2-6 (b)] is better than the GPR image [Figure 2-6 (c)], and among the fusion methods, product [Figure 2-6 (f)] and our proposed method [Figure 2-6 (g)] exhibit the best performance. It should be noted that none of the images allow for distinguishing the two middle bars, which are in contact with each other, i.e., all images show three rather than four individual reflectors. This is a limitation of our instruments and their resulting wavelength in our concrete.
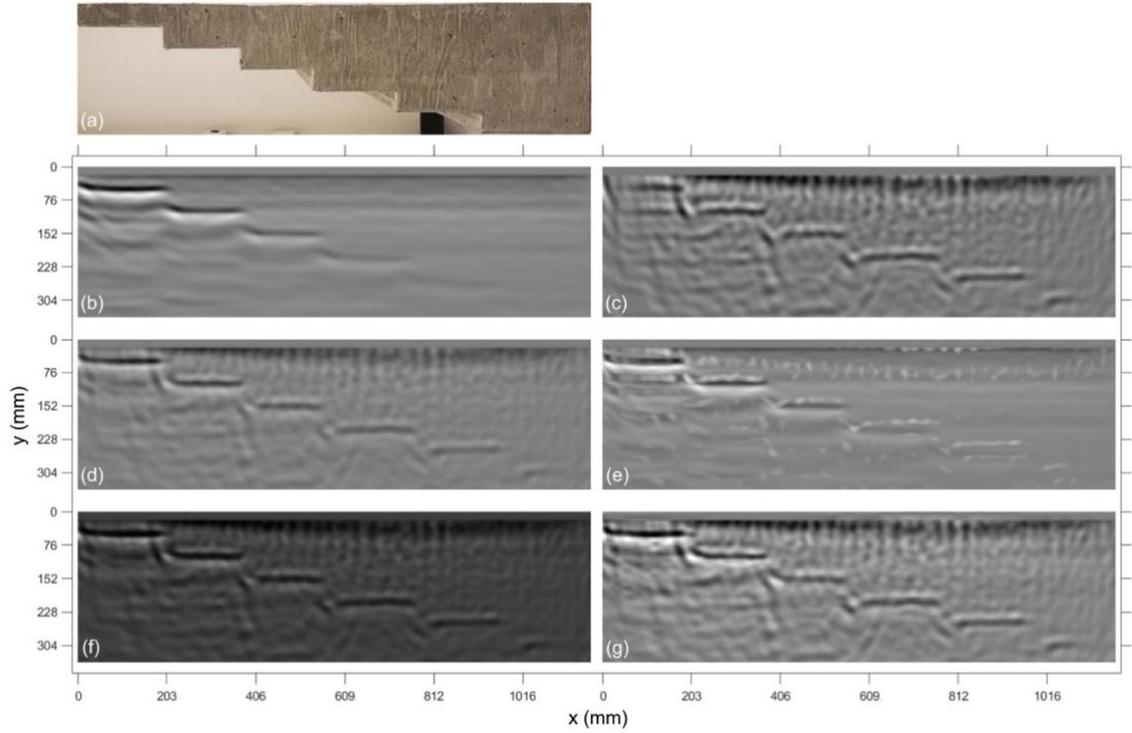
Figure 2-7 Results for Specimen 1: (a) Photo, reconstructed images for (b) GPR and (c) UEA, and fused images using (d) Averaging, (e) Maximum, (f) Product, and (g) our proposed method.

Table 2-4. Normalized local evaluation metric for images from Specimen 1.

Case	Position: x, y in (mm)	GPR	UEA	Average	Maximum	Product	Proposed method
Step 1	4, 2 (102, 51)	**1.00**	0.46	0.68	0.74	0.55	**1.08**
Step 2	11.5, 4 (292, 102)	0.84	**1.00**	0.88	**1.06**	0.82	**1.06**
Step 3	18.5, 6 (470, 152)	0.57	**1.00**	0.75	0.61	0.73	**0.97**
Step 4	26, 8 (660, 203)	0.38	**1.00**	0.66	0.57	0.65	**0.99**
Step 5	34, 10 (864, 254)	0.19	**1.00**	0.47	0.38	0.49	**1.01**
Step 6	43, 12 (1092, 305)	0.32	**1.00**	0.55	0.82	0.57	**0.98**

From Table 2-4 and Figure 2-7 we can see that the UEA image [Figure 2-7 (c)] shows the backwalls (steps) consistently better than the GPR image [Figure 2-7 (b)] except for the one very close to the surface. The proposed method [Figure 2-7 (g)] can retain and improve the information in most of the cases better than any of the other methods [Figure 2-7 (d) to (f)].

2.6.2. Global Evaluation Metrics

While we have now evaluated image quality based on local metrics, it can be valuable to consider some global evaluation metrics. Although we humans usually pay attention to local features and salient points in the image, we care about the overall appearance of the image as well. In addition, we would like to determine the overall information content of an image as well. These global metrics of quality are important for future work on automating the pipeline since image analysis methods such as deep neural networks perform notably worse when input images have a low quality [36]. In this study we used standard deviation, entropy, and average gradient as global evaluation metrics.

The standard deviation of a gray-level image represents the overall contrast. Usually, higher contrast images are more favorable for human perception because the features are more clearly discernible from the background [37]. Table 2-5 shows the results for the standard deviation metric of all reconstructed images for all three specimens. Values were computed for the entire images shown in Figure 2-5 to Figure 2-7 and then normalized relative to the highest individual modality. The fused image with the proposed method has a higher contrast compared to all other images.

Image entropy is used to measure the information content and richness of a grayscale image [37, 38]. Table 2-5 shows the results for the entropy metric. The values are normalized relative to the highest individual modality. The proposed wavelet-based method produces an image with the highest information entropy among all images, which supports a visual analysis of the image where we can observe more details of rebars and backwall information.

Average gradient is an image fusion metric where spatial resolution of an image can be compared to other images [32]. Each pixel of the gradient image shows how the intensity changes in a given direction. We expect a higher average gradient for an image with more edges and features. Table 2-5 shows the results of the average gradient metric for the different images. The values are normalized relative to the highest individual modality. It can be observed that the proposed wavelet-fused image has a higher average gradient, which means they contain more discernible features. This is consistent with a visual analysis, especially for the case of the proposed wavelet-based image where we can perceive more discernible features.

We can see that the proposed method performs well for all three global metrics and for all specimens. While maximum was not the best method when evaluated locally, it gives high global information, which makes sense since it maximizes information. However, it is unable to perform well globally for Specimen 1 when we have only Type 2 reflectors. This is because maximizing is not desired when the extremes are local minima. Even though product gives a high result in some cases, it does not perform well globally. Averaging, as expected by its definition, averages the information. We can see that the proposed method is able to retain the information from both modalities and accentuates them.

Table 2-5. Normalized global evaluation metrics for images of all specimens.

Specimen	Global Metric	GPR	UEA	Average	Maximum	Product	Proposed method
1	Standard Deviation	0.80	**1.00**	0.72	0.74	0.68	**1.21**
2	Standard Deviation	0.70	**1.00**	0.68	0.91	0.65	**1.16**
3	Standard Deviation	0.82	**1.00**	0.77	**0.95**	0.77	**1.34**
1	Entropy	0.91	**1.00**	0.91	0.91	0.91	**1.05**
2	Entropy	0.88	**1.00**	0.89	**0.99**	0.88	**1.05**
3	Entropy	0.92	**1.00**	0.91	**1.00**	0.92	**1.12**
1	Average Gradient	0.60	**1.00**	0.62	0.67	0.62	**1.17**
2	Average Gradient	0.50	**1.00**	0.57	**0.96**	0.54	**1.12**
3	Average Gradient	0.64	**1.00**	0.67	**0.97**	0.67	**1.18**

2.7. Summary and Conclusions

In this article, a pipeline to image the interior of concrete structures is proposed and evaluated. Three laboratory concrete specimens with known geometry, material properties, and features were employed to evaluate the entire methodology. Data were collected for two different modalities using two commonly used non-destructive testing (NDT)

instruments, namely ground penetrating radar (GPR) and ultrasonic echo array (UEA). An extended total focusing method (XTFM) was developed to reconstruct 2D images for both measurement modalities. A novel fusion algorithm based on multilevel wavelet decomposition and an NDT-informed rule was developed to fuse the GPR and UEA images. Image quality metrics were utilized enabling a quantitative comparison of the fused images in terms of local feature contrast and overall global quality. The results show that advanced image fusion has significant potential to enhance concrete imaging compared to when only individual GPR or UEA images are used. We made the following observations:

1. For the close-to-surface Type 1 reflectors (e.g., rebars) as well as small Type 1 reflectors, GPR is the superior modality, while UEA gives decent results except for small rebars close to the surface.

2. For Type 2 reflectors (e.g., pipe, backwall) UEA performs better than GPR, while GPR gives decent results, especially if the reflector is not very far from the surface.

3. If a metallic reflector is blocked by another metallic reflector, GPR is not able to detect it while UEA can.

4. For closely spaced rebars, UEA is performing better than GPR in differentiating the intensity in the space between rebars as well as keeping a high relative amplitude for the reflector.

5. The averaging fusion method keeps the information from both modalities, while smoothing everything. The maximum method does not produce consistent results and usually fails to improve an image. The reason is that the signals have multiple oscillations and there is usually a mismatch in many portions of the signals. Also, in case of Type 2 reflectors, maximization is not desired. The product method

43

sometimes gives promising results, in particular for the cases when both modalities detect a Type 1 reflector. However, it fails in almost all other cases such as when the information is complementary (i.e., one modality detects a feature and the other one does not), and when the reflector is Type 2.

6. The proposed wavelet method takes advantage of low pass filtering the images first to smooth the images and minimize undesired non-feature extrema (oscillations) and then apply a custom fusion rule, that maximizes, minimizes and averages pixel values depending on the type of reflector. In addition, high pass filtering images and maximizing details improves amplitude and relative contrast. This method has shown promise in all the cases covered in this study.

In conclusion, the proposed pipeline produced enhanced 2D images that retain and accentuate the information from both modalities with a target of Type 1 and Type 2 reflectors for all three specimens. We see significant potential and opportunity for further research, taking full advantage of the latest advances in the fields of image fusion and machine learning. The next step will be to collect additional data from specimens with known defects such as different types of cracking, rebar corrosion, and other forms of degradation. The fusion algorithm will also be tested and evaluated on large-scale laboratory specimens that exhibit different levels of damage from loading. Our ultimate goal is to develop a practical diagnostic tool that can be used to automatically analyze images and assist an inspector in the condition assessment of concrete structures.

Sharing of the Data and Algorithms

All data and algorithms presented in this article will be available on the following GitHub repository [31]: https://github.com/Sinamhd9/A-Pipeline-for-Enhanced-Multimodal-Imaging-of-Structural-Concrete.

Acknowledgments

Compliance with Ethical Standards

2.8. References

[1]   Clem, D. J., Schumacher, T., & Deshon, J. P. (2015). A consistent approach for processing and interpretation of data from concrete bridge members collected with a hand-held GPR device. *Construction and Building Materials*, 86, 140-148.

[2]   Sun, H., Pashoutani, S., & Zhu, J. (2018). Nondestructive evaluation of concrete bridge decks with automated acoustic scanning system and ground penetrating radar. *Sensors*, 18(6), 1955.

[3]   Lai, W. W. L., Derobert, X., & Annan, P. (2018). A review of Ground Penetrating Radar application in civil engineering: A 30-year journey from Locating and Testing to Imaging and Diagnosis. *NDT & E International*, 96, 58-78.

[4]   Schickert, M., Krause, M., & Müller, W. (2003). Ultrasonic imaging of concrete elements using reconstruction by synthetic aperture focusing technique. *Journal of Materials in Civil Engineering*, 15(3), 235-246.

[5]   Krause, M., Mielentz, F., Milman, B., Müller, W., Schmitz, V., & Wiggenhauser, H. (2001). Ultrasonic imaging of concrete members using an array system. *NDT & E International*, 34(6), 403-408.

[6]   Bittner, J. A., Spalvier, A., & Popovics, J. S. (2018). Internal Imaging of Concrete Elements. *Concrete International*, 40(4), 57-63.

[7]   Choi, H., & Popovics, J. S. (2015). NDE application of ultrasonic tomography to a full-scale concrete structure. IEEE transactions on ultrasonics, ferroelectrics, and frequency control, 62(6), 1076-1085.

[8]   Choi, H., Bittner, J., & Popovics, J. S. (2016). Comparison of ultrasonic imaging techniques for full-scale reinforced concrete. *Transportation Research Record,* 2592(1), 126-135.

[9]   Balázs, G. L., Lublóy, É., & Földes, T. (2018). Evaluation of concrete elements with X-ray computed tomography. *Journal of Materials in Civil Engineering*, 30(9), 06018010.

[10]   Moosavi, R., Grunwald, M., & Redmer, B. (2020). Crack detection in reinforced concrete. *NDT & E International*, 109, 102190.

[11]   Marfisi, E., Burgoyne, C. J., Amin, M. H. G., & Hall, L. D. (2005). The use of MRI to observe the structure of concrete. *Magazine of concrete research*, 57(2), 101-109.

[12]   Pla-Rucki, G.F. and Eberhard, M.O., (1995) "Imaging of reinforced concrete: State-of-the-art review." *Journal of Infrastructure Systems*, Vol. 1(2)*,* pp: 134-141.

[13]   Büyüköztürk, O., (1998). "Imaging of concrete structures." *NDT & E International*, Vol. 31(4), pp: 233-243.

[14]   ACI-American Concrete Institute. (2013). 228: 2R-13 Report on nondestructive test methods for evaluation of concrete in structures.

[15]   Kohl, C., Krause, M., Maierhofer, C. and Wöstmann, J., (2005). "2D-and 3D-visualisation of NDT-data using data fusion technique." *Materials and Structures*, Vol. 38(9), pp: 817-826.

[16]   Langenberg, K.J., Mayer, K. and Marklein, R., (2006). "Nondestructive testing of concrete with electromagnetic and elastic waves: Modeling and imaging." *Cement and Concrete Composites*, Vol. 28(4), pp: 370-383.

[17]   Li, H., Manjunath, B.S. and Mitra, S.K., (1995). "Multisensor image fusion using the wavelet transform." *Graphical models and image processing*, Vol. 57(3), pp: 235-245.

[18]   Nikolov, S., Hill, P., Bull, D. and Canagarajah, N., (2001). "Wavelets for image fusion." *Wavelets in signal and image analysis* pp: 213-241. Springer, Dordrecht.

[19]   Maierhofer, C., Zacher, G., Kohl, C., & Wöstmann, J. (2008). Evaluation of radar and complementary echo methods for NDT of concrete elements. *Journal of Nondestructive Evaluation*, 27(1-3), 47.

[20]   Van der Wielen, A., Lybaert, M. and Grégoire, C., (2017). "Combined GPR and ultrasonic tomography measurements for the evaluation of a new concrete pavement." *Proc. 9th International Workshop on Advanced Ground Penetrating Radar (IWAGPR),* IEEE, pp: 1-6.

[21]   Krause, M., Bärmann, M., Frielinghaus, R., Kretzschmar, F., Kroggel, O., Langenberg, K.J., Maierhofer, C., Müller, W., Neisecke, J., Schickert, M. and Schmitz, V., (1997). Comparison of pulse-echo methods for testing concrete. *NDT & E International*, Vol. 30(4), pp: 195-204.

[22]   Gucunski, N., & National Research Council. (2013). *Nondestructive testing to identify concrete bridge deck deterioration*. Transportation Research Board.

[23] Wimsatt, A., White, J., Leung, C., Scullion, T., Hurlebaus, S., Zollinger, D., ... & Tonon, F. (2014). *Mapping voids, debonding, delaminations, moisture, and other defects behind or within tunnel linings* (No. SHRP 2 Report S2-R06G-RR-1).

[24] Salazar, A., Gosalbez, J., Safont, G. and Vergara, L., (2012). "Data fusion of ultrasound and GPR signals for analysis of historic walls". *IOP Conference Series: Materials Science and Engineering*, IOP Publishing, Vol. 42(1), p: 012008.

[25] Völker, C., & Shokouhi, P. (2015). Multi sensor data fusion approach for automatic honeycomb detection in concrete. *NDT & E International*, 71, 54-60.

[26] Völker, C., & Shokouhi, P. (2015). Clustering based multi sensor data fusion for honeycomb detection in concrete. *Journal of Nondestructive Evaluation*, 34(4), 32.

[27] Zhang, J., Drinkwater, B.W., Wilcox, P.D. and Hunter, A.J., (2010). "Defect detection using ultrasonic arrays: The multi-mode total focusing method." *NDT & e International*, Vol. 43(2), pp: 123-133.

[28] Holmes, C., Drinkwater, B.W. and Wilcox, P.D., (2005). "Post-processing of the full matrix of ultrasonic transmit–receive array data for non-destructive evaluation." *NDT & E International*, Vol. 38(8), pp: 701-711.

[29] Carcreff, E., Laroche, N., Braconnier, D., Duclos, A., & Bourguignon, S. (2017, September). Improvement of the total focusing method using an inverse problem approach. In *2017 IEEE international ultrasonics symposium (IUS)* (pp. 1-4). IEEE.

[30] Kerr, W., Rowe, P., & Pierce, S. G. (2017). Accurate 3D reconstruction of bony surfaces using ultrasonic synthetic aperture techniques for robotic knee arthroplasty. *Computerized Medical Imaging and Graphics*, 58, 23-32.

[31]   Mehdinia, S. (2021). GitHub Repository: https://github.com/Sinamhd9/A-Pipeline-for-Enhanced-Multimodal-Imaging-of-Structural-Concrete.

[32]   Daneshvar, S. and Ghassemian, H. (2010). "MRI and PET image fusion by combining IHS and retina-inspired models." *Information Fusion*, Vol. 11(2), pp.114-123.

[33]   Pajares, G., & De La Cruz, J. M. (2004). A wavelet-based image fusion tutorial. *Pattern recognition*, 37(9), 1855-1872.

[34]   Balakrishnan, S., Cacciola, M., Udpa, L., Rao, B. P., Jayakumar, T., & Raj, B. (2012). Development of image fusion methodology using discrete wavelet transform for eddy current images. *NDT & E International*, 51, 51-57.

[35]   Wang, A., Sun, H., & Guan, Y. (2006, April). The application of wavelet transform to multi-modality medical image fusion. In *2006 IEEE International Conference on Networking, Sensing and Control* (pp. 270-274). IEEE.

[36]   Dodge, S., & Karam, L. (2017, July). A study and comparison of human and deep learning recognition performance under visual distortions. In 2017 26th international conference on computer communication and networks (ICCCN) (pp. 1-7). IEEE.

[37]   Jagalingam, P., & Hegde, A. V. (2015). A review of quality metrics for fused image. *Aquatic Procedia*, 4(Icwrcoe), 133-142.

[38]   Gonzalez, R.C. and Woods, R.E., (2008). "Digital image processing:" Pearson prentice hall. *Upper Saddle River, NJ*, 1.

3. Chapter Three: Damage Tracking of Full-scale Pre-1990s Reinforced Concrete Bridge Members During Reverse Cyclic Loading Using Fusion-based Imaging

Sina Mehdinia[1], Thomas Schumacher[2], AKM Golum Murtuz[3], and Peter Dusicka[4]

This article will be submitted to Journal of Nondestructive Evaluation.

[1]PhD Candidate, Department of Civil and Environmental Engineering, Portland State University, Portland, OR, USA, E-mail: mehdinia@pdx.edu

[2]PhD, PE, Associate Professor, Department of Civil and Environmental Engineering, Portland State University, Portland, OR, USA, E-mail: thomas.schumacher@pdx.edu

[3]PhD, Department of Civil and Environmental Engineering, Portland State University, Portland, OR, USA, E-mail: amurtuz@pdx.edu

[4] PhD, Professor, Department of Civil and Environmental Engineering, Portland State University, Portland, OR, USA, E-mail: dusicka@pdx.edu

Abstract

Fusion-based imaging using ground penetrating radar (GPR) and ultrasonic echo array (UEA) measurements is used to track damage progression of two full-scale reinforced concrete (RC) bridge column-footing subassembly specimens with different lap-splice detailing. The laboratory specimens were subjected to reverse-cyclic lateral loading following the Cascadia Subduction Zone (CSZ) loading protocol. Two vertical GPR and UEA scans were performed on each of the columns' east and west faces at select ductility levels. Images from the interior of the columns were reconstructed using the pipeline developed in Chapter Two, the extended total focusing method (XTFM), and a wavelet-based fusion technique. Finally, the images from the two sides were fused together to create two composite images of the interior of each column. A qualitative analysis based on the structural similarity (SSIM) index of the reconstructed images was found to capture damage progression well. A so-called backwall analysis is also presented, in which the amplitude of the backwall reflector was used to track damage progression. This quantitative analysis shows that changes in the images can be detected as early as the first measurement, which in this study was at a ductility level, $\mu = 0.5$. Moreover, the changes along the height of the column vary, and are consistent with the higher damage at the bottom of the column. Finally, a comparison between the two columns is presented. In conclusion, fusion-based imaging can be used to track and characterize damage progression in full-scale RC members adequately.

ultrasonic echo array; ground penetrating radar; extended total focusing method; image fusion.

3.1. Introduction

The evaluation of reinforced concrete (RC) structures after an extreme event is usually done by visual inspection of the outer surface [1], monitoring the debonding of steel reinforcing (rebars), and crushing damage of the concrete [2]. Earthquakes can cause damage to a structure that is not visible on the surface. Internal cracking can affect the overall health of the structure, its remaining life, as well as its serviceability. Non-destructive testing methods (NDT) can be helpful in evaluating the condition of the structure after an earthquake, employing array-based approaches, advanced imaging, and advanced data analysis techniques [3, 4 , 5, 6, 7, 8, 9]. A large number of bridges in Oregon were built before the 1990s, prior to the development of the current seismic design code [10]. As a result, the design and detailing of these bridges focuses only on the gravity load system with minimal consideration to a lateral load path. This, coupled with the increase in seismic demand due to the CSZ earthquake event, has led to the renewed interest in gathering experimental data for these potentially vulnerable bridges.

Ultrasonic (US) testing has been shown to be promising for evaluating the health of a structure after an extreme event. Polimeno et al. [11] showed that there is a correlation between US velocity and drift ratios when they tested a two-story RC frame on a shake test with incremental seismic loading. They showed that there is a significant difference in the p-wave velocity between the bottom and mid-height of the column. The velocities at the mid-height of the column were found to be higher and more uniform in comparison with

the bottom of the column. The reduction in velocity and local variability at the bottom of the column indicated the presence of damage. The researchers concluded that the cracks orthogonal to the direction of measurement can be detected with US tests. Choi et al. [2] performed 2D US tomography on a full-scale RC column at increasing deformation levels up to a drift ratio of 1% and stacked the tomograms in a 3D format. Their work showed that US tomograms are able to track damage progression that are in line with strain gauge data. Using this method, they also showed that ultra-high-performance fiber-reinforced concrete (UHPFRC) columns have less damage than conventional RC columns. Choi et al. [12] also showed that US tomography (through thickness measurements), compared to one-sided echo imaging, has the benefits of having better performance when a highly dense layer of reinforcement is present. Freeseman et al. [13] exposed a full-scale RC column to simulated earthquake loading and performed US echo imaging. They collected data at three stages, i.e., the baseline (= 0% drift), 0.5% drift, and 1%. They used the extended synthetic aperture focusing technique (SAFT) [14] to reconstruct the images and showed that changes in the relative reflectivity of the reconstructed US images are indicative of damage, before surface damages were visible. They also used Pearson's correlation method to quantify damage levels, which is an indicator of linear dependence of an image with the baseline.

The work presented in this article is based on our previously developed fusion imaging pipeline presented in Chapter two and herein used to evaluate the condition of two full-scale RC column-footing subassembly specimens subjected to reverse-cyclic loading and makes the following contributions:

1. Two NDT techniques, namely GPR and UEA, were used for image fusion and comparison purposes. We confirm previous findings in the literature that US measurements can reveal internal changes at early stages of damage and show the limitations of GPR to detect such changes. We applied our previously established image reconstruction and fusion pipeline to realistic full-scale RC members experiencing increasing levels of demand to produce high quality images that provide all information in one frame.

2. Two specimens were tested to increase the reliability of the results and verify repeatability. A structural performance comparison is made between the two specimens showing that our method can detect the difference in the specimen's behavior.

3. Measurements were collected at seven different stages of loading corresponding to increasing ductility levels, μ. This provides a better picture of our method's ability to capture the performance of the specimens.

4. The structural similarity (SSIM) index from the field of image processing is introduced and found useful in quantifying and distinguishing internal changes (a) between different levels of damage as well as (b) along the height of the column.

5. A quantitative backwall analysis and visualization is presented that measures the changes of the average backwall amplitudes compared to the baseline, for the bottom, middle and top sections of the columns.

3.2. Experimental setup

3.2.1. Test specimens

Two full-scale reinforced concrete (RC) specimens representative of pre-1990s bridge column-footing subassemblies were constructed and tested in the iSTAR Laboratory at Portland State University. A cantilever 610 x 610 mm square cross-section RC column with four 25 mm-diameter continuous longitudinal steel reinforcing bars (rebars) was used for Specimen 1 whereas Specimen 2 had a lap splice located in the plastic hinge zone (see Figure 3-1). The lap splice length for the dowel bars starting from the column-footing joint was $25d_b$ (or 635 mm). The transverse reinforcement consisted of 10 mm-diameter square ties with 90-degree hooks at both ends with an extension of 10 times the diameter of the tie bars (or 114 mm). The concrete clear cover from the external face of the tie bars to the face of the column cross section was 25 mm for both of the specimens. The first tie at the bottom of the column region is located 152 mm from the column-footing joint, with subsequent ties spaced at 305 mm. A square spread footing with a single orthogonal layer of 16 mm-diameter rebars spaced at 165 mm located at the bottom was used as the foundation supporting the square column.
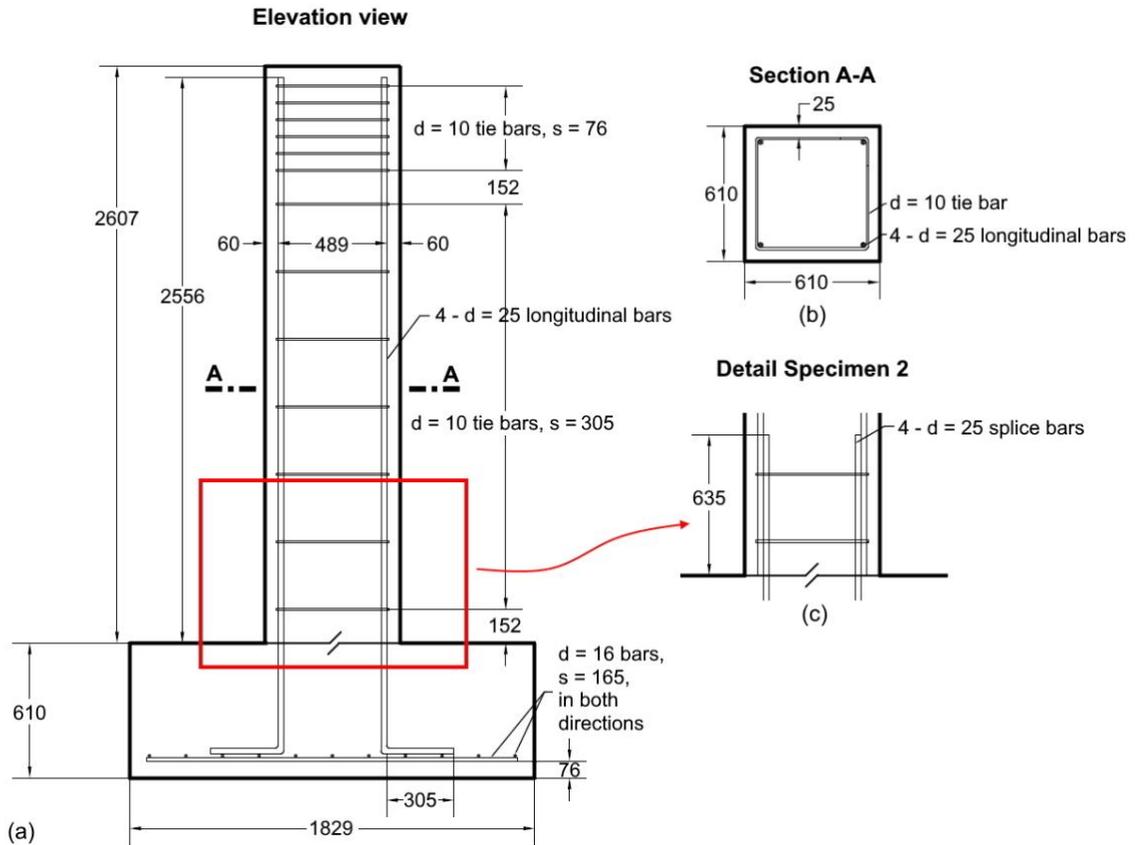
Elevation view

Figure 3-1. Drawings of RC column-footing subassembly test specimens: (a) Elevation view (Specimen 1 and 2), (b) Cross section (Specimen 1 and 2), and (c) lap splice detail Specimen 2. All dimensions in (mm).

3.2.2. Loading protocol

A reverse-cyclic protocol developed to capture the number and amplitude of cycles expected from a subduction earthquake [15] was utilized to assess the seismic performance of the reinforced concrete (RC) column-footing subassembly test specimens. This lateral loading protocol is characterized by higher number of cycles at the low ductility levels and lower number of cycles at the higher ductility level. The loading consists of two stages where the first stage includes three nominally elastic cycles, each having displacements,

57

$x(t)$ corresponding to $0.25\delta_i$, $0.5\delta_i$, and $0.75\delta_i$, followed by one cycle at $1.0\delta_i$ to capture initial damage such as first cracking and the progression of cracks. Here, δ_i is the analytically predicted yield lateral displacement as obtained from monotonic moment curvature analysis of the column cross-section. The second stage of the protocol consists of inelastic displacement cycles corresponding to increasing levels of ductility. The subduction protocol targeted a displacement ductility of $\mu = 8$ and a fundamental natural vibration period, $T = 0.5$ s, which was found to be representative of typical multi-column RC bridge columns [16]. The subduction zone lateral loading protocol is presented in Figure 3-2 (a). The variation of the gravity loads on the bridge columns due the secondary effects during ground shaking were simulated with a varying axial loading protocol (See Figure 3-2 (b)) that is proportional to the lateral strength of the column. A base axial compression load, $P_y = 890$ kN was initially applied and the variation in the axial column load was then implemented simultaneously alongside the application of lateral loading protocol.
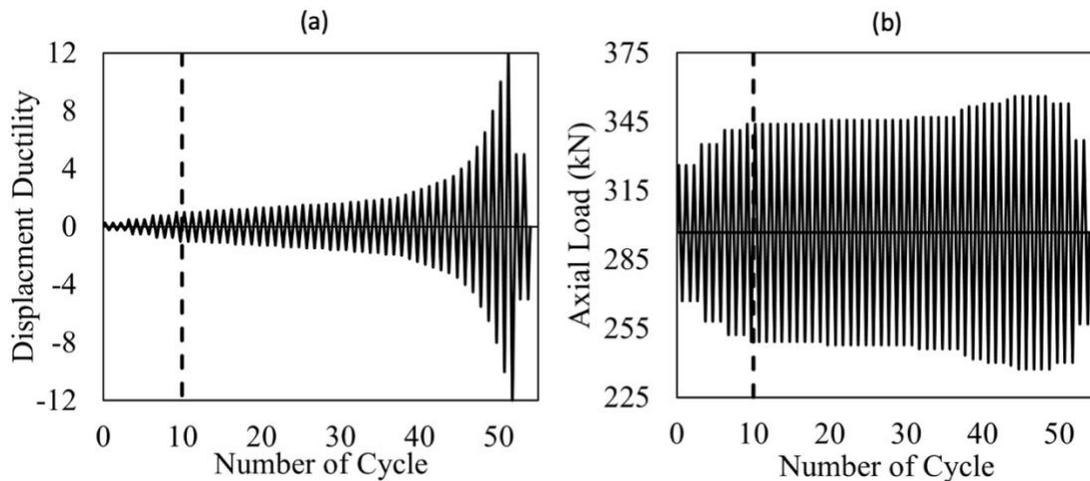
Figure 3-2. The subduction zone lateral (a) and (b) axial loading protocol

3.2.3. Specimen instrumentation

Several displacement transducers and strain gauges were used to monitor the global and local response of the test specimens. The lateral displacement imposed by the lateral actuator was captured using a load cell and LVDT attached to the actuator. The top displacement of the columns, $x(t)$ was measured with a string potentiometer attached to a fixed reference frame. Strain gauges were used to measure strain in both the longitudinal and dowel bars at critical locations. In addition, three strain gauges were placed at the transverse reinforcement to measure the strain of the tie bars. Strain gauges along the base of the column were closely spaced to have accurate spatial resolution in the plastic hinge zone. Two of the dowel strain gauges in each rebar were placed in the footing region to capture the strain penetration profile within the footing. Further details of the instrumentation can be found in [10].

3.2.4. Non-destructive measurements

An ultrasonic echo array (UEA) instrument with a central pulse frequency of 50 kHz and a temporal resolution, $\Delta t = 1\ \mu s$ from Proceq, Model Pundit 250 Array, was used to collect data. The instrument has an 8 x 3 array of transducers that fires an ultrasonic (US) shear wave pulse row-by-row into the material. The response is recorded with the other transducers. The resulting stress wave travels through the material and is reflected back when it reaches a boundary between materials with different acoustic impedances [17]. A hand-held ground penetrating radar (GPR) was used to collect data along the same scan

lines as US data were collected. The instrument used was a GSSI, Model StructureScan Mini XT with a central pulse frequency of 2.7 GHz. In GPR, electromagnetic waves are transmitted into a material and are reflected back when they reach boundaries between materials with different dielectric properties [8].

Figure 3-3 shows the locations of the four scan lines on the columns. The measurements were taken roughly from the base of the column but the image reconstruction was started at exactly the base of the column, i.e., at $y = 0.00$. The measurements were taken when the column was in a neutral position, i.e., at $x = 0$, at select ductility levels, μ. The seven-stage measurements for the columns were taken for the baseline, i.e., prior to starting the experiment, and increasing cycle numbers corresponding to roughly every 0.5 increase in ductility level, μ.
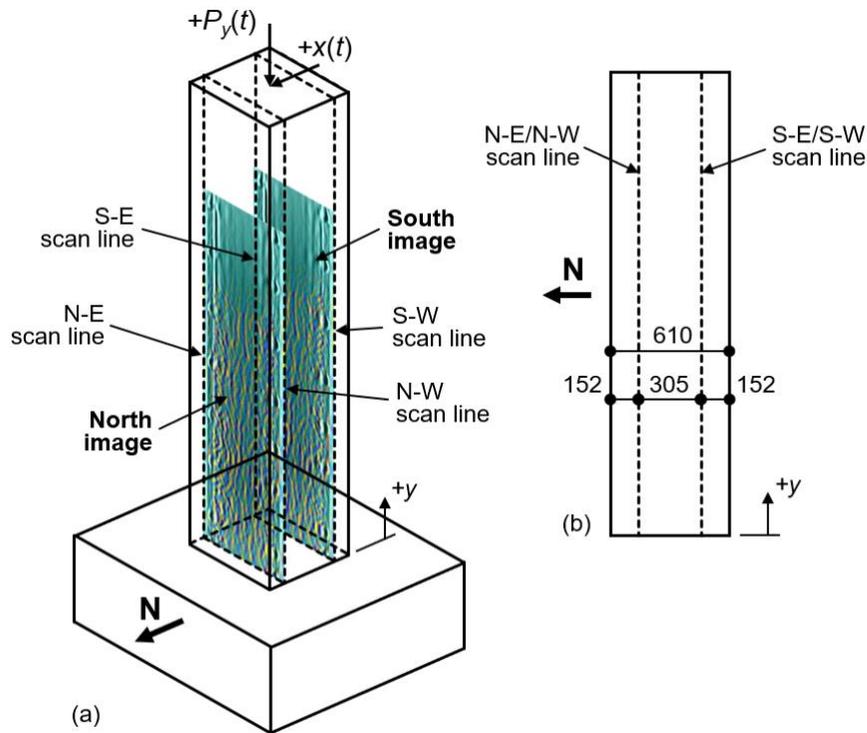
Figure 3-3. Illustrations of test specimen showing scan lines and sample final images: (a) Isometric view from north-east and (b) elevation view of column west face. N = north, S = south, E = east, and W = west. All dimensions in (mm).

3.3. Analytical methodology

We used the extended total focusing method (XTFM) (Chapter Two) to reconstruct the images from both GPR and UEA measurements. For UEA, in order to focus on the backwall and horizontal cracks, we discarded the areas that are not directly beneath the instrument. This is similar to a panoramic SAFT image that considers all the regions covered directly under the instrument and from all the sending and receiving channels. Panoramic SAFT images are stitched and averaged or maxed such as in extended SAFT

[14] in overlapping regions to generate a panoramic image, while XTFM sees the whole specimen as one entire region.

To have a complete picture of the interior of the specimens, we used image fusion to include all the information in one frame to achieve a comprehensive visualization [18]. In order to provide an even more complete picture of the columns' interior, two-sided fusion was implemented to include the information of the west and east images in one frame. Fusion allows taking advantage of the strengths of individual measurements. While GPR is an excellent tool to detect the rebars, US is better at detecting concrete air interfaces, such as a backwall and cracks or the changes in relative reflectivity [13] caused by damage. High reflectivity is an indicator of change in acoustic impedance. Therefore, the information is complementary in nature and can benefit from image fusion. The algorithm used for fusion is based on a wavelet decomposition [19] where GPR features are shown in gray and ultrasound features are shown in color. Our previously established pipeline for image reconstruction and fusion is used for this process [9].

Before fusion, standard surface wave removal was applied to both images, and proper normalization and translation was applied to make sure the images are in the same pixel range and are aligned horizontally. GPR and UEA from the north and south slices were individually obtained using fusion from the west and east slices. UEA two-sided fused image was colorized using the the parula colormap from MATLAB [20]. The coloring helps us quantifying the contribution of each modality in the final fused image. The two-sided GPR and UEA images were then fused together to create a final multimodal fused image. The fusion for both steps are the same. Each image was decomposed into an

approximation coefficient (low pass) and three high detail coefficients (high pass) using a

2D wavelet transform in a recursive fashion for four times [9]. The approximations were

averaged, and the details maxed. Multi-level wavelet reconstruction was used to obtain the

final fused image. Figure 3-4 illustrates the image reconstruction and fusion methodology.

It can be observed that the GPR and UEA measurements were not available over the same

height, which shows in the loss of scatter information from UEA visible in the top region

of the image. For consistency, only the region up to $y = 1.52$ m was included in our analysis

(see Figure 3-6 for details).
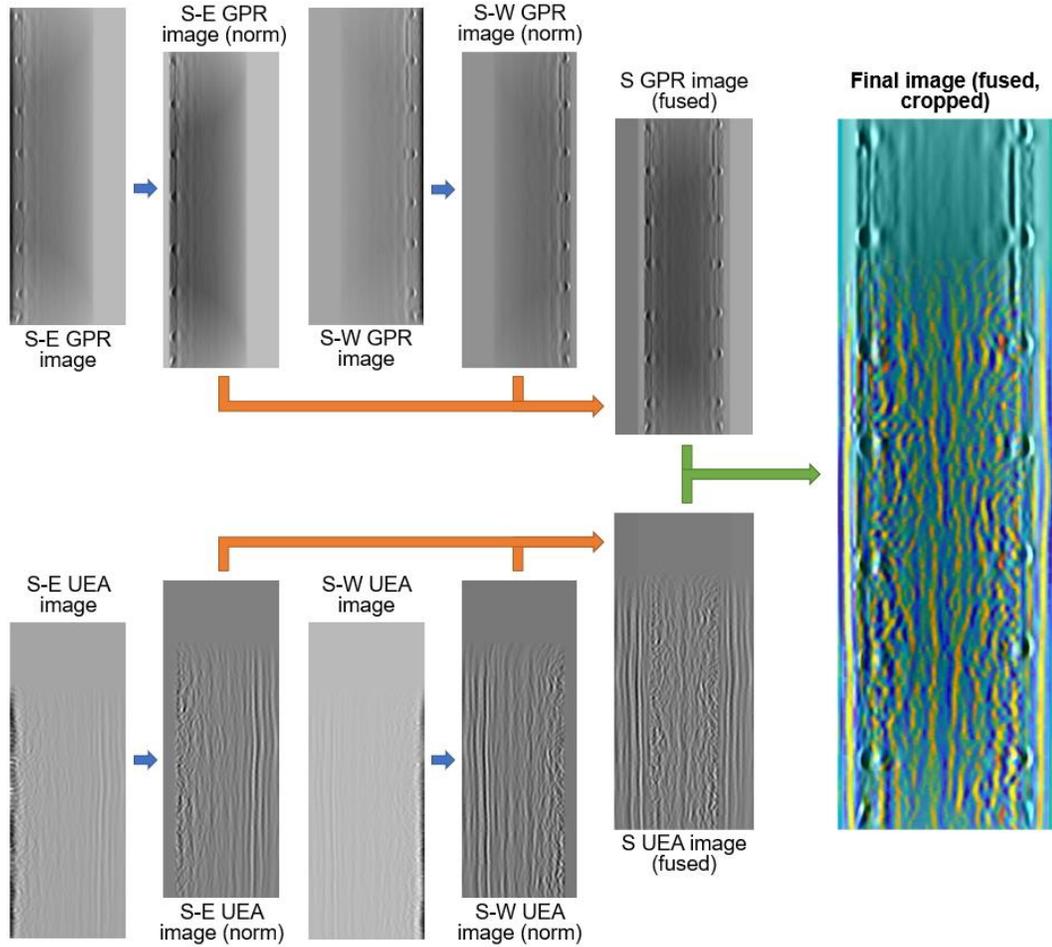
Figure 3-4. Illustration of image reconstruction and fusion methodology. N = north, S = south, E = east, and W = west.

3.4. Results and discussion

3.4.1. Structural performance

Figure 3-5 shows the lateral load vs. drift ratio hysteresis loops of the two specimens tested. The load-deformation response of Specimen 1 is characterized by a stable hysteretic response with wide loops at higher displacement ductility cycles [Figure 3-5 (a)]. The peak lateral load recorded in the push direction was 198 kN and the corresponding lateral

displacement was 47 mm. In the pull direction, the measured peak load was 169 kN and the displacement was 32 mm. The sequence of damage for Specimen 1 was concrete cracking, yielding of longitudinal reinforcement, initiation of cover spalling, loss of cover concrete, and buckling of longitudinal reinforcement. The ultimate displacement capacity of Specimen 1 was 108 mm in the push direction and 139 mm in the pull direction. The corresponding drift ratio at the ultimate displacement capacity was calculated as 4.1% and 5.3%, respectively, for the push and pull directions.

Specimen 2 contains short lap splices within the plastic hinge zone that resulted in lap splice failure. As a result, the load-deformation response of Specimen 2 shows rapid strength degradation in the pull cycle [see Figure 3-5(b)]. The hysteretic loops for this specimen were closely spaced compared to Specimen 1, indicating lower energy dissipation. The peak lateral load measured in the push and pull directions were 186 kN and 164 kN, respectively. The lateral displacement corresponding to the peak load was 42 mm for both the push and pull directions. Following the peak load, significant strength reduction led to a poor performance of this specimen compared to Specimen 1. The ultimate displacement capacity was 52 mm in the pull direction while in the push direction, the specimen continued to sustain the lateral load carrying capacity. The drift ratio associated with the ultimate displacement capacity was calculated to be 2.0%, which is significantly lower than Specimen 1.
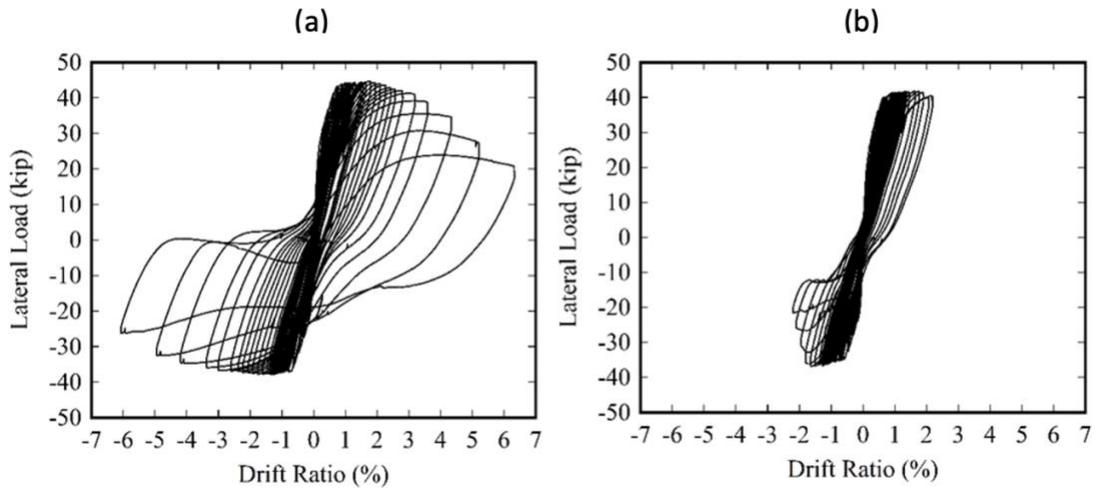
Figure 3-5. Load-drift response of the tested specimens, (a) Specimen 1, and (b) Specimen 2

3.4.2. Qualitative observations

Figure 3-6 shows sample qualitative fused images from the south side of Column 1 for the baseline and a ductility level, $\mu = 2.0$. The images for all seven stages of loading starting from baseline (prior to loading) to failure are provided in the Appendix Figure 3-13 through Figure 3-16. It can be seen that the relative reflections are dispersing and gaining higher amplitudes while the specimen is experiencing cracking. As can be seen in Figure 3-6, UEA images are capable of revealing the backwall, as well as reflections from internal cracking and reinforcements [13]. Moreover, the backwall portion of the images, which is clear in all baseline states, starts to be shadowed by degradation as we increase the loading. Indeed, the backwalls are clearly visible in the baseline (damage free) state, and as we progress with loading and damage, the backwall reflection starts to show gaps and a loss in amplitude. This suggests that the cracks are scattering and blocking the waves from

reaching and returning from the backwall. It is also interesting to note that changes in the backwall of the low region (i.e., Section 1) are more severe compared to the middle (i.e., Section 2) and especially the top regions (i.e., Section 3) as delineated by black dashed lines shown in Figure 3-6. This implies that the bottom regions of the columns experience a higher level of damage. This can be explained by the distribution of the internal forces, namely the bending moment, as is illustrated in Figure 3-7 (d). In practice, the lower portions of the columns are subjected to high rotational demands and axial loads, and damage to the ground level columns of a building can cause a total collapse [2]. The lower regions of the columns carry a higher bending moment and are thus expected to show more damage. This is also shown in Figure 3-7 (e) where we see more cracks at the lower sections of the column. Figure 3-7 illustrates the applied and internal forces in the column and a sample visual crack map of one of the columns.
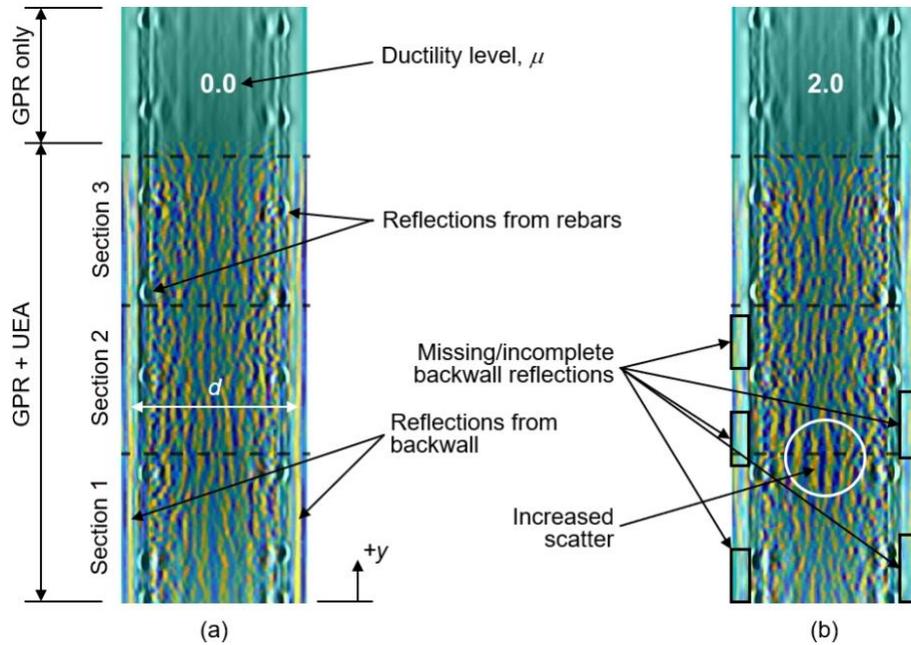
Figure 3-6. Sample final images Specimen 1 (South): (a) Baseline image (mu = 0) and (b) Image at mu = 2.0. Column width, d = 610 mm. The location and dimensions of the three designated sections of damage are shown in Figure 3-6. Final images for both specimens and additional ductility levels can be found in Appendix, Figure 3-13 to Figure 3-16.
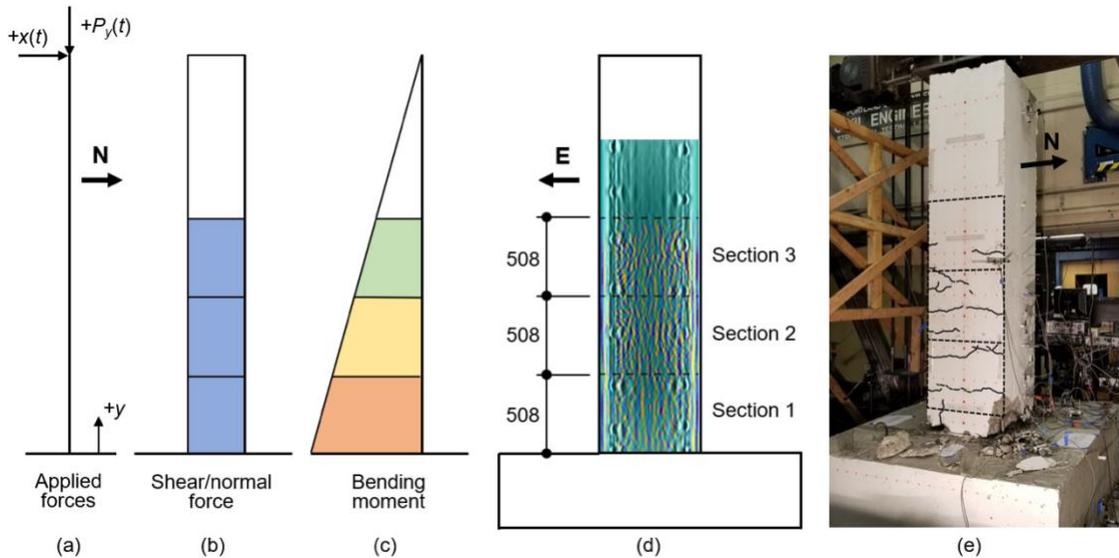
Figure 3-7 Illustrations of (a) applied forces, (b) and (c) internal force curves (qualitative), (d) elevation view of specimen north face with sample final reconstructed image and three designated damage sections, and (e) photo of east face of specimen after failure. All dimensions in (mm).

3.4.3. Structural similarity (SSIM) index

From the qualitative observations, we observed the changes in our images are not only from the loss of structural information of the image, but also, changes in the luminance and contrast of the images. For example, a missing of the backwall in some parts, is related to loss of structural information of the image, while increasing the amplitude of the ultrasonic reflectivity is more related to changes in luminance of the image. The popular SSIM metric from the field of image processing compares three relatively independent terms in two images, namely luminance, contrast, and structure, and hence is an ideal metric for our case. The luminance term, l is related to the intensity of the images and is computed by averaging the intensity of an image. To compare the luminance of two images x, y, Equation (1) is used.

$$l(x, y) = \frac{2\mu_x\mu_y + C_1}{\mu_x{}^2 + \mu_y{}^2 + C_1} \tag{1}$$

where μ_x, μ_y are the mean intensities of the images, and C_1 is a small number to avoid zero division. The contrast term, c is related to the standard deviation of each image. In other terms, contrast is the variability from the mean value. The contrast term, c is computed using Equation (2), as

$$c(x, y) = \frac{2\sigma_x\sigma_y + C_2}{\sigma_y{}^2 + \sigma_y{}^2 + C_2} \tag{2}$$

where σ_x, σ_y are the standard deviation of the images, and C_2 is a small number to avoid zero division. After subtraction of the luminance, l and variance normalization, the structure of the images is compared, which is the correlation coefficient, s between the

images. This correlation coefficient is similar to the metric introduced in [13] and can be calculated using Equation (3), as

$$s(x, y) = \frac{\sigma_{xy} + C_3}{\sigma_x \sigma_y + C_3} \tag{3}$$

where σ_{xy} is the cross covariance of the two images, and C_3 is a small number to avoid zero division. At last, the three terms of luminance, contrast, and structure are multiplied together to result in the SSIM metric defined by Equation (4), as

$$SSIM(x, y) = [l(x, y)]^\alpha \cdot [c(x, y)]^\beta \cdot [s(x, y)]^\gamma \tag{4}$$

where α, β, and γ control the relative importance of each measure. If we assign a similar weight of 1 to these variables, and assume $C_3 = C_2/2$, simplified SSIM values are computed, which is shown in Equation (5):

$$SSIM(x, y) = \frac{(2\mu_x\mu_y + C_1)(2\sigma_{xy} + C_2)}{(\mu_x{}^2 + \mu_y{}^2 + C_1)(\sigma_x{}^2 + \sigma_y{}^2 + C_2)} \tag{5}$$

It should be noted that we do not compute the SSIM value globally over the entire image, but rather, local SSIM values are computed using a 11×11 circular-symmetric Gaussian weighting function with standard deviation of 1.5 samples as suggested by the original article [21]. Given this, the final metric reported for comparison of the images over the entire image is the mean SSIM (MSSIM), which is the average value of SSIM over local windows, which we simply refer to as SSIM in the rest of this article. This metric is an

objective, reference-based index measuring the quality of an image with respect to a baseline image. An SSIM value of 1 means that two images are identical. Figure 3-8 shows the SSIM values for the north side and south side of both columns for comparing each loading stage with the baseline. It can be observed that SSIM values are steadily decreasing over ductility levels, $\mu = 0.5$ to 4.0 (3.2). It can be seen that there is a significant change in similarity of the baseline image and the first measurement after the baseline ($\mu = 0.5$). In addition, the results show a similar trend for both sides of both columns, which demonstrates the reliability of this method. The consistency in these results shows the robustness of this method in quantifying damage progression.
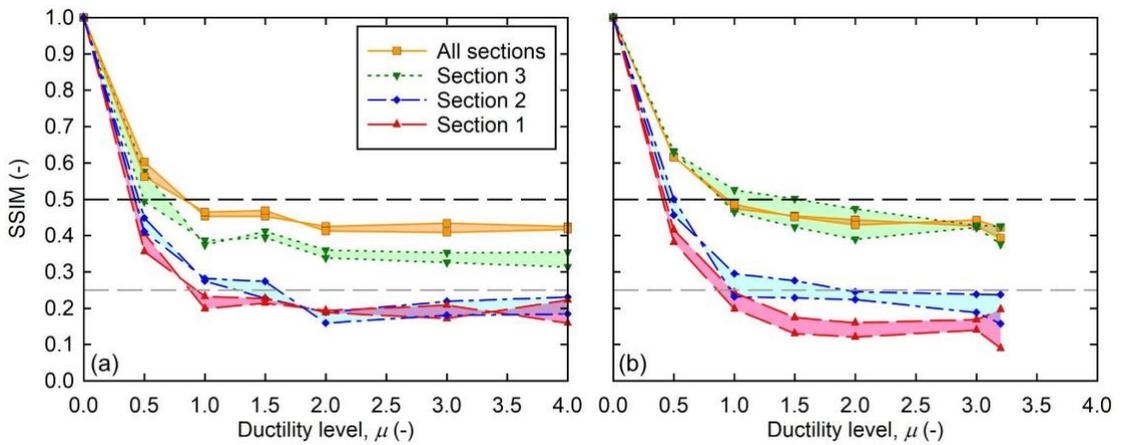
Figure 3-8. SSIM curves for (a) Specimen 1 and (b) Specimen 2. The dashed horizontal lines at 0.5 and 0.25 are provided for reference (location arbitrary).

In order to compare damage progression along the height of the column, we divided each column into three sections, each having a height of 508 mm [see Figure 3-7 (d)]. Also, we discarded the area of the images above Section 3 because either no or only GPR information was available. It can be observed that the SSIM values are consistently higher

71

at the base of the column compared to the areas above. This is consistent with the internal forces in the columns, as was discussed previously. It can also be seen that the bottom section of Specimen 2 has consistently lower SSIM values than the middle section, however, this is not completely the case for Specimen 1. This difference in the performance of the columns is explored further in the Section 3.4.4.

As hypothesized earlier, the internal changes in the fused images are mainly detected by ultrasound, and GPR might not be contributing the same level. In order to show the difference in the capabilities of these modalities, we quantified the results using only GPR, only UEA, and the fused image. Figure 3-9 shows the SSIM values for the entire height of the section (aggregate of the three sections along height) for the GPR image, the UEA image and the fused image. It can be seen that the changes are captured by UEA from early on, however, GPR is unable to detect and track the changes. This makes sense since ultrasound is sensitive to concrete-air interfaces such in cracks, but GPR energy is being reflected mostly from steel rebars.
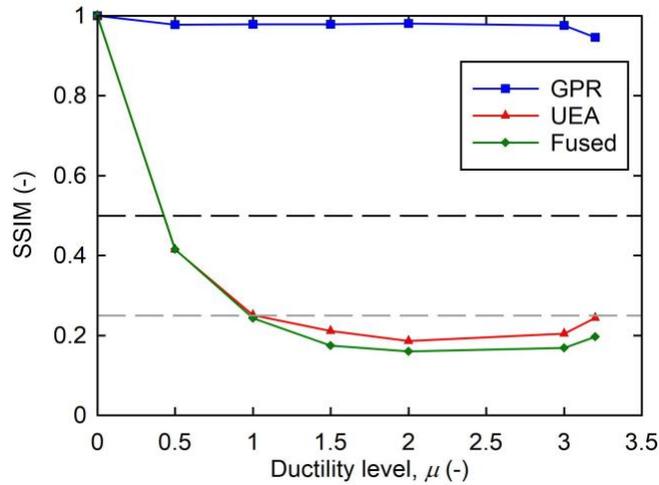
Figure 3-9. SSIM curves for GPR, UEA, and fused images (for Specimen 2, north

image).

3.4.4. Backwall analysis

As reported in [13], the shadowing of backwalls, caused by scattering of the ultrasonic

waves, can be used as an indicator of damage, in a controlled environment. This shadowing

effect is also visible in our fused images. However, this effect was not expressed

quantitatively in [13]. In order to quantify this effect, we propose a simple but effective

algorithm based on the US images only. In the baseline images (See Figure 3-6 (a) or

Appendix) we can see that the backwall is strongly present, suggesting that there is no

damage resulting in wave scattering or blocking. As damage progresses, the backwall

amplitude starts to decrease and is sometimes completely undetectable. Figure 3-10 shows

a narrow band that is tracked in all stages. The center of the band is the maximum amplitude

chosen in a small window where the backwall is present. The width of a band is 5 pixels,

where the maximum amplitude is the center of it. We take the average of these 5 pixels as

the value for that backwall intensity. Figure 3-11 and Figure 3-12 show the average

73

amplitude of the four backwalls for Specimens 1 and 2, respectively. The green area curve shows the mean backwall amplitude at each distance along the height of the column. The dashed black lines are separating the three sections and the red lines are showing the mean value for each section. The key observations are as follows:

- From left to right, which corresponds to increasing levels of damage (and increasing ductility levels), for both columns, the area under the curve, or mean value, of the backwall amplitude is decreasing. This is more visible in the bottom sections of the column and less in the top one, which suggests that the bottom section is more damaged. Looking at the red line from bottom to top, we can see it is more like a straight line at the beginning, and as damage progresses, it turns to a step like line increasing from bottom to top.

- Comparing the two specimens, Specimen 2 experiences larger and more sudden loss of amplitude in the backwalls. Even though Specimen 2 has a higher backwall amplitude at the beginning, it suddenly loses backwall amplitude at ductility 1.0, of 24%, whereas it is 14% for Specimen 1, and it goes up to 33% whereas it is 21% for Specimen 1. The same holds for the middle section, where Specimen 2 loses 19% of the mean backwall amplitude at ductility 1.0, whereas it is 9% for Specimen 1 and it goes to 24 % for Specimen 2 and 14 % for Specimen 1.

- It can be observed that the range of amplitude loss is lower in the middle section than the bottom section. For the top section, both columns lose only 8% of backwall amplitude at the most. This is in line with the findings reported at the structural

74

performance section where Specimen 2 has rapid strength degradation and lower energy dissipation.
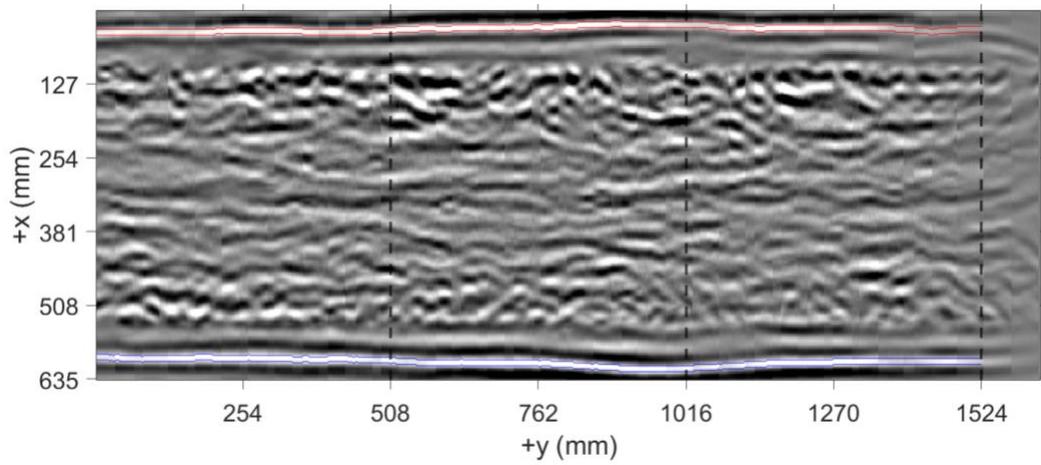
Figure 3-10. Illustration of the tracked backwall bands for Specimen 2, south side. Average values within the blue and red bands are used for the analysis.
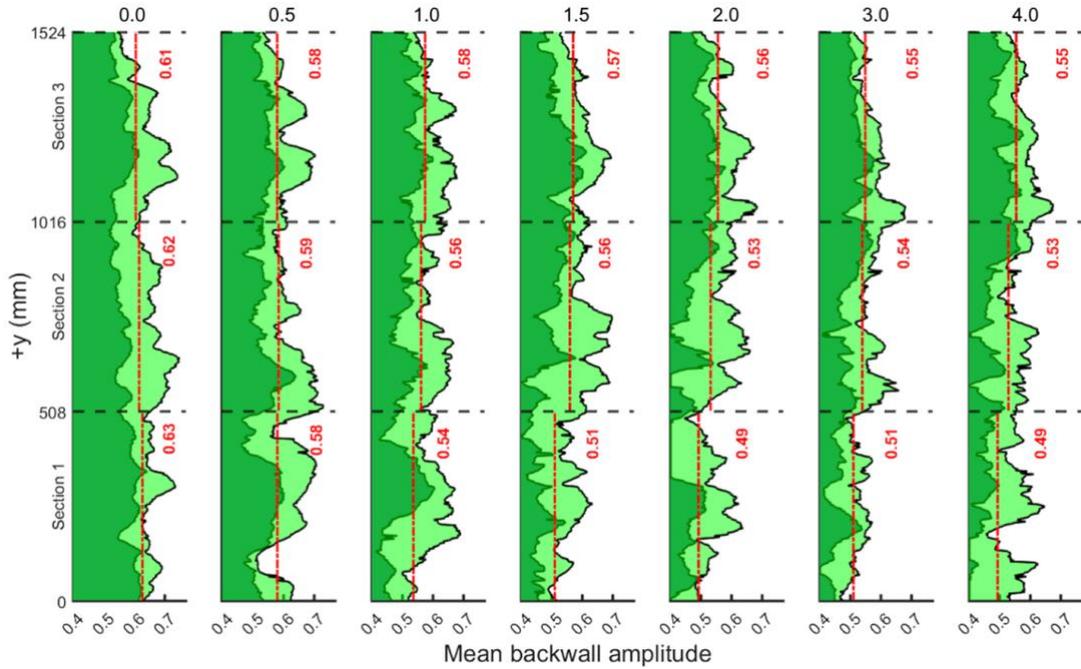
Figure 3-11. Mean backwall amplitude envelopes from all four measurements for Specimen 1. The numbers on top represent the ductility levels, μ.
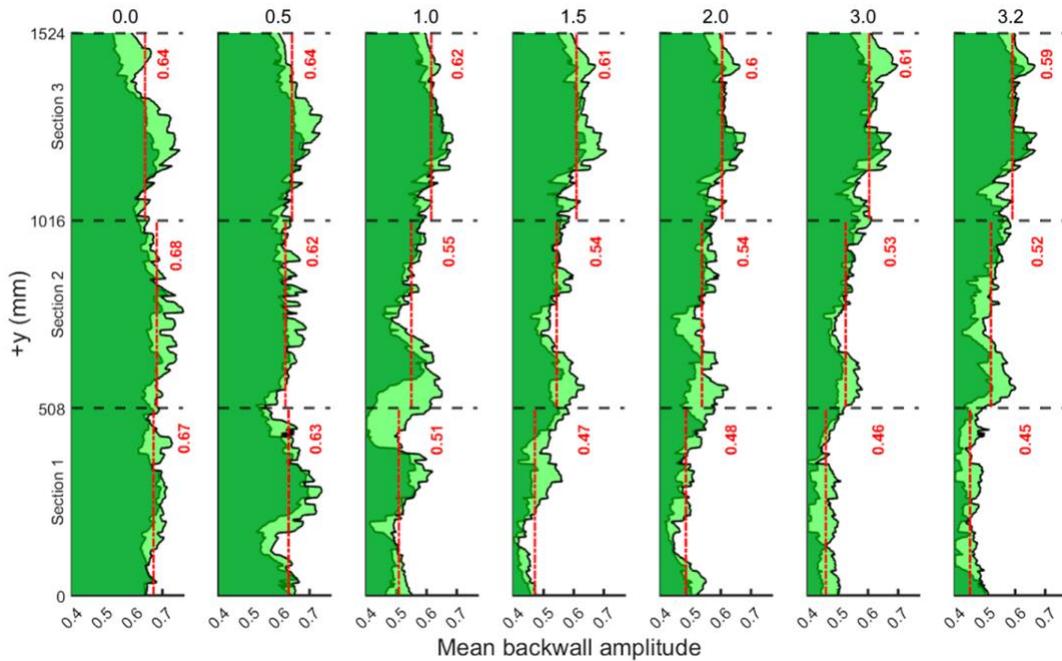
Figure 3-12. Mean backwall amplitude envelopes from all four images for Specimen 2. The numbers on top represent the ductility levels, μ.

3.5. Conclusion

In this study, two RC column-footing subassembly specimens were tested in the laboratory under reverse-cyclic loading and NDT was performed using ground penetrating radar (GPR) and ultrasonic echo array (UEA) measurements. The images were reconstructed using the extended total focusing method (XTFM) and image fusion was performed using wavelet decomposition to fuse all information from both modalities as well as from the east and west images. The ultrasonic measurements show the capability of tracking the damage with increasing levels of loading and damage. GPR is unable to detect changes but provides useful information regarding the location of rebars. The measurements were performed at an increment of 0.5 ductility levels. The results show that the changes are visible from the first measurement after the baseline. In addition, the results show that the base of the column is more damaged compared to the middle and top sections. A visual analysis of backwall amplitude and reflectivity maps are discussed and the results are quantified using the structural similarity index (SSIM) measure and a backwall amplitude analysis. The SSIM analysis shows that the damage can be tracked as early as the first measurement after the baseline. The backwall amplitude analysis provides a robust way of finding changes in ultrasonic images and locating the damage. Indeed, the backwall analysis agrees with the structural performance observations of the two test specimens. In addition, the images obtained from our fusion methodology show that the bottom section of the column experiences more damage than the middle and top sections and this is confirmed with both SSIM and mean backwall amplitude analysis. Based on the findings of this study and the other studies reviewed in the introduction, we conclude that obtaining a few baseline measurements after construction of a column can be a valuable asset to later

evaluate the condition of a concrete column, in particular after an earthquake. GPR measurements are useful for locating metallic features such as rebars and can be used in image fusion to create a more complete image of the interior of a member, but they do not add notable value in terms of detecting damage progression. The SSIM metric introduced is a valuable tool to detect the changes compared to the baseline. The mean backwall analysis and tracking the backwall, is a simple tool that provides the most information in terms of analyzing damage progression, as well as damage location along a member. In the future, the use of other modalities and more advanced methods in image reconstruction, especially for the ultrasonic will be investigated to further quantify the internal changes of the concrete.

Acknowledgements

3.6. References

[1]   Rojah, C. (2005). ATC-20-1 field manual: Postearthquake safety evaluation of buildings. *Applied Technology Council: Redwood City, CA, USA*.

[2]   Choi, H., Palacios, G., Popovics, J. S., & Chao, S. H. (2018). Monitoring Damage in Concrete Columns Using Ultrasonic Tomography. *ACI Structural Journal*, *115*(2).

[3]   Holmes C, Drinkwater BW, Wilcox PD (2005) Post-processing of the full matrix of ultrasonic transmit–receive array data for non-destructive evaluation. NDT E Int 38(8):701–711

[4]   Moghaddaszadeh, M., Adlakha, R., Attarzadeh, M. A., Aref, A., & Nouh, M. (2021). Nonreciprocal Elastic Wave Beaming in Dynamic Phased Arrays. *Physical Review Applied*, *16*(3), 034033.

[5]   Schickert, M., Krause, M., & Müller, W. (2003). Reconstruction by Synthetic Aperture Focusing Technique. *Advances and Developments in NDE Techniques for Concrete Structures*, *15*(3), 235.

[6]   Krause, M., Mielentz, F., Milman, B., Müller, W., Schmitz, V., & Wiggenhauser, H. (2001). Ultrasonic imaging of concrete members using an array system. *NDT & E International*, *34*(6), 403-408.

[7]   Pashoutani, S., Zhu, J., Sim, C., Won, K., Mazzeo, B. A., & Guthrie, W. S. (2021). Multi-sensor data collection and fusion using autoencoders in condition evaluation of concrete bridge decks. *Journal of Infrastructure Preservation and Resilience*, *2*(1), 1-12.

[8]   Clem, D. J., Schumacher, T., & Deshon, J. P. (2015). A consistent approach for processing and interpretation of data from concrete bridge members collected with a hand-held GPR device. *Construction and Building Materials*, *86*, 140-148.

[9]   Mehdinia, S., Schumacher, T., Song, X., & Wan, E. (2021). A pipeline for enhanced multimodal 2D imaging of concrete structures. *Materials and Structures*, *54*(6), 1-16.

[10]   Murtuz, A. K. M., Dusicka, P., & Schumacher, T. (2020). *Seismic Performance Design Criteria for Bridge Bent Plastic Hinge Regions* (No. FHWA-OR-RD-21-04). Oregon. Dept. of Transportation. Research Section

[11]   Polimeno, M. R., Roselli, I., Luprano, V. A., Mongelli, M., Tati, A., & De Canio, G. (2018). A non-destructive testing methodology for damage assessment of reinforced concrete buildings after seismic events. *Engineering Structures*, *163*, 122-136.

[12]   Choi, H., & Popovics, J. S. (2015). NDE application of ultrasonic tomography to a full-scale concrete structure. *IEEE transactions on ultrasonics, ferroelectrics, and frequency control*, *62*(6), 1076-1085.

[13]   Freeseman, K., Khazanovich, L., Hoegh, K., Nojavan, A., Schultz, A. E., & Chao, S. H. (2016). Nondestructive monitoring of subsurface damage progression in concrete columns damaged by earthquake loading. *Engineering Structures*, *114*, 148-157.

[14]   Hoegh, K., & Khazanovich, L. (2015). Extended synthetic aperture focusing technique for ultrasonic imaging of concrete. *NDT & E International*, *74*, 33-42.

[15]   Bazaez, R., & Dusicka, P. (2016). Cyclic loading for RC bridge columns considering subduction megathrust earthquakes. *Journal of Bridge Engineering*, *21*(5), 04016009.

[16]   Bazaez, R., & Dusicka, P. (2016). Cyclic behavior of reinforced concrete bridge bent retrofitted with buckling restrained braces. *Engineering Structures*, *119*, 34-48.

[17]   ACI-American Concrete Institute (2013) 228: 2R-13 Report on nondestructive test methods for evaluation of concrete in structures

[18]   Kohl, C., Krause, M., Maierhofer, C., Mayer, K., Wöstmann, J., & Wiggenhauser, H. (2003). 3D-visualization of NDT data using a data fusion technique. *Insight-Non-Destructive Testing and Condition Monitoring*, *45*(12), 800-804.

[19]   Pajares, G., & De La Cruz, J. M. (2004). A wavelet-based image fusion tutorial. *Pattern recognition*, *37*(9), 1855-1872.

[20]   MATLAB. (2022a). Natick, Massachusetts: The MathWorks Inc.

[21]   Wang, Z., Bovik, A. C., Sheikh, H. R., & Simoncelli, E. P. (2004). Image quality assessment: from error visibility to structural similarity. *IEEE transactions on image processing*, *13*(4), 600-612.

3.7. Appendix: Supplementary figures
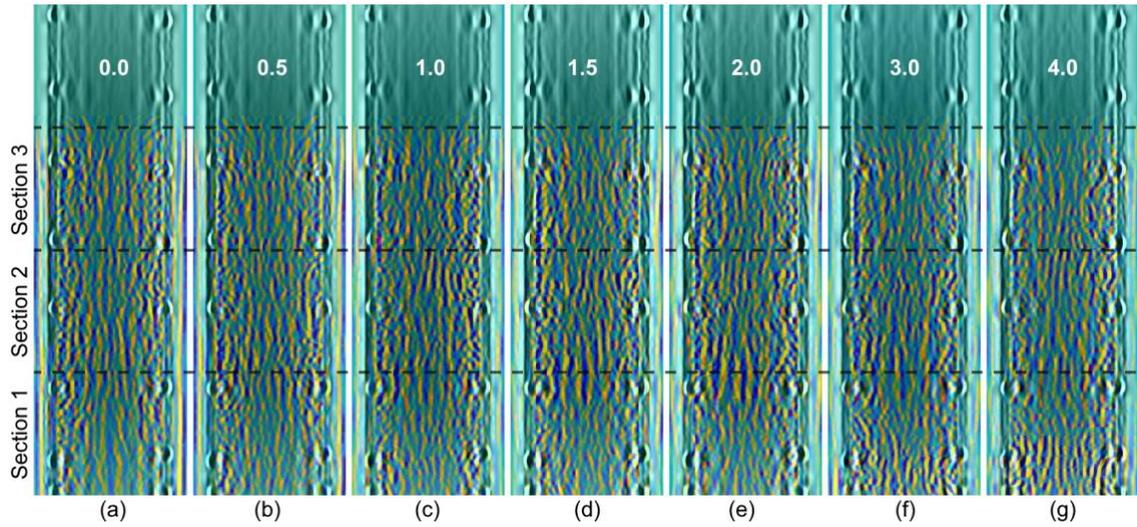
Figure 3-13 Reconstructed images Specimen 1, south scan: (a) to (g) correspond to ductility levels, $\mu = 0.0$ (= Baseline) to 4.0, respectively (also shown above Section 3). The location and dimensions of the three designated sections of damage are shown in Figure 3-6.
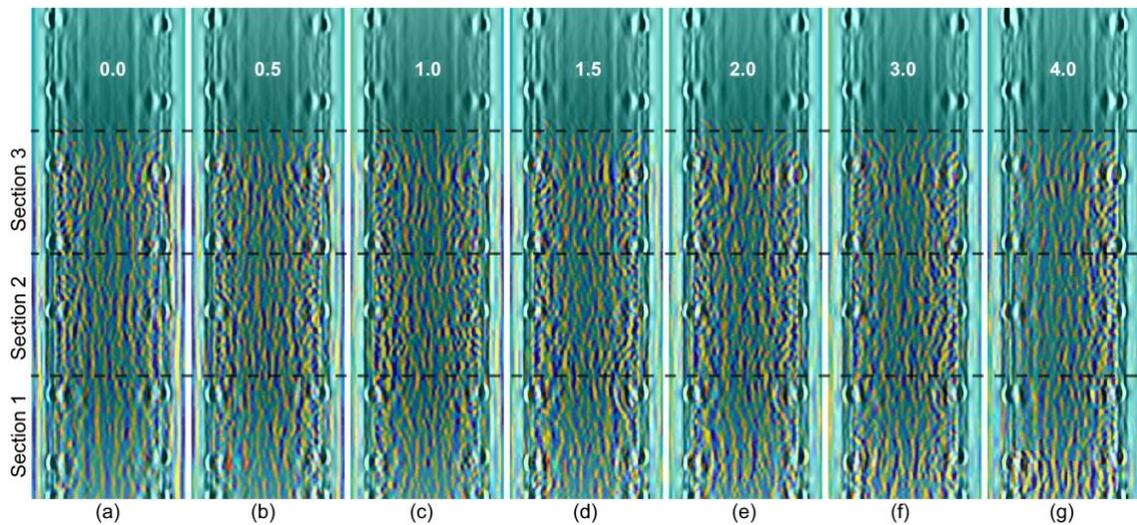
Figure 3-14 . Reconstructed images Specimen 1, north scan: (a) to (g) correspond to ductility levels, $\mu = 0.0$ (= Baseline) to 4.0, respectively (also shown above Section 3). The location and dimensions of the three designated sections of damage are shown in Figure 3-6.
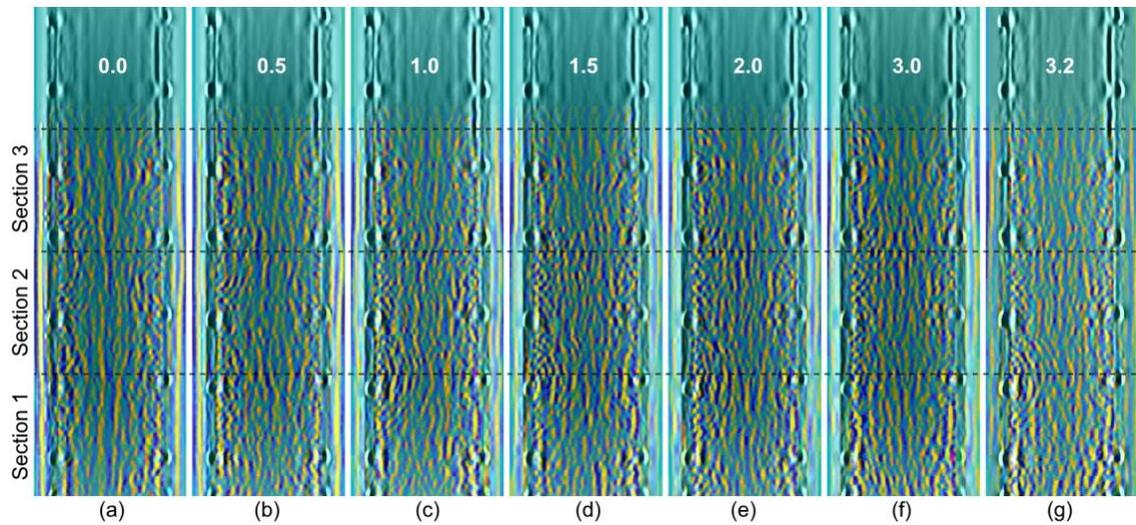
Figure 3-15. Reconstructed images Specimen 2, south scan: (a) to (g) correspond to ductility levels, $\mu = 0.0$ (= Baseline) to 3.2, respectively (also shown above Section 3). The location and dimensions of the three designated sections of damage are shown in Figure 3-6.
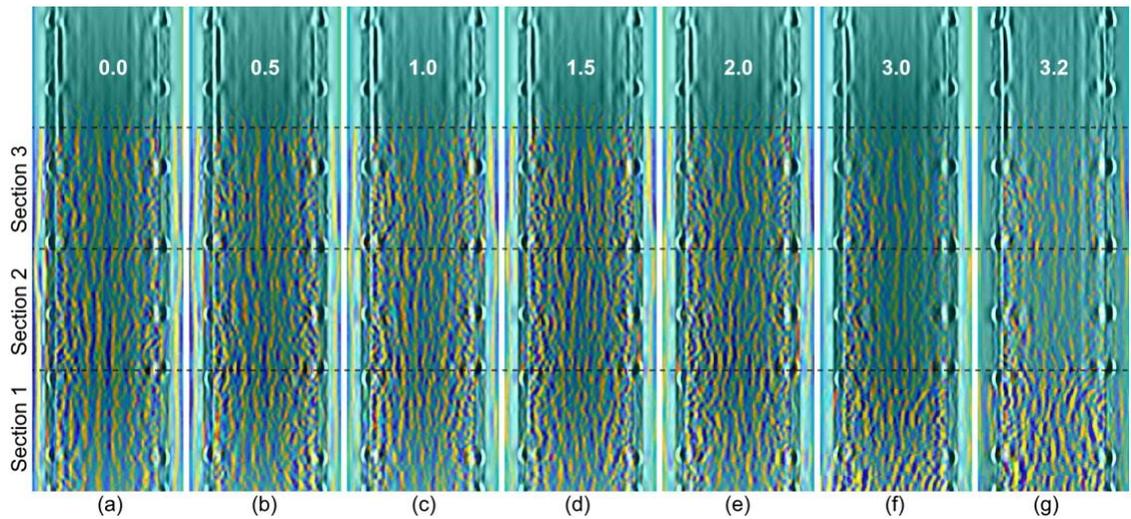
Figure 3-16 Reconstructed images Specimen 2, north scan: (a) to (g) correspond to ductility levels, $\mu = 0.0$ (= Baseline) to 3.2, respectively (also shown above Section 3). The location and dimensions of the three designated sections of damage are shown in Figure 3-6.

4. **Chapter Four: A Deep Learning and Simulation Pipeline for Image**

Reconstruction of GPR Data

Sina Mehdinia[1], Thomas Schumacher[2]

This article will be submitted to Journal Automation in Construction.

---

[1]PhD Candidate, Department of Civil and Environmental Engineering, Portland State University, Portland, OR, USA, E-mail: mehdinia@pdx.edu
[2]PhD, PE, Associate Professor, Department of Civil and Environmental Engineering, Portland State University, Portland, OR, USA, E-mail: thomas.schumacher@pdx.edu

Abstract

Image reconstruction on ground penetrating radar (GPR) B-scan data is usually performed with synthetic aperture focusing and migration techniques, which require prior knowledge of several parameters. For example, in the extended total focusing method (XTFM) algorithm, an accurate dielectric constant of the media, as well as an offset parameter, are required to reconstruct a focused image from the interior of a media, herein, reinforced concrete. Traditionally, this is done by a manual calibration process that requires knowledge about the depth of multiple reflectors in a structure. Deep neural networks can learn meaningful representations from raw data. In this study, we introduce a simulation and deep learning pipeline to generate high quality datasets, as well as learn from them. We propose a neural network model that can predict the dielectric constant of the media and the offset parameter, and thus, can reconstruct the focused image with high accuracy. In addition, we use model explainability techniques such as gradient visualization to show which areas of the images the algorithm is utilizing in the prediction process. We test the algorithm on real-world data from Chapter 2 and Chapter 3 and discuss the generalizability of it. In conclusion, the model performs has an excellent performance on the simulated data with an R2 coefficient of higher than 0.999 on both parameters. It has also been found that the neural network pays the most attention to the angle of reflections and the shape of a hyperbole resulting from a point reflector to predict the dielectric constant, and surface wave portion of GPR to predict the offset parameter.

Keywords: Ground penetrating radar, deep learning, synthetic aperture focusing, neural networks, B-scan, image reconstruction, dielectric constant

4.1. Introduction

Deep neural networks have been used widely in the prior decades to solve a variety of problems in engineering and science [1, 2]. While conventional machine learning algorithms require feature engineering and raw data transformation, deep learning methods are representation learning methods that are end-to-end, meaning that they can map an input to a desired output without the need for hand-crafting features. Indeed, with the proper amount of data, and computational resources, very complex nonlinear functions can be learned [1]. Each layer in a deep neural network learns a representation from raw data and passes it to the next layer where more abstract features can be learned. Convolutional neural networks are especially popular with image data [3, 4, 5] where the learnable weights of the neural network are convolutional filters. With the advances in graphics processing unit (GPU) architectures, and the introduction of new big datasets such as ImageNet [4], the performance of deep learning algorithms improved. For example, AlexNet, [5] introduced in 2012, changed the state-of-the-art of image recognition task by a significant margin.

In recent years, there have also been numerous studies with the application of deep learning, especially convolutional neural networks to detect rebars in GPR radargrams [6, 7, 8, 9], remove clutter in GPR images [10, 11], and GPR B-scan-to permittivity-map inversion [12, 13, 14, 15, 16, 17]. For example, Liu et al. [12] designed a deep neural network named GPRInvNet that performs image-to-image translation of GPR B-scans to dielectric maps for tunnel linings. Alvarez et al. [13] investigated encoder-decoder networks, and conditional generative adversarial networks to perform image-to-image

86

transformation of GPR B-scans to permittivity maps. Synthetic aperture focusing techniques (SAFT) to reconstruct dielectric maps from radargrams need prior knowledge about the medium such as the velocity of the electromagnetic wave. In our previous study, we proposed the extended total focusing method (XTFM) algorithm (Chapter Two), which can be used for both GPR and ultrasonic echo array (UEA) measurements, whether single or multi-channel, with overlapping measurements, to perform image reconstruction. Using XTFM, or similar focusing algorithms [18, 19, 20] all require at least a few parameters such as wave velocity of the medium, or dielectric constant of the material, and the time offset parameter. The time offset parameter is a function of the trigger time of the input waveform and the standoff distance of the GPR instrument from the surface of concrete [21]. These parameters can be obtained through calibration using trial and error until a perfect shape and correct position of the reflectors are achieved. However, in order to do this, multiple reflectors, such as reinforcing bars, and their exact positions should be known.

In order to tackle the image reconstruction of GPR B-scans we propose a GPR simulation and deep neural network pipeline that can be used to predict the two parameters used to reconstruct focused images. Even though many models in engineering applications can perform very well on test sets, it is important to be clear about the meaning of the technical term "generalization". Generalizing from a training set to an unseen test set is different from generalizing from a simulation to real-world data with a totally different underlying distribution [22, 23, 24]. A well-designed neural network that predicts accurately on unseen test sets can lose performance if there is a distribution shift in the data. Therefore, we see

87

data as the most important ingredient in designing such networks and a practical way to build a comprehensive GPR network that can be applicable in practice (real-world scenarios) is to share the simulated data and be clear about the details of the simulation generation.

In this study, we share our dataset and its related metadata at [25], which can be used for benchmarking. The metadata is the information about each simulation scenario that is saved (Table 4-1). gprMax [26, 27], a Python-based open-source electromagnetic simulation package, was used to generate the dataset in this study. A simulation pipeline was developed as a Jupyter notebook that simplifies the use of the original text-based interface of gprMax. Our dataset consists of 3000 data examples where frequency of the input waveform, dielectric constant of concrete, shape of the input waveform and number of rebars are variables. Fixed parameters include simulation time (time window) of the input waveform, other properties of the concrete such as conductivity, transmitter receiver distance, standoff distance of GPR antennas, and size of the specimen, all of which can affect the simulation results and define the limitations of neural network capability.

Table 4-1. The metadata generated automatically for an example simulation scenario shown in Figure 4-3. ID is the simulation number, gaussiandot is the derivative of Gaussian, and numOfrebars is the number of rebars.

ID	dielectric	waveform_type	frequency (Hz)	numOfrebars
8	6.03	gaussiandot	3e9	11

We ran some ablation studies to find a good model and parameters. We have tested the VGG16 architecture [28] with different layer modifications, and explored transfer learning, kernel initializations, augmentation techniques, and learning schedules. One of the unique contributions of this study is the use of model interpretability techniques and showing how a neural network can learn something meaningful and create knowledge that can assist engineers. We used feature visualization and gradient visualization methods to interpret our neural network and gain some insights into how the model is predicting the output parameters. As a matter of fact, the model showed us that the shape of a hyperbole resulting from a point reflector can be used to determine the dielectric constant of the media and the surface wave can be used to predict the offset parameter.

4.2. Methodology

4.2.1. Data

The first step in our proposed pipeline is to generate the dataset via simulation. gprMax, an open-source software is used to simulate GPR measurements. gprMax solves Maxwell's equations using the finite-difference time-domain (FDTD) method [26]. gprMax has a rudimentary text-based interface that makes it challenging to simulate a large number of datasets required for machine learning applications. We developed a Python notebook that can be easily read and executed without the need to use the text interface. This notebook is automated, can be customized, and can randomly create any number of different scenarios. We used this notebook to generate a 2D dataset consisting of 3000 data examples by varying some of the variables in each generation loop. The data are shared at our GitHub repository of the paper [25].

In all simulation scenarios, a *1.0 × 0.4* m concrete 2D cross-section with random placement of 1 to 19 rebars is generated. The number of rebars are not uniformly distributed since at some point during data generation, we decided to decrease the number of rebars. Figure 4-1 (a) shows a histogram of the used dielectric constants. Four different input waveforms were used, which are Gaussian, first derivative of Gaussian, second derivative of Gaussian, and Ricker (See Figure 4-2). The frequencies of the input waveforms, which are typical for concrete applications, range 1.5 to 3 GHz with increments of 0.1 GHz. Figure 4-1 (b) shows the distribution of the waveform frequencies used. Figure 4-1 (c) shows the number of data examples for each waveform type and Figure 4-1 (d) shows the distribution of the number of rebars in the dataset. The dielectric constant is in the range [4, 12] with increments of 0.01. This dielectric range is a typical range for concrete [29]. A simulation time of 10 ns was used to make sure every reflection of interest has enough time to return to the receiver. A spatial resolution of 2 mm was used for all simulations. The radius of the rebars ranged from 6 to 20 mm in increments of 2 mm, which is equal to the spatial resolution. The rebars can be placed randomly anywhere, and a check is performed to make sure they do not overlap. Conductivity, relative permeability, and magnetic loss of the concrete were kept constant at 0.01, 1, and 0, respectively for all simulations. The domain is automatically calculated by adding 20 cells to the top, left, and right of the specimen. Figure 4-3 (a) shows the geometry of a sample simulated specimen. The black area shows the space between concrete, the antennas, and the domain. This area is added to make sure no objects are placed in the absorbing boundary conditions. The small blue rectangles indicate the source at the first recording position and the last. The distance between transmitter and receiver is 40 mm and the standoff distance of the instrument is 2 mm. The red circles show the

randomly placed rebars inside the concrete. Figure 4-3 (b) shows the B-scan generated from this scenario. All B-scans are downsampled to have a time axis with 510 data examples. The output size of one simulation scenario is a 510×481 matrix, where 510 is the number of amplitudes in the time domain, and 481 is the number of simulated measurements, i.e., A-scans.

GPU parallelization can be used to generate the data in gprMax [27]. 1877 of data examples are generated using a virtual device provided by Google with a Tesla P-100 GPU and 27.3 GB of random access memory (RAM), and the rest of the data examples are generated on a NVIDIA A-100 GPU with 40 GB of RAM. The 3000 data examples in the dataset are split into training and validation sets with 2700 and 300 data examples, respectively. The validation set is used for experiments to find the best practices of model architecture and learning schedules. An extra 20 data examples with only one rebar are generated as an extra test set for explainability experiments, which is discussed in Section X. Three real GPR scans were also set aside to test the ability of the proposed method to generalize on real-world data.
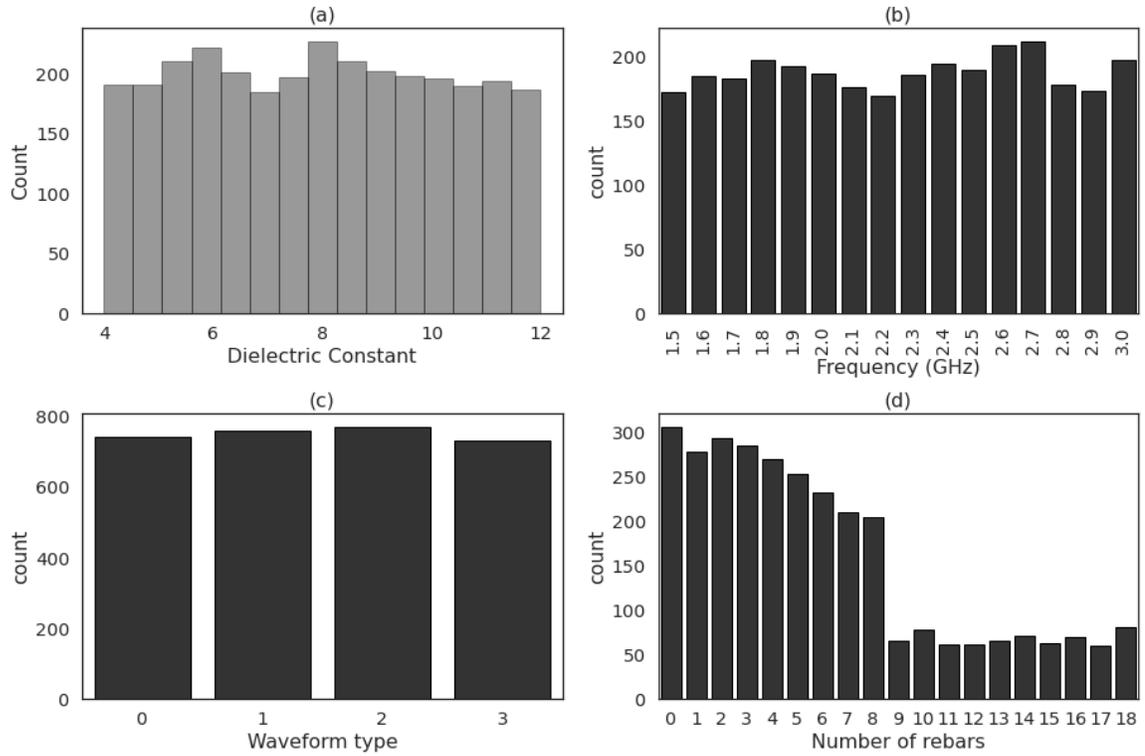
Figure 4-1 Distribution of variables in generated dataset: (a) Histogram of dielectric constant, (b) count plot of input waveform frequency, (c) count plot of waveform type, and (d) count plot of number of rebars
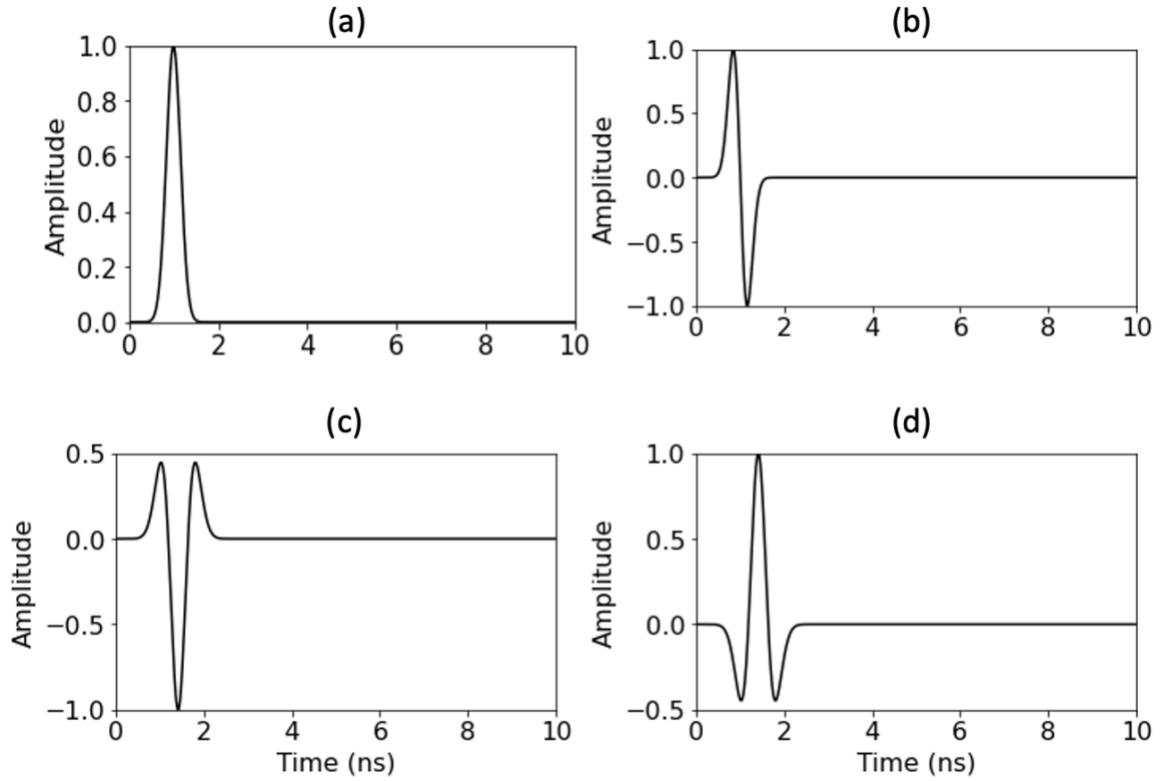
Figure 4-2. Time-histories of four types of waveforms employed to generate the dataset used in this study: (a) Gaussian, (b) first derivative of Gaussian, (c) second derivative of Gaussian, and (d) Ricker
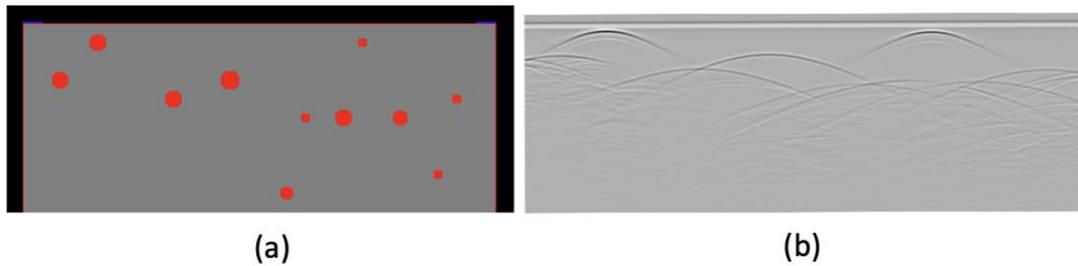
Figure 4-3. (a) Geometry of a sample simulation domain, with concrete shown in gray, rebars in red, and the blue boxes are the first and last position of the GPR instrument. The black area is air(b) Sample generated B-scan resulting from (a)

4.2.2. XTFM

The extended total focusing method (XTFM) is an algorithm recently developed by the authors that can reconstruct images from multi-channel GPR and UEA images with overlapping measurements (Chapter Two). It was written in MATLAB and Python and is open-source available at [30]. Two parameters, namely wave velocity of the medium, v and as the time offset, ϵ, are required inputs and need to be determined experimentally. With an assumption that these parameters are deterministic and uniform throughout the entire specimen, tuning these two parameters results in correct depths and shapes of reflectors. The procedure for tuning these two parameters is done by manual calibration and requires some knowledge of the specimen such as the depth of the specimen or the depth of reflectors such as rebars. In order to arrive at a unique set of parameters, multiple known reflectors should be used in the calibration process. However, in practice, this is not always possible. Thus, we suggest and evaluate a deep neural network model that can predict the dielectric constant and time offset parameters and help us with the manual tuning. Wave velocity is directly related to the dielectric constant of the material and can be obtained by dividing the speed of light by the square root of the dielectric constant [21]. Since the input waveform is known in simulations, the time offset parameter can be calculated by the following Equations (1) and (2).

$$\epsilon = \frac{1}{f} \text{ for Gaussian and derivative of Gaussian waveform} \tag{1}$$

$$\epsilon = \frac{\sqrt{2}}{f} \text{ for second derivative of Gaussian and Ricker waveforms} \tag{2}$$

where f is the frequency of the input waveform in GHz. This equation holds true for simulations, where the delay of the input waveform is calculated with respect to frequency, however, in real-world data, we do not know the input waveform and the offset parameters. The distance of the GPR to the surface of the concrete also contributes to the time offset parameter. Since it is only 2 mm in this dataset, it is negligible. In practice, the input waveform of the instruments and their time of trigger are unknown, and the GPR standoff distance can be higher. Thus, having a neural network predicting this unknown parameter can be valuable.

4.2.3. Model Architecture

In order to find the optimal architecture, we ran ablation studies. For the architecture of the model, we found that having a few hidden layers consisting of convolutional and pooling layers achieves accurate results with low mean absolute error in comparison with more complex models. VGG16 is a powerful architecture that consists of five convolutional blocks with a total depth of 16. The number of channels in each convolutional block increases from 64 at conv1 (See Figure 4-4) to 128 at conv2, 256 at conv3, and 512 at the conv4 and conv5 blocks. The first and second convolutional blocks (conv1 and conv2) have two successive 2D convolutions, while the rest of convolutional blocks have three 2D convolutions. Each of the convolutional layers is followed by a RELU nonlinearity and each convolutional block by a max-pooling operation.

We experimented with some changes to the original VGG16 to find the most suitable model. In the end, the selected architecture has the core five convolutional blocks of VGG16. A global average pooling layer was added after the last convolutional block and

two dense layers consisting of 512 neurons each with a RELU activation and a final linear

dense layer were added to predict the two parameters. Figure 4-4 illustrates the architecture
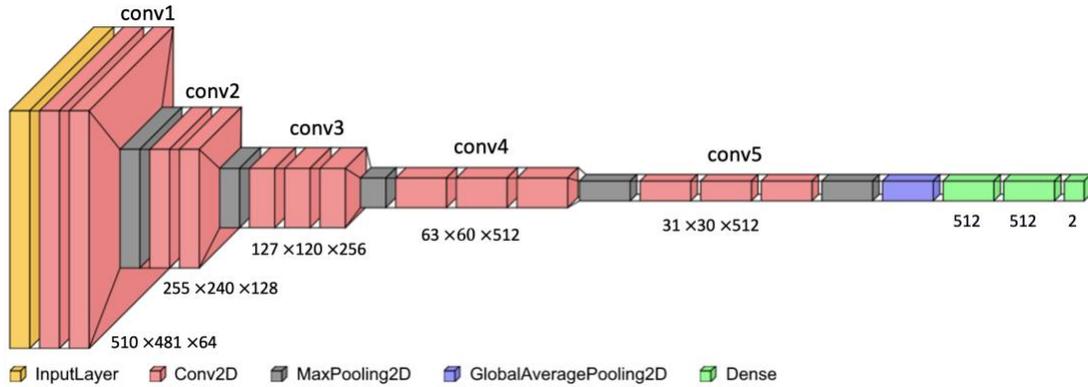
of the used model.

Figure 4-4. Architecture of the used model. The architecture is drawn using visualkeras
[31]

4.2.4. Data Preprocessing

Preprocessing of the data consisted of normalizing them to be in the range of 0 and 1. We

do not perform image resizing, a common procedure in computer vision, since this

operation distorts the time axis of the B-scan images and can change information for

learning the time-depth conversion. In addition, we do not perform common B-scan

preprocessing such as direct wave removal. Indeed, as is demonstrated later, the direct

wave is crucial for our model to learn the offset parameter. The ground truth values of the

time offset parameter are multiplied by 10 and then the predictions are divided by 10. The

reason for this is that the dielectric constant and time offset parameters both contribute to

the loss with the same weight, and it is important to have them on the same scale. Otherwise, weights should be assigned to calculate the loss values.

4.2.5. Loss Function

The mean absolute error (MAE) or L1 loss is chosen as the loss function. In addition, the mean squared error (MSE) or L2 loss is also employed as a reported metric. The MAE is simply the mean difference between ground truth, y and predictions, $\hat{y}$ [Equation (3)], while MSE squares the variables before averaging them [Equation (4)]:

$$L_{MAE}(y, \hat{y}) = \frac{1}{n}\sum_{i=1}^{n}|y - \hat{y}| \tag{3}$$

$$L_{MSE}(y, \hat{y}) = \frac{1}{n}\sum_{i=1}^{n}(y - \hat{y})^2 \tag{4}$$

y is the ground truth, $\hat{y}$ is the prediction and n is the number of data examples.

4.3.   Results

4.3.1. Implementation Details

Our deep learning solution is written in Tensorflow [32] and Keras [33] and is publicly available at [25]. The Tensorflow data pipeline is used to load the dataset and Albumentations [34] is used for data augmentation. The models are trained on four A-100 NVIDIA GPUs with 40 GB of RAM (4 × A100 40 GB). The model is trained with distributed parallel training with a total batch size of eight, distributed on the 4 GPUs. The Tensorflow and Numpy seeds are set to 23, however, there is still randomness due to distributed training that cannot be avoided. Following the methodology proposed in this

article may produce slightly different results. One approach is to run the algorithm many times and average the results. We avoided such computations due to limitations of our computational resources and the fact that the results are very similar. In addition, fixating too much on random seeds, hyperparameter tuning, and selective reporting are not subjects of this article.

4.3.2. Training Schedule

Each experiment was trained for 150 epochs with early stopping to avoid overfitting. Early stopping has a patience of 10 epochs if the validation loss is not improved by a minimum of 0.001. For the optimizer, the Adam optimizer [35] was used. Adam is one of the adaptive learning algorithms that is relatively robust and has shown to result in better optimization than traditional gradient descent without momentums. With the progress of the training, it is usually useful to reduce the learning rate, thus a cosine decay scheduler is used [36]. At each training step, a cosine decay function is applied to reduce the learning rate. The initial learning rate is set to 10^{-4}. Figure 4-5 shows the learning rate scheduler. The validation loss is monitored to be minimized and a checkpoint callback returns the model with the minimum validation loss. The VGG16 architecture with a global average pooling after the convolutional layers followed by a linear dense layer is tested with and without the learning scheduler. Table 4-2 shows the validation MAE and MSE for this matter. It can be seen that using a learning rate scheduler can enhance the performance. Figure 4-6 (a) and (b) show the learning curves for training and test sets with and without scheduler, respectively. It can be seen that without the learning scheduler the model is stopped early at epoch 25, while by lowering the learning rate at later epochs, the model keeps minimizing the loss.

98
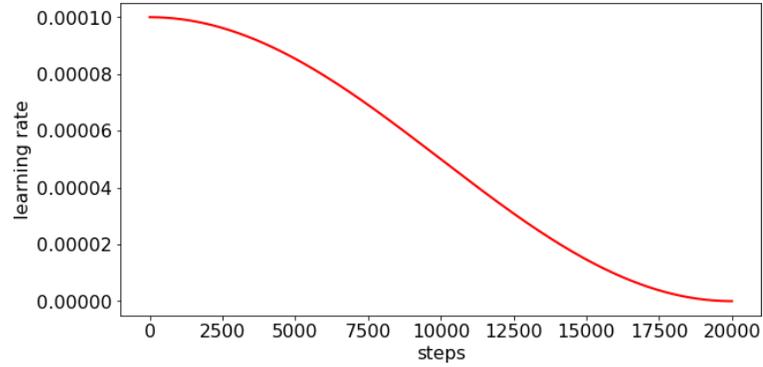
Figure 4-5. Cosine decay learning rate function starting from the initial rate of 10^{-4}

Table 4-2. The result of training with and without the cosine decay schedule, respectively

Learning schedule	Validation MAE	Validation MSE
With cosine decay	0.0236	0.0019
Without cosine decay (constant learning rate)	0.0812	0.0154
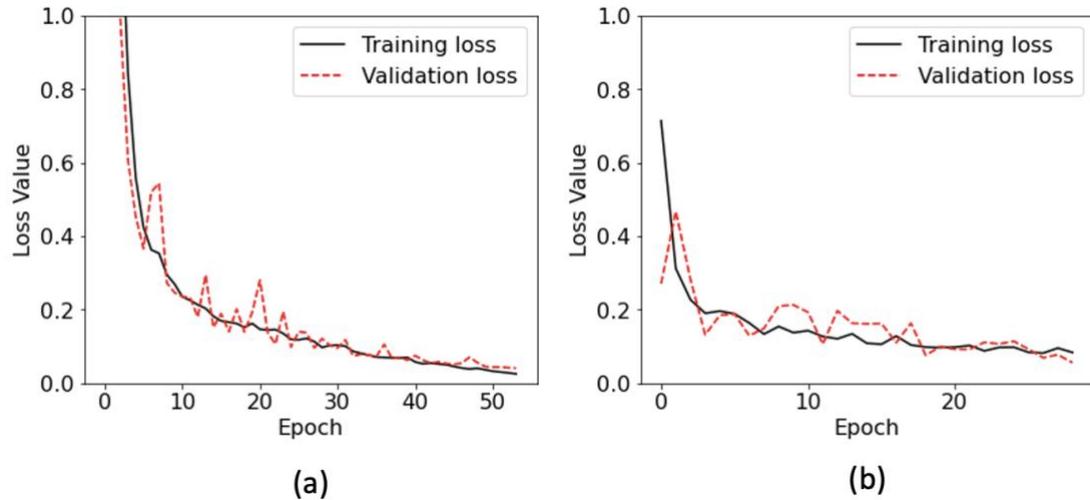
Figure 4-6. Learning curves of the two models: (a) with cosine decay learning scheduler and (b) without learning schedule (constant learning rate).

4.3.3. Experiments

We first define a base core model, which is a regular VGG16. We remove the top dense layers, and use the regular five convolutional blocks, followed by a global average pooling layer, and a linear dense layer with two neurons, to predict the two parameters. This model has 14.7M (million) parameters and 13 convolutional layers. The first experiment is to test the effect of kernel weight initialization, whether to use a random weight initialization or use the pretrained ImageNet weights. Kernel initialization can affect the performance of neural networks. Since the first few layers of convolutional neural networks usually learn simple concepts such as presence of edges and or their orientations [1], initializing the network with learned ImageNet weights may benefit our problem as well. It can be seen in Table 4-3 that initializing the weights with weights from the model pretrained on ImageNet

results in better performance. Thus, we will use ImageNet initialization for the rest of our experiments.

Table 4-3. Effect of weight initialization on performance of the base model

Weight initialization	Validation MAE	Validation MSE
Random	0.0407	0.0052
Pretrained on ImageNet	0.0236	0.0019

Since using initial ImageNet weights helped our network, we considered the idea of transfer learning and freezing some of the initial layer weights to see how it affects the performance. In this case, the network will only do backpropagation and weight updating for the unfrozen layers and use the frozen layers as the fixed feature extractor. As can be observed, the features learned for ImageNet classification tasks are not going to help our problem, but the features in the very early layers might be useful. As can be seen in Table 4-4, freezing the weights does not improve the performance. It is interesting to note that freezing the weights for the first two and even three convolutional blocks does not significantly worsen the results. Given the fact that initializing the weights with ImageNet pretrained weights improves our result from the previous experiment, it can be inferred that learned ImageNet weights in the early layers are not far from our application here.

Table 4-4. The results of experimenting with transfer learning

Modification	Val MAE	Val MSE
Freezing the first 2 convolutional blocks	0.0255	0.0018
Freezing the first 3 convolutional blocks	0.0290	0.0022
Freezing the first 4 convolutional blocks	0.1457	0.0345

Next, we experiment with different architectures by imposing a few variations. We apply the same modification for our VGG16 base model to the VGG19 architecture. VGG19 is similar to VGG16 except that the third, fourth, and fifth convolutional blocks have a depth of four instead of three (as in VGG16) with a total depth of 16 convolutional layers. The model has 20M parameters. It can be seen in Table 4-5 that using the VGG19 as the core did not improve the performance, therefore we continue our experiments with the VGG16 architecture as the core. Please note the original VGG16 and VGG19 have 138.4M and 143.7M parameters where most of the weights come from the top dense layers, which are removed in our base model.

Next, we remove the last convolutional block, and the last two convolutional blocks of the base model, respectively, to see if reducing model depth and complexity benefits our problem. This reduces the number of parameters from 14.7M to 7.6M and 1.7M parameters

respectively. However, as can be seen in Table 4-5, the performance is reduced. Next, we add two dense layers with 512 neurons followed by RELU activation to the model, once after the global average pooling layer and once before the global average pooling layer, this time followed by a max pool. It can be seen that adding dense layers after the global average pooling layer and before the final linear dense layer has indeed improved the performance. We keep this model as our selected model for the rest of the work.

Table 4-5. Results of experiments for modifying the architecture (used model shown in bold)

Model	Validation MAE	Validation MSE
VGG 16 core	0.0236	0.0019
VGG19 core	0.0256	0.0018
Removing last convolutional block of VGG16	0.0270	0.0021
Removing the last two convolutional blocks of VGG16	0.0610	0.0124
Adding two 512 dense layers layers after global average pooling	**0.0224**	**0.0014**
Adding two 512 dense layers and a max pool before global average pooling	0.0253	0.0017

In the next step, we explore the effect of augmentation. Proper augmentation can benefit the network to be exposed to different inputs and have a better generalization ability and reduce overfitting. Even though we are not seeing any overfitting in the previous experiments, we believe that training the network with randomized augmentations may result in better performance for testing on real GPR test cases. In this study, we propose a few methods that can be useful to be applied to GPR data. We experimented with these proposed augmentation techniques and report our findings in Table 4-6. The following techniques five techniques were explored:

- **Gaussian Noise**

  With a probability of 0.5, random Gaussian noise with zero mean and a standard deviation sampled uniformly over (0, 0.01) is added to the input B-scan. Figure 4-7 (b) shows the resulting image after applying this augmentation with a standard deviation of 0.01 to the example B-scan shown in Figure 4-7 (a).

- **Gaussian Blur**

  With a probability of 0.5, random Gaussian blurring with a kernel size sampled uniformly across (3, 21) is applied to the input B-scan. Figure 4-7 (c) shows the resulting image after applying this augmentation with a kernel size of 15 to the original B-scan.

- **Random Brightness and Contrast**

  With a probability of 0.5, brightness and contrast of the input B-scan are changed based on a random sample uniformly chosen from (-0.2, 0.2) for both operations.

Figure 4-7 (d) shows the resulting image after applying this augmentation with a brightness of -0.2 and contrast of 0.2 to the input B-scan.

- **Multiplicative Noise**

  With a probability of 0.5, each pixel of the input B-scan is multiplied with a value sampled uniformly from (0.8, 1.2). Figure 4-7 (e) shows the resulting image of applying this augmentation with values sampled uniformly from (0.8, 0.2) and applied elementwise to the input B-scan.

- **Solarize**

  With a probability of 0.5, pixels are inverted if they are above a threshold sampled uniformly over (0, 0.5). Figure 4-7 (f) shows the result of applying this augmentation with a threshold of 0 to the input B-scan.

The results of applying the aforementioned augmentations and retraining the model are shown in Table 4-6. It can be seen that augmentation is not helping the network but decreasing its ability to properly fit to the data. However, it can still be useful practice if our validation set was coming from real-world data or other unseen distributions. Since we have only three real-world test cases and the goal in this paper is not to optimize the results for these three, but the validation set, we decided to not use augmentation in our final model.
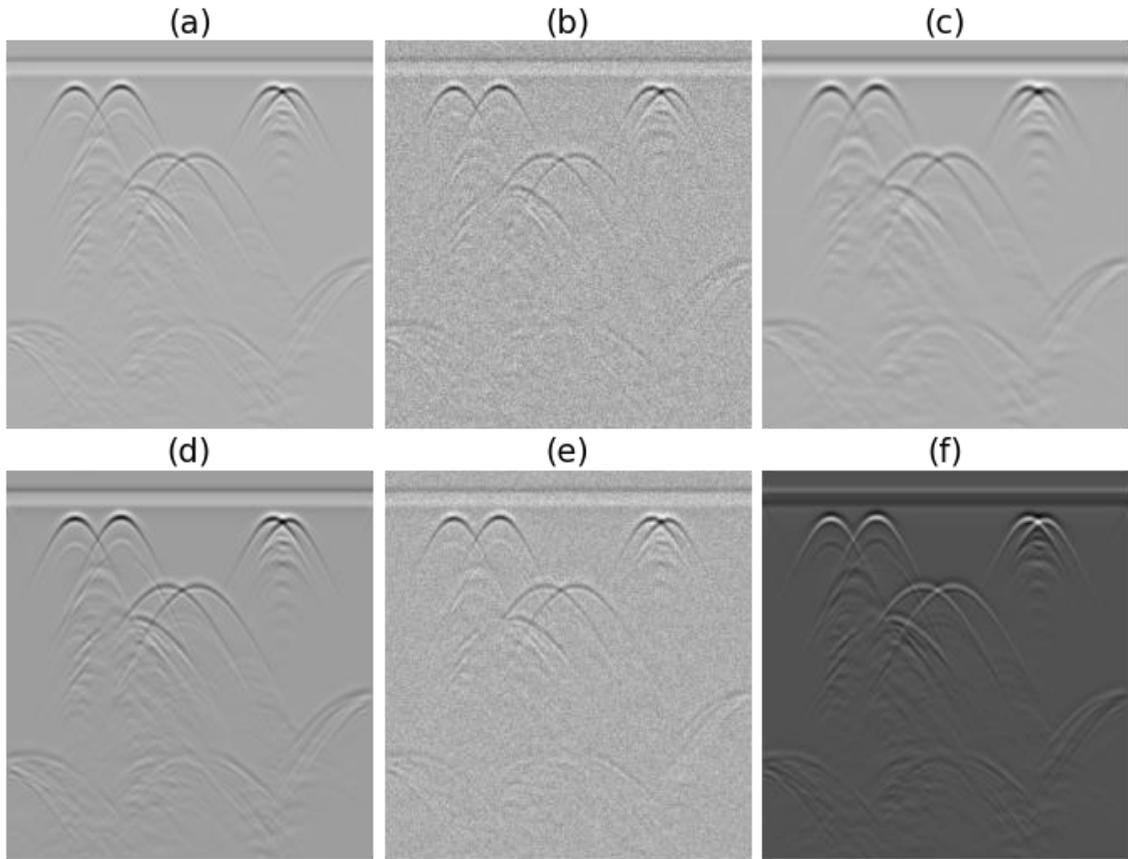
Figure 4-7 (a) Original input B-scan and resulting augmented image: (b) Gaussian noise with zero mean and 0.01 standard deviation, (c) Gaussian blur with kernel size of 15, (d) brightness of -0.2 and contrast of 0.2, (e) multiplicative noise in range of 0.8 to 1.2, and (f) solarize with 0 threshold (inversion)

Table 4-6. The results of experiment with proposed augmentations

Modification	Validation MAE	Validation MSE
With proposed augmentations	0.0485	0.0054

Finally, we explore the effect of the dataset size. As reported earlier, the training set size was 2700 data examples. The experiments are to train with only ¼ (= 675 data examples)

106

and ½ of data (= 1325 data examples), respectively. We found that to have a fair comparison, the training steps and learning schedule should be the same as the full-size dataset. Thus, the batch size was reduced to two, and four for the quarter and half datasets, respectively, while it was eight for the full dataset. This results in the same number of training steps in each epoch as the original full-size dataset. Table 4-7 summarizes the results. It can be observed that the model does not converge well if the batch size is not reduced. However, the performance of the model increases when the batch size is reduced, even with only 675 data examples. This shows that this model can learn the required parameters to predict the output with high accuracy with a low amount of training examples.

Table 4-7. The results of experiment with changing the dataset size and batch size

Dataset size	Validation MAE	Validation MSE
675 data examples with batch size of eight	0.1064	0.0231
675 data examples with batch size of two	0.0528	0.0104
1350 data examples with batch size of eight	0.0838	0.0135
1350 data examples with batch size of four	0.0369	0.0048

Full-size 2700 data examples with batch size of eight	0.0224	0.0014

We continue to report our findings with the best model in the validation set, which has the five blocks of VGG16 as the core, followed by a global average pooling layer, two dense layers with RELU, and a final linear dense layer. The whole layers are set to be trainable, without any augmentation and with a cosine decay scheduler. We use the model trained on the full-size dataset to report our findings. Figure 4-8 shows the performance of the model on the unseen 300 validation set. Figure 4-8 (a) and (b) show the actual and predicted values for dielectric constant and offset parameter, respectively. It can be seen that the model's performance is excellent on the validation set where the R^2 value is higher than 0.999 for both. Figure 4-9 (a) shows sample B-scans from the validation set and Figure 4-9 (b) shows the XTFM image resulting from applying the predicted parameters to the sample B-scans. The red faded circles are showing the actual position and shape of the reflectors, i.e., rebars. It can be seen that the reconstructed XTFM images are extremely well focused, and the vertical position of the reflectors is correct. Please note that not all reflectors were represented in the input B-scan, that is why some ground truth red circles have missing reflections. This is due to the limitation of GPR in reflecting bottom reflectors, where the wave is blocked by the top reflectors.
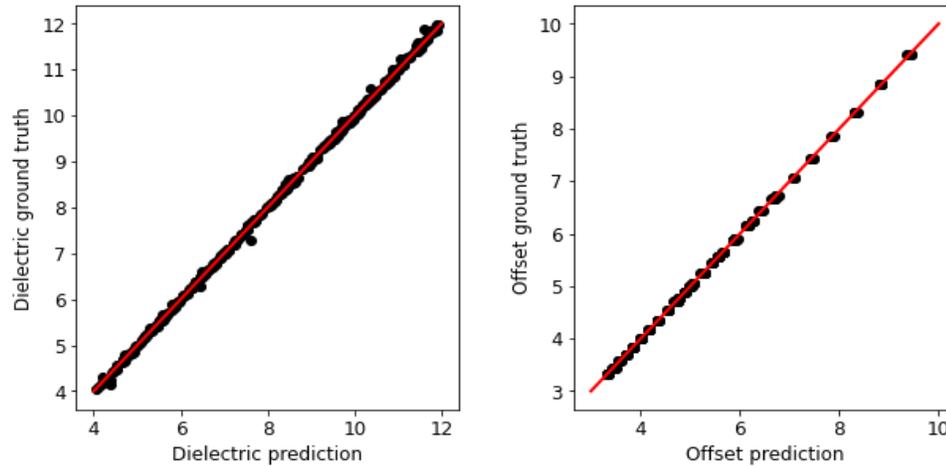
Figure 4-8 The actual and predicted values on validation set for (a) dielectric constant and (b) time offset parameter. The R^2 value is higher than 0.999 for both.

4.3.4. Testing on Real Data

The fact that the model trained on the simulated dataset can predict accurately on unseen simulated data is valuable. It suggests that if one collects real data from specimens with known features, such as the precise placement of rebars, and labels them with tuned dielectric and offset parameters, one can use these deep neural network models as the one suggested in this paper to train and predict correctly on unseen real data. Since generating real data can be a time-consuming process, we evaluate whether models trained on simulated datasets can perform decently on real-world data. Therefore, we test our model on data collected from Chapter 2 and Chapter 3. First, we test the algorithm on the three experimental specimens that were built in the laboratory (See Chapter 2). Figure 4-10 shows the elevation view of these specimens, which are described in detail in Chapter Two. We collected B-scans from the three test specimens using a GSSI miniXT instrument with a central frequency of 2.7 GHz, and an unknown input waveform with a recording length of 8.41 ns. The size of the B-scans is 510×450, where 510 is the number of samples and

109

450 is the number of A-scans. A-scans were recorded every 2.5 mm (= spatial resolution). The input for our neural network model was 510×481. Instead of resizing the input, we simply repeat the last 31 pixels to make their size equal to the simulated dataset.
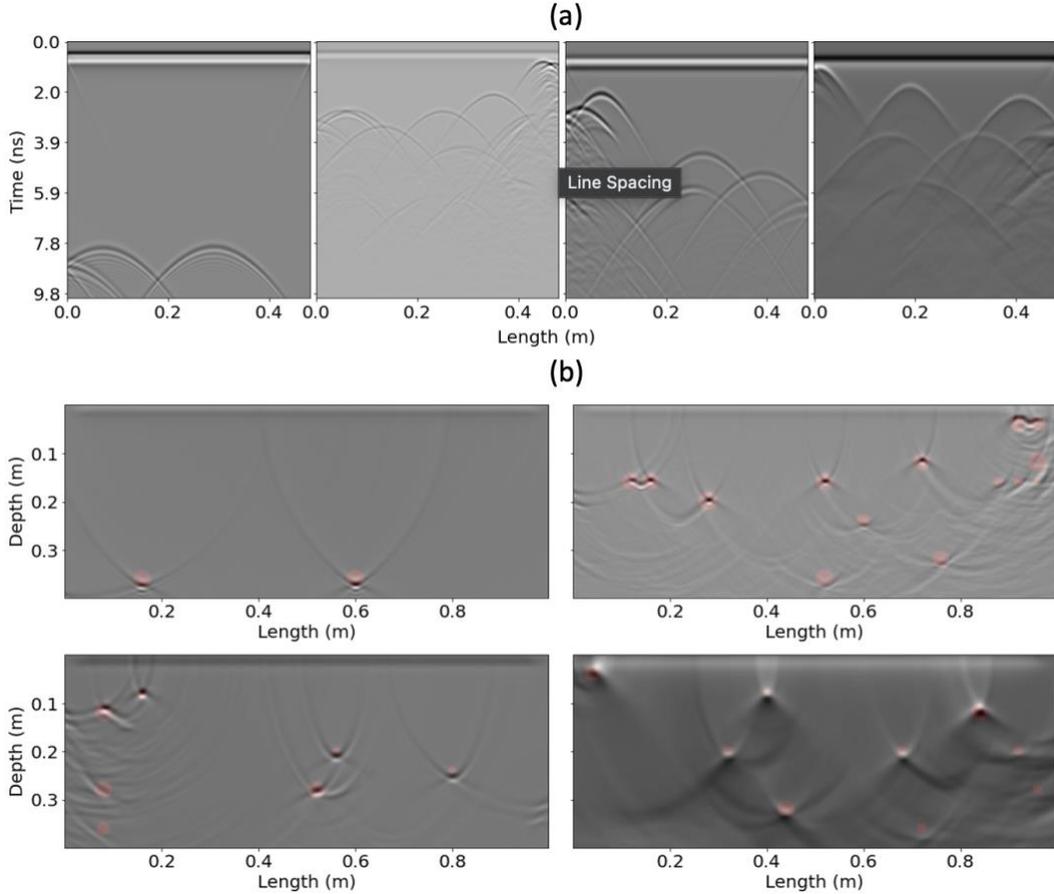
Figure 4-9. (a) Four sample B-scans from the validation set, and (b) their respective reconstructed XTFM images using the predicted parameters from the output of the model

Table 4-8. Predicted parameters of the dielectric constant and time offset for three test specimens

Test Specimen	Predicted dielectric constant	Predicted time offset parameter

Specimen 1	5.931	0.949
Specimen 2	7.627	0.941
Specimen 3	7.452	0.924
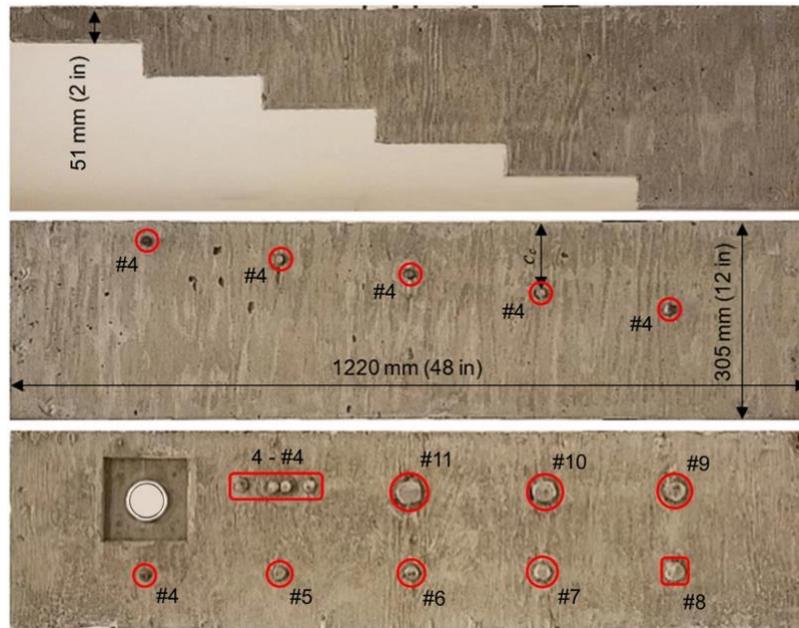
Figure 4-10. Images from rectified elevation view of the three test specimens (top to bottom): specimens 1, 2, and 3. Rebars are shown in red circles and rectangles (Figure 2-1 repeated from Chapter Two)

Next, we use our trained neural network model to predict the dielectric constant and offset parameter to run the XTFM algorithm. Table 4-8 shows the predicted parameters. It can be seen that the time offset parameters are very similar to each other. This makes sense because we are using the same instrument with the same frequency and input waveform.

Note that the trigger time of the transmitted pulse is not known. However, we used a value of 0.9 for the time offset in our previous work, which we determined through manual calibration by means of trial-and-error (see Chapter Two). The dielectric constant predicted parameters slightly differ for Specimen 1 compared to the other two specimens. This is not unexpected since our model is not trained on unreinforced data, which is not the case for Specimens 2 and 3. Nevertheless, XTFM and other synthetic aperture focusing techniques are approximate solutions and there is no ideal "golden" parameter that would produce a perfect image. Figure 4-11 shows the XTFM reconstructed images using the predicted parameters. It can be seen that using the predicted parameters results in reconstructed images that are very similar to the ones achieved by manually tuning the two parameters.

Next, we test the algorithm on the data collected from the experiments discussed in Chapter 2. Two columns were tested, and data were collected at seven different stages of loading and damage progression. At each stage, four measurements at different positions were taken (See Figure 3-3). Therefore, for each column, 28 measurements were taken. In order to feed the data into the model for prediction, a sliding window inference approach was adopted because the size of B-scans is larger than the size of the simulation dataset on which the network was trained. A window size of 481 pixels (in horizontal axis) was selected from the beginning of each B-scan and then shifted by 50 pixels for the next inference. The final predicted parameters are the average of the outputs for each window. Table 4-9 shows the results. It can be seen that the predicted values for offset parameters for measurements on both columns have a mean value very close to the value found for the data of Chapter 2 (See Table 4-8). Indeed, the offset parameter is only dependent on the

112

instrument, and all these datasets were taken with the same instrument. It can also be seen that the dielectric constants of the concrete of the two specimens in Chapter 3 do not differ notably with a low standard deviation between measurements. We reported in Chapter 3 that GPR is unable to detect changes when the columns are undergoing damage. Therefore, we do not expect changes in the dielectric constant with the progress of the damage.

Table 4-9. Predicted parameters of the dielectric constant and time offset for the Specimens of Chapter 3

Test Specimen	Predicted dielectric constant, mean $\pm$ standard deviation	Predicted time offset parameter, mean $\pm$ standard deviation
Column 1	4.731 ± 0.093	0.0916 ± 0.0006
Column 2	4.808 ± 0.054	0.0909 ± 0.0007

Figure 4-12 shows an example of a reconstructed image from with predicted parameters. The measurement is from north-east side of the Specimen 1 in Chapter 3. It can be seen that the rebars have a correct focus and are at the position of about 2 inches (0.0508 m) shown with red dashed line.
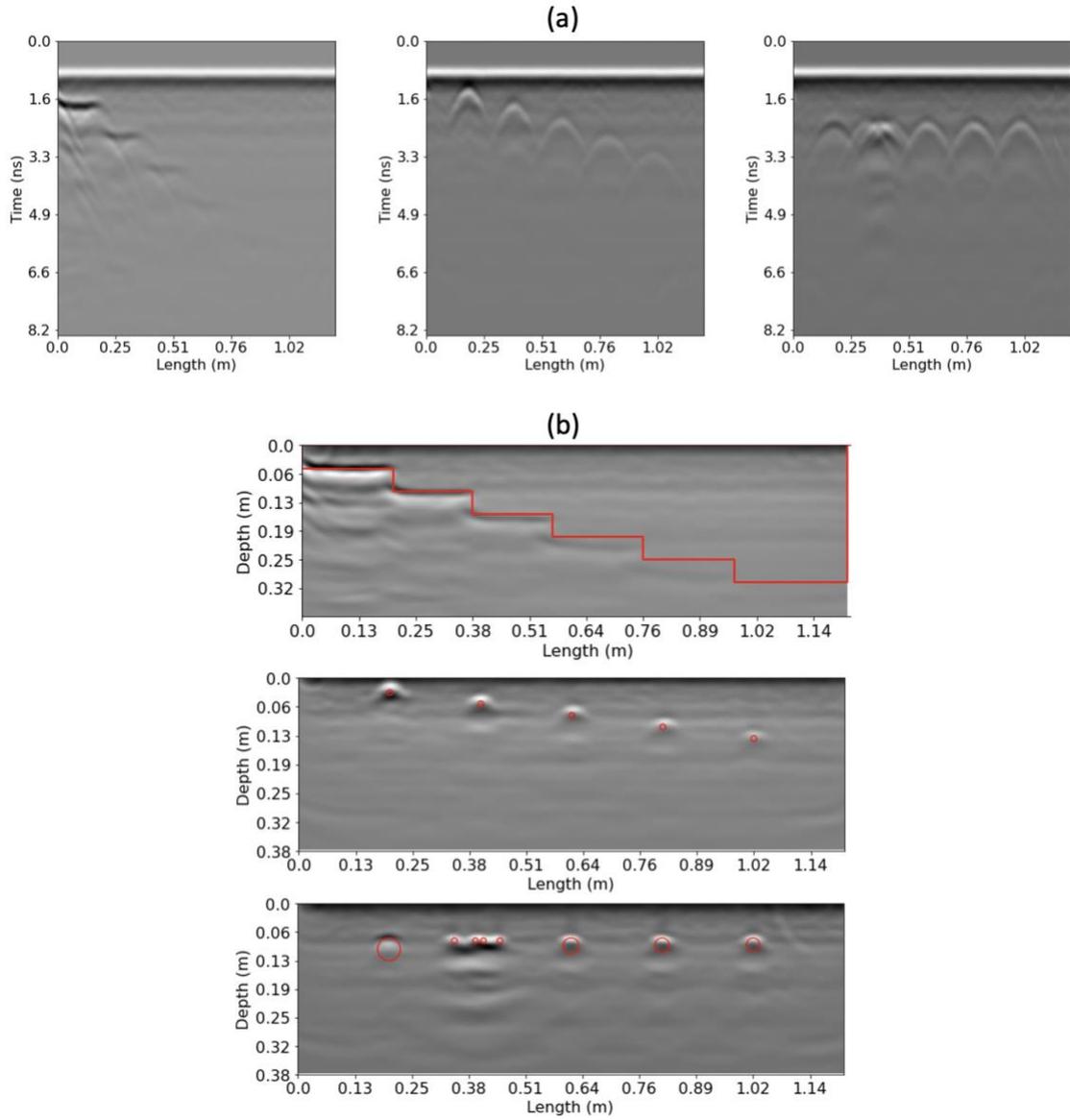
Figure 4-11. (a) B-scans of the three test specimens (left to right): Specimens 1 to 3 (in Chapter 2) and (b) XTFM reconstructed image of the three test specimens (top to bottom): Specimens 1 to 3 (in Chapter 2)

114
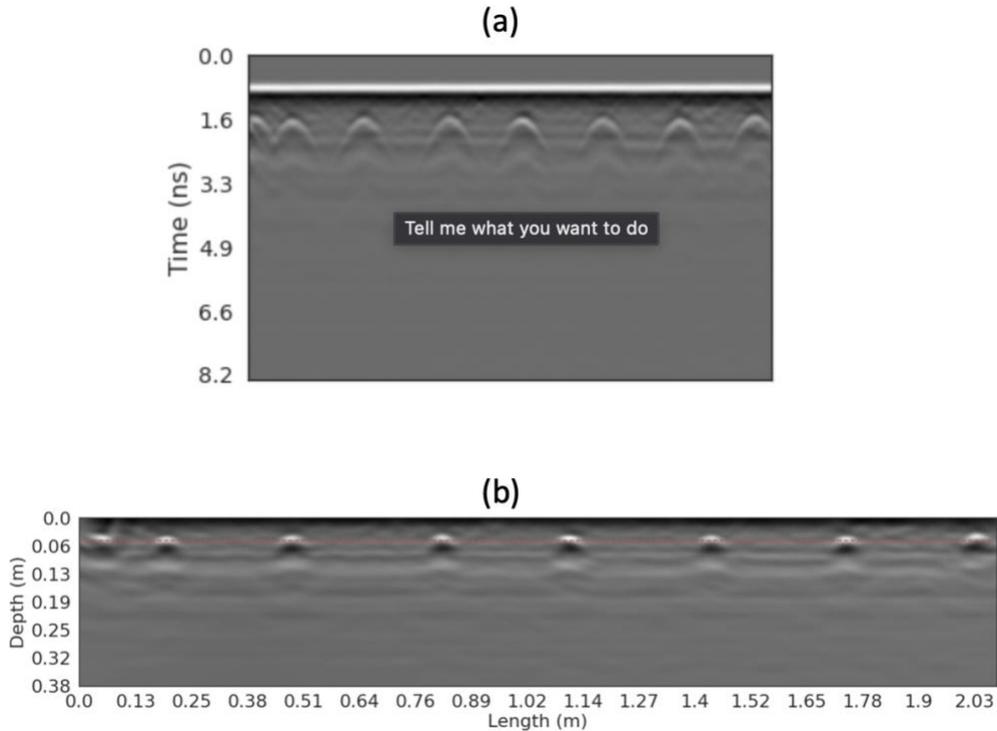
Figure 4-12. (a) B-scan of north-east side measurement from Specimen 1 in Chapter 3 and (b) XTFM reconstructed image of it with predicted parameters

Even though the model performs well on these real-world test cases, it would be naive to conclude that this model can generalize to every instrument, and we do not claim this. It should also be noted that the recording length of the real GPR instrument used for collecting of the data is 8.41 ns which is different from 10 ns of our generated dataset. Changing the simulation time may alter the B-scans in a way that learned features by the neural network is not applicable anymore. This is why the hyperbolic fitting methods built in GPR units, are only applicable to those units. We propose to investigate this in a separate study. A bigger simulation dataset that includes variability in other variables used in the

simulation such as simulation time (time window) can expose the network to more variability and make it gain better generalizability to external data from other instruments.

4.3.5. Model Explainability

Even though neural networks are notorious for being black boxes, there has been extensive research about how to find methods that can help us interpret (or explain) deep learning models [37, 38, 39, 40]. Here we use two methods to help decode what our neural network learns, namely feature maps visualization and gradient-weighted class activation mapping (Grad-CAM). We generated an extra 20 data examples (B-scans) with pulse frequencies of 1.5, 2, 2.5, and 3 MHz, and dielectric constants of 4, 6, 8, 10, and 12 to examine the slight differences of the B-scan visually. All of the generated new test cases were generated with a Ricker waveform [see Figure 4-2(d)]. The B-scans from these new test scenarios are shown in Figure 4-13.
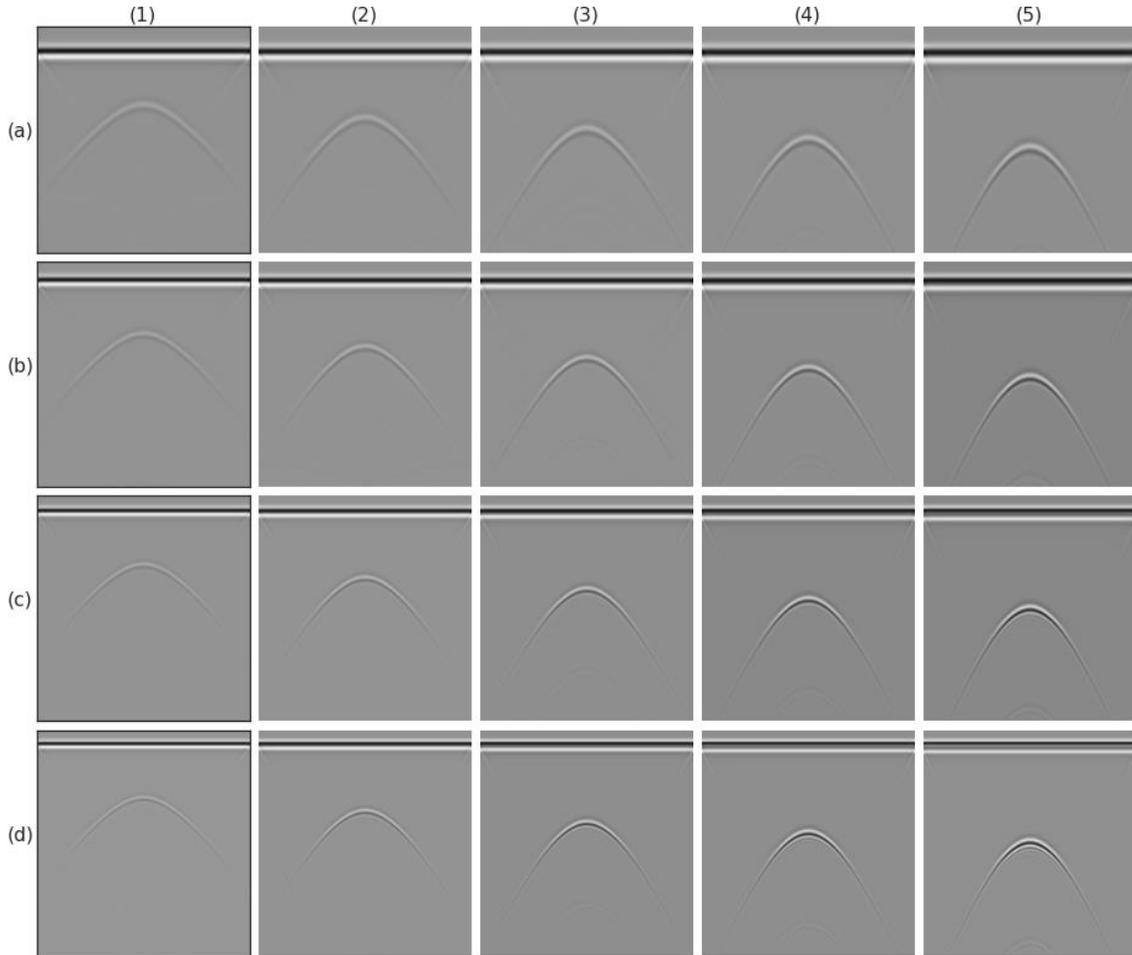
Figure 4-13. The new test set generated. From left to right (1) to (5) dielectric constant is 4, 6, 8, 10, and 12 respectively. From top to bottom (a) to (d) frequency is 1.5, 2, 2.5, and 3 respectively.

It can be seen that with increasing the dielectric constant [going from left to right, i.e., Figure 4-13 (1) to (5)] the hyperbole shifts down vertically in the image, and its width narrows. Increasing the frequency (going from top to bottom, i.e., Figure 4-13 (a) to (d)] results in a shift of the surface wave upward in the simulations, where delay of the pulse is related to frequency [see Equation (4)], and sharpens the appearance of the hyperbole. This

117

can of course be the explained by the inverse relationship between frequency and wavelength. Figure 4-14 shows actual vs. predicted correlation plots for this new test set. It can be seen that the model can predict both parameters accurately with an R^2 value of higher than 0.999.
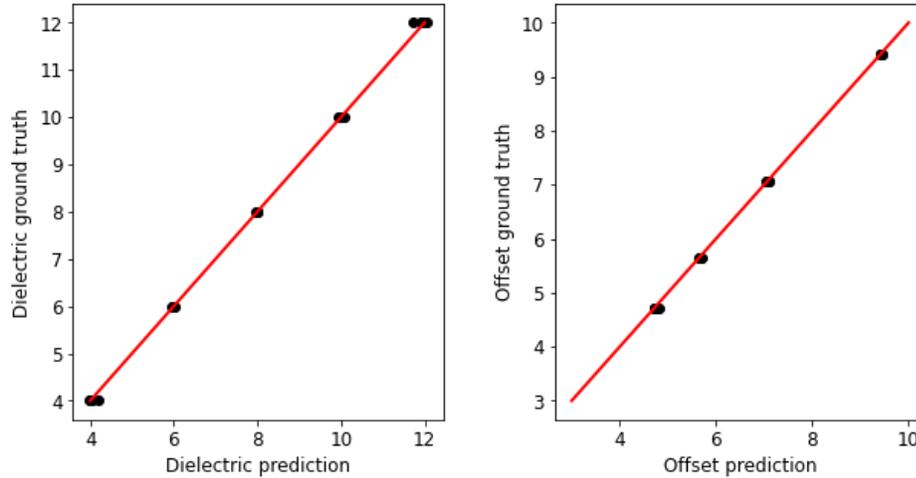
Figure 4-14. The actual and predicted values on the new test set for a) Dielectric constant, and b) Time offset parameter. The r2 value is higher than 0.999 for both.

4.3.5.1.Feature Maps

Feature maps or activation maps (or layer activations) show the results of convolving the learned filters to an input image [39]. Here, they show which parts of the B-scans are detected and are useful for predictions. Figure 4-15 (a) and (b) show some of the feature maps from the output for the third and five convolutional layers, respectively. It should be noted that the third and fifth convolutional layers have 256 and 512 filters, respectively, and not all the feature maps are shown here. The earlier convolutional layers activation maps usually show the more familiar objects and become more localized in the deeper

layers. It can be seen in Figure 4-15 that reflections from the corners and the hyperbolae are mostly activated as well as the surface wave portion of the B-scans.
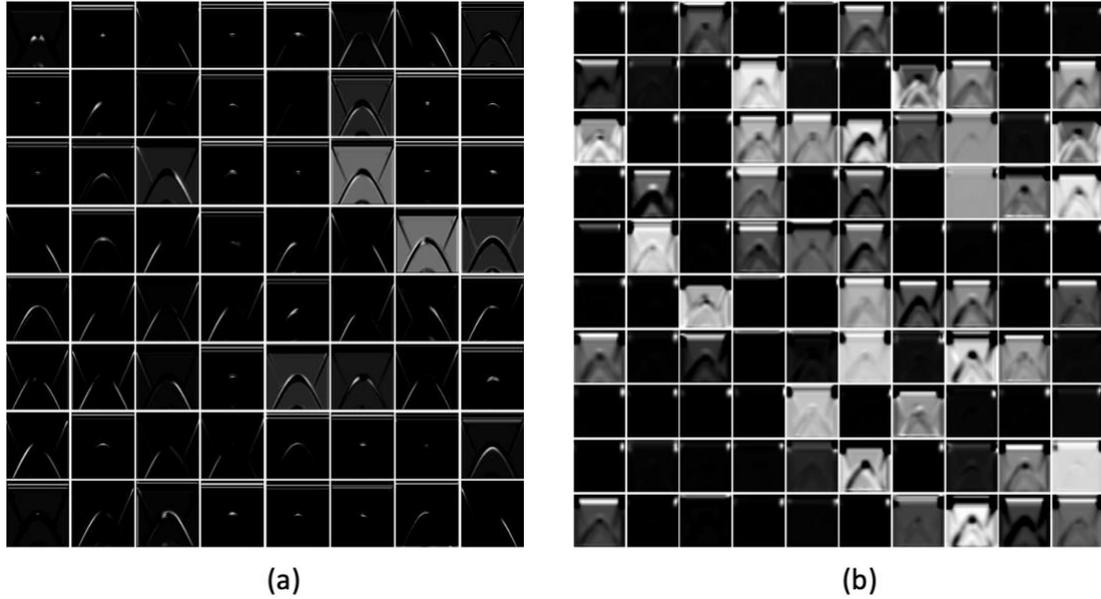
Figure 4-15. Feature maps (Activation maps) of the third (a) and last (b) convolution layer output from an input test case

4.3.5.2. Grad-CAM

Grad-CAM [40] uses the gradient information from a final convolutional layer to generate a coarse localization map that shows the important regions of the image that was used to predict the output. The Grad-CAM is designed to generate these saliency maps for each target class prediction of a classification network, however, since our problem is a regression problem, our output is numerical values. The last convolutional layer of our model has 512 filters. The output dependent gradients are computed for each of these filters and then averaged with respect to each pixel in the activation output of the last

convolutional layer with the size of 31×30, in our network shown as A^k. This average

results in a scalar value, which is the importance of feature map, k for target, t, which is

shown as α_k^t in Equation (5):

$$\alpha_k^t = \frac{1}{31 \times 30} \sum_{j=1}^{31} \sum_{i=1}^{30} \frac{\partial y^t}{\partial A_{ij}^k} \qquad (5)$$

where y^t is the prediction of of our network for each target, t, which is the dielectric

constant and the time offset. Next, after having the α_k^t for target, t, the weighted

combination of activation maps is calculated and followed by a RELU function to discard

the negative values. The reason as explained in the original paper [40] is that we are only

interested in the features that have a positive effect on the target output. Therefore, The

Grad-CAM of target, t is computed using Equation (6), as follows

$$L_{Grad-CAM}^c = RELU\left(\sum_{k=1}^{512} \alpha_k^t A^K\right) \qquad (6)$$

This results in a coarse saliency map that can be resized to the original input size and

overlaid on it to show which areas of the input the neural network used more for its

predictions.

Figure 4-16 (a) and (b) show the Grad-CAM maps of the data in our test set for the

dielectric constant and the time offset parameters, respectively. It can be seen that for the

offset parameters, the model is paying attention to the surface wave area. For the dielectric

constant, the model is mostly considering the two tiny angular edges of the image, which

seem parallel to the angle of the hyperbolae (see Figure 4-17). In [41], the authors show

that the exact shape of the hyperbola is dependent on the relative dielectric constant of the

half-space, the height of the source, and the propagation time from source to wavefront multiplied by the wave velocity. Figure 4-17 shows the contrast enhanced images of five examples from the new test cases. We increased the contrast of the images to emphasize subtle lines and angles. It can be seen how increasing the dielectric constant lowers the angle of the hyperbolae, which our neural network determined as the pertinent feature to predict the dielectric constant accurately.
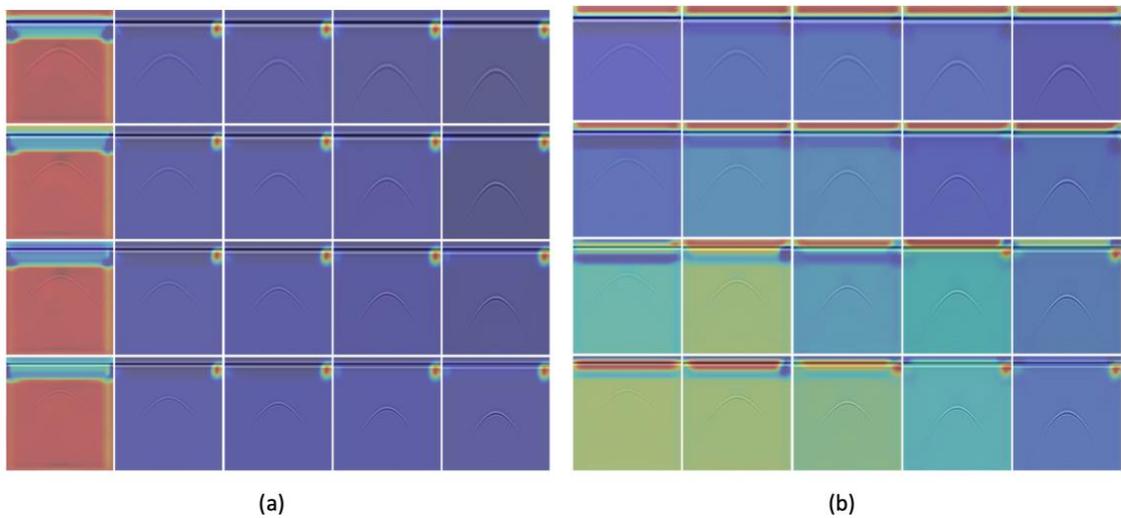
Figure 4-16. The Grad-Cam output for (a) dielectric constant and (b) time offset parameter
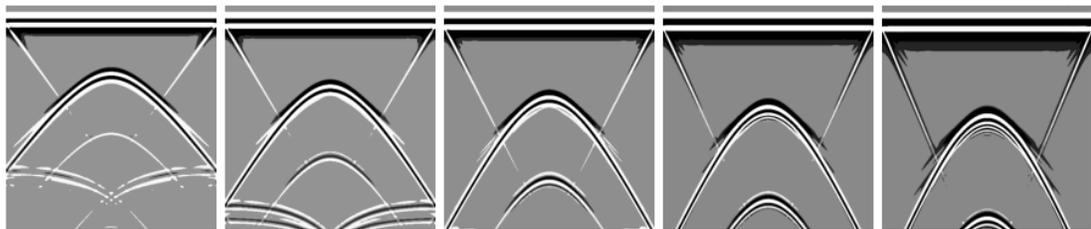
Figure 4-17. Five contrast-increased sample B-scans from newly generated test showing varying angle of corner reflections, left to right = dielectric constant of 4, 6, 8, 10 and 12

4.3.5.3. Occluding Features in B-scans

Since the neural network pays attention to the features in the corner of the input B-scans, we decided to occlude those areas to see if our model can still achieve good accuracy and visualize which parts of the image are utilized. The occlusions were defined as 200 pixels in depth and 100 pixels in length, located in the top two corners. Figure 4-18 shows samples of occluded B-scans. We trained the model again with exactly the same parameters as before. As expected, the performance of the model decreased slightly with a validation MAE loss of 0.0382 and validation MSE of 0.0037. It should be mentioned that this can still be considered having high accuracy. Figure 4-19 (a) shows the last layer activation map output from one of the test case inputs. It can be seen that compared to Figure 4-15 (b) there are more hyperbolic shapes and there are no corner pixels involved. We ran the Grad-CAM for the dielectric constant prediction output on the 20 new test cases. The results are shown in Figure 4-19 (b).

Figure 4-18. Samples of two occluded B-scans

It can be seen that this time, the model did not use the corner features and paid the most attention to the hyperbolic shape of the reflectors. Thus, we conclude that the model has truly learned what is important, and in the first case, it was trying to be more intelligent by only considering the corner reflections, which are indeed parallel to the side lobes of the hyperbolic reflections. The Grad-cam results for the offset output are not provided since they are very similar to Figure 4-16 (b) where the model is paying the most attention to the surface wave area.

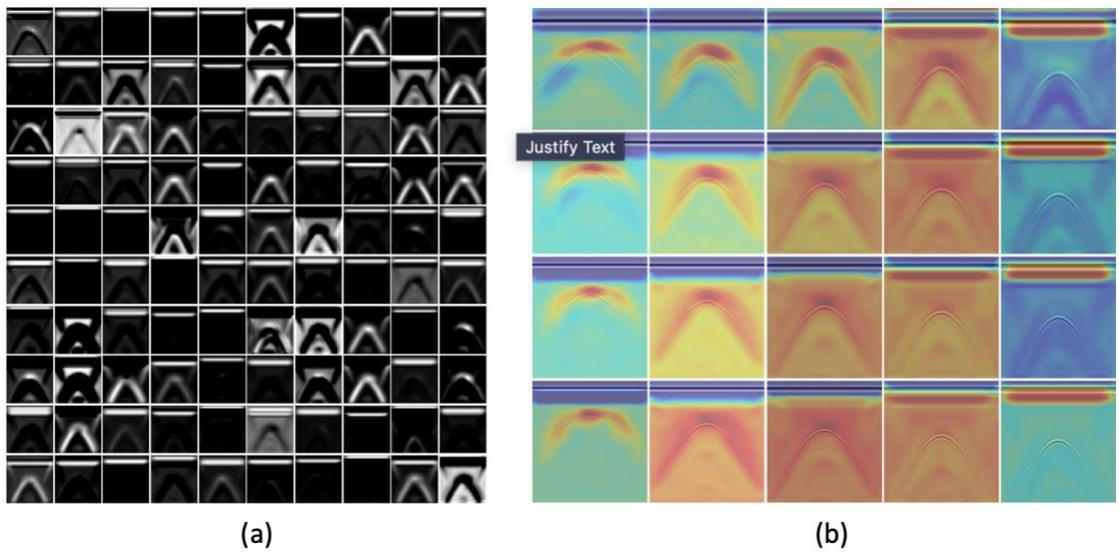(a)   (b)

Figure 4-19. (a) Feature maps of the last convolution layer output from an input test case and (b) The Grad-Cam output for dielectric target for the 20 newly generated test cases

4.4. Conclusion

In this study, we present a pipeline for data generation using GPR simulation and a deep learning model that can learn and predict two parameters required for image reconstruction using the XTFM algorithm, i.e., dielectric constant and time offset. The dataset is generated using the open-source software gprMax. The dataset is made available on GitHub. We experimented with different architectures and used VGG-16 architecture as the core of our model, which is composed of several convolutional and pooling layers. We also provide some insights about augmentation techniques, choice of learning rate, kernel initialization, and size of the dataset. The model achieved highly accurate results in predicting both parameters on the simulated validation and test sets. We also tested the model on a real-world dataset. Even though the model performed well on the real test data, we discussed that the generalizability of such neural networks is limited to the underlying distribution of the dataset generated. For example, in the generated dataset, the simulation time of the data is fixed, and it is not expected that the model trained on this dataset is able to generalize well on a dataset with a very different simulation time. In the end, we used two methods, namely, feature maps and gradient visualizations to visualize what features the model is learning and which parts of the input B-scan the model pays attention to. It turned out that for the offset parameter, the model is looking at the surface wave area, the portion that is usually discarded in GPR data pre-processing. For the dielectric constant, the model considers the angles of the hyperbolic reflections. We believe these are promising findings, showing that our neural network is able to select and use meaningful information within an image, which can help experts to have better insights when investigating GPR data.

4.5. References

[1]   LeCun, Y., Bengio, Y., & Hinton, G. (2015). Deep learning. *nature*, *521*(7553), 436-444.

[2]   Goodfellow, I., Bengio, Y., & Courville, A. (2016). *Deep learning*. MIT press.

[3]   LeCun, Y., Bottou, L., Bengio, Y., & Haffner, P. (1998). Gradient-based learning applied to document recognition. *Proceedings of the IEEE*, *86*(11), 2278-2324.

[4]   Deng, J., Dong, W., Socher, R., Li, L. J., Li, K., & Fei-Fei, L. (2009, June). Imagenet: A large-scale hierarchical image database. In *2009 IEEE conference on computer vision and pattern recognition* (pp. 248-255). Ieee.

[5]   Krizhevsky, A., Sutskever, I., & Hinton, G. E. (2012). Imagenet classification with deep convolutional neural networks. *Advances in neural information processing systems*, *25*.

[6]   Liu, H., Lin, C., Cui, J., Fan, L., Xie, X., & Spencer, B. F. (2020). Detection and localization of rebar in concrete by deep learning using ground penetrating radar. *Automation in construction*, *118*, 103279.

[7]   Hou, F., Lei, W., Li, S., & Xi, J. (2021). Deep learning-based subsurface target detection from GPR scans. *IEEE Sensors Journal*, *21*(6), 8161-8171.

[8]   Dinh, K., Gucunski, N., & Duong, T. H. (2018). An algorithm for automatic localization and detection of rebars from GPR data of concrete bridge decks. *Automation in Construction*, *89*, 292-298.

[9]   Xiang, Z., & Rashidi, A. (2019). An improved convolutional neural network system for automatically detecting rebar in GPR data. *arXiv preprint arXiv:1907.09997*.

[10]   Wang, J., Chen, K., Liu, H., Zhang, J., Kang, W., I S., ... & Wang, Z. (2021). Deep learning-based rebar clutters removal and defect echoes enhancement in GPR images. *IEEE Access*, *9*, 87207-87218.

[11]   Sun, H. H., Cheng, W., & Fan, Z. (2022). Learning to Remove Clutter in Real-World GPR Images Using Hybrid Data. *IEEE Transactions on Geoscience and Remote Sensing*.

[12]   Liu, B., Ren, Y., Liu, H., Xu, H., Wang, Z., Cohn, A. G., & Jiang, P. (2021). GPRInvNet: Deep Learning-Based Ground-Penetrating Radar Data Inversion for Tunnel Linings. *IEEE Transactions on Geoscience and Remote Sensing*.

[13]   Alvarez, J. K., & Kodagoda, S. (2018, May). Application of deep learning image-to-image transformation networks to GPR radargrams for sub-surface imaging in infrastructure monitoring. [I]n *2018 13th IEEE Conference on Industrial Electronics and Applications (ICIEA)* (pp. 611-616). IEEE.

[14]   Ji, Y., Zhang, F., Wang, J., Wang, Z., Jiang, P., Liu, H., & Sui, Q. (2021). Deep neural network-based permittivity inversions for ground penetrating radar data. *IEEE Sensors Journal*, *21*(6), 8172-8183.

[15]   Yang, S., Wang, Z., Wang, J., Cohn, A. G., Zhang, J., Ing, P., ... & Sui, Q. (2022). Defect segmentation: Mapping tunnel lining internal defects with ground penetrating radar data using a convolutional neural network. *Construction and Building Materials*, *319*, 125658.

[16]   Wang, J., Liu, H., Jiang, P., Wang, Z., Sui, Q., & Zhang, F. (2021). GPRI2Net: A Deep-Neural-Network-Based Ground Penetrating Radar Data Inversion and Object Identification Framework for Consecutive and Long Survey Lines. *IEEE Transactions on Geoscience and Remote Sensing*.

[17]   Xie, L., Zhao, Q., Ma, C., Liao, B., & Huo, J. (2020). Ü-Net: Deep-Learning Schemes for Ground Penetrating Radar Data Inversion. *Journal of Environmental and Engineering Geophysics*, *25*(2), 287-292.

[18]   Holmes, C., Drinkwater, B. W., & Wilcox, P. D. (2005). Post-processing of the full matrix of ultrasonic transmit–receive array data for non-destructive evaluation. *NDT & e International*, *38*(8), 701-711.

[19]   Schickert M, Krause M, Müller W (2003) Ultrasonic imaging of concrete elements using reconstruction by synthetic aperture focusing technique. J Mater Civ Eng 15(3):235–246

[20]   Özdemir, C., Demirci, Ş., Yiğit, E., & Yilmaz, B. (2014). A review on migration methods in B-scan ground penetrating radar imaging. *Mathematical Problems in Engineering*, *2014*.

[21]   Clem, D. J., Schumacher, T., & Deshon, J. P. (2015). A consistent approach for processing and interpretation of data from concrete bridge members collected with a hand-held GPR device. *Construction and Building Materials*, *86*, 140-148.

[22]   Lipton, Z. C., & Steinhardt, J. (2019). Research for practice: troubling trends in machine-learning scholarship. *Communications of the ACM*, *62*(6), 45-53.

[23]   Ng, A., Laird, D., & He, L. (2021). Data-Centric AI Competition. *DeepLearning AI. Available online: https://https-deeplearning-ai. github. io/data-centric-comp/(accessed on 9 December 2021)*.

[24]   Mazumder, M., Banbury, C., Yao, X., Karlaš, B., Rojas, W. G.Iiamos, S., ... & Reddi, V. J. (2022). DataPerf: Benchmarks for Data-Centric AI Development. *arXiv preprint arXiv:2207.10062*.

[25]   Mehdinia S (2022) GitHub repository. https://github.com/Sinamhd9/A-deep-learning-and-simulation-pipeline-for-image-reconstruction-of-GPR-data

[26]   Warren, C., Giannopoulos, A., & Giannakis, I. (2016). gprMax: Open source software to simulate electromagnetic wave propagation for Ground Penetrating Radar. *Computer Physics Communications*, *209*, 163-170.

[27]   Warren, C., Giannopoulos, A., Gray, A., Giannakis, I., Patterson, A., Wetter, L., & Hamrah, A. (2019). A CUDA-based GPU engine for gprMax: Open source FDTD electromagnetic simulation software. *Computer Physics Communications*, *237*, 208-218.

[28]   Simonyan, K., & Zisserman, A. (2014). Very deep convolutional networks for large-scale image recognition. *arXiv preprint arXiv:1409.1556*.

[29]   Bourdi, T., Rhazi, J. E., Boone, F., & Ballivy, G. (2012). Modelling dielectric-constant values of concrete: An aid to shielding effectiveness prediction and ground-penetrating radar wave technique interpretation. *Journal of Physics D: Applied Physics*, *45*(40), 405401.

[30]   Mehdinia S (2021) GitHub repository. https://github.com/Sinamhd9/A-Pipeline-for-Enhanced-Multimodal-Imaging-of-Structural-Concrete

[31]   Gavrikov,   P.   (2020).   GitHub   repository. https://github.com/paulgavrikov/visualkeras

[32]   Abadi, M., Agarwal, A., Barham, P., Brevdo, E., Chen, Z., Citro, C., ... & Zheng, X. (2016). Tensorflow: Large-scale machine learning on heterogeneous distributed systems. *arXiv preprint arXiv:1603.04467*.

[33]   François Chollet et al. Keras. https://github.com/fchollet/keras, 2015.

[34]   Buslaev, A., Iglovikov, V. I., Khvedchenya, E., Parinov, A., Druzhinin, M., & Kalinin, A. A. (2020). Albumentations: fast and flexible image augmentations. *Information*, *11*(2), 125.

[35]   Kingma, D. P., & Ba, J. (2014). Adam: A method for stochastic optimization. *arXiv preprint arXiv:1412.6980*.

[36]   Loshchilov, I., & Hutter, F. (2016). Sgdr: Stochastic gradient descent with warm restarts. *arXiv preprint arXiv:1608.03983*.

[37]   Zhang, Q. S., & Zhu, S. C. (2018). Visual interpretability for deep learning: a survey. *Frontiers of Information Technology & Electronic Engineering*, *19*(1), 27-39.

[38]   Zeiler, M. D., & Fergus, R. (2014, September). Visualizing and understanding convolutional networks. In *European conference on computer vision* (pp. 818-833). Springer, Cham.

[39]   Karpathy, A. (2016). Neural Networks Part 1: Setting Up the Architecture. Notes for CS231n Convolutional Neural Networks for Visual Recognition.

[40]   Selvaraju, R. R., Cogswell, M., Das, A., Vedantam, R., Parikh, D., & Batra, D. (2017). Grad-cam: Visual explanations from deep networks via gradient-based localization. In *Proceedings of the IEEE international conference on computer vision* (pp. 618-626).

[41]   Rappaport, C. M. (2007). Accurate determination of underground GPR wavefront and B-scan shape from above-ground point sources. *IEEE Transactions on Geoscience and Remote Sensing*, *45*(8), 2429-2434.

5. Chapter Five: Conclusions and Outlook

5.1. Summary and Conclusions

The focus of this PhD dissertation research was to develop algorithms and tools for advanced imaging of concrete structures. The unique contributions of this dissertation are the algorithmic development of advanced imaging methods and development of image quality metrics that can be used by the engineers to achieve enhanced images of the concrete and be able to evaluate them quantitatively. This dissertation lays the foundation for advanced imaging of the concrete. Two novel comprehensive algorithmic pipelines are proposed:

- Extended total focusing method (XTFM) and multimodal image fusion pipeline: The XTFM algorithm is based on the core algorithms of the syntenic aperture focusing technique (SAFT) and the total focusing method (TFM). This algorithm can take inputs from either GPR and UEA, single channel or multi-channel, with or without overlapping measurements, and reconstruct the image in a computationally efficient way. The algorithms were written in both in MATLAB and Python and are available for free on the GitHub page of the first manuscript (Chapter Two). In addition, some image quality metrics are introduced that can help with assessing the quality of the reconstructed and fused images. In Chapter Two it is demonstrated that the images reconstructed from the interior of concrete is enhanced as they are easier to interpret by a human inspector and they have a higher information content as determined by most image quality metrics.

132

- GPR simulation and deep learning pipeline: A simulation and deep learning pipeline is developed that builds on top of the XTFM algorithm and automates some parts of it. Simulation offers powerful possibilities that one can generate artificial datasets that are similar to real-world data. The dataset is shared freely with the community on the GitHub page of the second manuscript (Chapter Four). A deep learning model is proposed that can learn from the simulated data to predict two key parameters that otherwise require cumbersome manual tuning. Emphasis was given to model generalization and explainability and it is shown that the knowledge extracted from the deep learning model can be useful for non-destructive testing experts.

Additionally, the XTFM and image fusion imaging pipeline was applied to two full-scale concrete specimens tested in laboratory (see Chapter Three). The ability of the imaging pipeline to track damage progression is investigated while the specimens undergo reverse-cyclic loading. It is shown that the proposed imaging pipeline has the ability to track damage as early as first cycles of loading that impose some internal changes to the material compared to a baseline measurement. Therefore, obtaining a few baseline measurements after the construction of a structure can be a valuable asset that can later be used to identify damage after an extreme event such as an earthquake. Finally, two quantitative analysis metrics are introduced that can assist with analyzing the images.

5.2. Outlook and Recommended Future Work

There is tremendous potential in making use of simulation and deep learning in imaging of concrete structures. New datasets can be generated with the goal of solving different NDT

problems. Deep learning models can learn from these datasets and assist engineers in real time with the detection, localization, and diagnostics of concrete. In addition, ultrasonic simulations are not investigated in this dissertation. Generating UEA simulations, besides GPR, can lead to multi-modal simulated datasets and opens numerous possibilities for deep learning models to learn from both datasets. Below are some ideas for further research:

1. Generate simulated datasets for both GPR, and UEA. Train a deep learning model that takes UEA and GPR B-scans as input, and outputs a fused image.

2. Generate a simulated dataset with both GPR and UEA with possible concrete defects and train a model to classify and localize these defects based on the B-scan input from one or both modalities, or the fused image of these two.

3. An end-to-end deep learning model can be developed to take B-scans as input, and the perfect geometry as output. This model can replace the XTFM and similar synthetic aperture focusing techniques entirely. This model should learn the spatial relationship of the input and output since the location of the real objects are not the locations where they appear in the input B-scan. That location is dependent on dielectric constant and other variables of the instrument and media. Therefore, this cannot be a segmentation problem where input and outputs are spatially aligned.

4. Develop a model that takes the geometry as input and predicts its possible B-scan using a specific instrument. Simulation is time consuming, and this model can help generate new datasets rapidly that can be used to augment the real datasets. The generated datasets can be used for deep learning tasks, such as the ones proposed above.

With proven results from simulation, new laboratory specimens can be built to test the ability of these methods on real-world data